

# Spitzer IRAC and MIPS Imaging of Clusters and Outflows in 9 High-mass Star Forming Regions

Keping Qiu<sup>1,2</sup>, Qizhou Zhang<sup>2</sup>, S. Thomas Megeath<sup>3</sup>, Robert A. Gutermuth<sup>2</sup>, Henrik Beuther<sup>4</sup>, Debra S. Shepherd<sup>5</sup>, T. K. Sridharan<sup>2</sup>, L. Testi<sup>6,7</sup>, and C. G. De Pree<sup>8</sup>

kqiu@cfa.harvard.edu

## ABSTRACT

We present *Spitzer* Space Telescope IRAC and MIPS observations toward a sample of nine high-mass star forming regions at a distance of around 2 kpc. Based on IRAC and MIPS 24  $\mu\text{m}$  photometric results and 2MASS *JHKs* data, we carry out a census of young stellar objects (YSOs) in a  $5' \times 5'$  field toward each region. Toward seven out of the nine regions, we detect parsec sized clusters with around 20 YSOs surrounded by a more extended and sparse distribution of young stars and protostars. For the other two regions, IRAS 20126+4104 and IRAS 22172+5549, the former has the lowest number of YSOs in the sample and shows no obvious cluster, and the latter appears to be part of a larger, potentially more evolved cluster. The deep IRAC imaging reveals at least twelve outflows in eight out of the nine regions, with nine outflows prominent in the 4.5  $\mu\text{m}$  band most probably attributed to shocked H<sub>2</sub> emission, two outflows dominated by scattered light in the 3.6 and 4.5  $\mu\text{m}$  bands, and one outflow standing out from its hydrocarbon emission in the 8.0  $\mu\text{m}$  band. In comparison with previous ground-based observations, our IRAC observations reveal new outflow structures in five regions. The dramatically different morphologies of detected outflows can be tentatively interpreted in terms of possible evolution of massive outflows.

---

<sup>1</sup>Department of Astronomy, Nanjing University, Nanjing, China

<sup>2</sup>Harvard-Smithsonian Center for Astrophysics, Cambridge, MA

<sup>3</sup>Department of Physics and Astronomy, University of Toledo, Toledo, OH

<sup>4</sup>Max-Planck-Institute for Astronomy, Heidelberg, Germany

<sup>5</sup>National Radio Astronomical Observatory, Socorro, NM

<sup>6</sup>Osservatorio Astrofisico di Arcetri, Firenze, Italy

<sup>7</sup>ESO, Karl-Schwarzschild-Str. 2, D-85748 Garching bei München, Germany

<sup>8</sup>Department of Physics and Astronomy, Agnes Scott College, Decatur, GA

The driving sources of these outflows are deeply embedded in dense dusty cores revealed by previous millimeter interferometric observations. We detect infrared counterparts of these dusty cores in the IRAC or MIPS 24  $\mu\text{m}$  bands. Reflection nebulae dominated by the emission from UV heated hydrocarbons in the 8  $\mu\text{m}$  band can be found in most regions and they may imply the presence of young B stars.

*Subject headings:* infrared: stars — stars: formation — stars: pre-main-sequence — ISM: jets and outflows — ISM: reflection nebulae

## 1. Introduction

It is well known that high-mass stars form in dense clusters (Lada & Lada 2003). The research on embedded young clusters around young intermediate- to high-mass stars has advanced significantly via near-infrared surveys (e.g., Testi et al. 1999; Gutermuth et al. 2005; Kumar et al. 2006). The *Spitzer* space telescope with its unprecedented sensitivity at mid-infrared wavelengths provides a new means for identifying young stellar objects (YSOs) in star forming regions through detection of dusty disks and envelopes. High sensitivity in the 3 – 24  $\mu\text{m}$  bands is invaluable for distinguishing young stars from reddened background stars through infrared excess arising from circumstellar materials (Allen et al. 2004; Megeath et al. 2004; Whitney et al. 2004; Gutermuth et al. 2004; Muzerolle et al. 2004). This capability is particularly valuable for studies of high-mass star forming regions for two reasons: 1) such regions are typically located near the Galactic plane where the density of background stars is high and 2) the member YSOs are often faint due to the large distances to these regions ( $> 1\text{kpc}$ ). The faint magnitude of the YSOs complicates not only the detection of members but also their identification since the density of background stars rises rapidly with increasing magnitudes. With the Infrared Array Camera (IRAC) and Multiband Imaging Photometer for *Spitzer* (MIPS), a significant census of YSOs can be carried out, which provides a fossil record of the distribution of star formation sites and information on the environments in which stars and planets form. This method is particularly effective for finding extended, lower density distributions of stars surrounding the dense regions of embedded clusters.

Extended structures, such as reflection nebulae and outflows, can also be mapped with the IRAC. Outflows emanating from the central young stars or protostars are usually detectable in rotational transitions of CO and other molecules at (sub)millimeter wavelengths. In IRAC observations, outflows can be revealed from shocked H<sub>2</sub> emission. Hydrodynamic simulations of shock models predict that H<sub>2</sub> emission is particularly strong in the 4.5  $\mu\text{m}$  band (Smith & Rosen 2005). Since the 4.5  $\mu\text{m}$  band is relatively free of the emission from hy-

drocarbons (probably in the form of Polycyclic Aromatic Hydrocarbons, or PAHs) compared with the other three bands, and the 5.8 and 8.0  $\mu\text{m}$  bands are significantly less sensitive than the shorter wavelength bands, composite images with emission from different bands coded in different colors can be a diagnostic tool for  $\text{H}_2$  emission in outflows. A remarkable example of such a detection can be found in the IRAC observations of the HH 46/47 outflow, a collimated bipolar outflow emanating from a low-mass protostar, where the southwestern lobe was clearly seen in the 4.5  $\mu\text{m}$  band as a limb-brightened bow-shock cavity (Raga et al. 2004; Noriega-Crespo et al. 2004b). Smith et al. (2006) reported the IRAC detection of a spectacular outflow in the high-mass star forming region DR 21 by virtue of its brightness in the 4.5  $\mu\text{m}$  band. Further investigations of the *ISO* SWS spectra of the DR 21 outflow verified that the  $\text{H}_2$  lines contribute significantly to all four IRAC bands and the emission in the 4.5  $\mu\text{m}$  band is mostly attributed to the  $\text{H}_2$   $v=0-0$   $S(9)$  (4.695  $\mu\text{m}$ ) line. Outflow activities can also be revealed from scattered light in the IRAC bands. By comparison of the deep IRAC imaging of L1448 with the radiative transfer modelling, Tobin et al. (2007) demonstrated that the observed infrared emission in the IRAC bands is consistent with the scattered light from the central low-mass protostars escaping the cavities carved by molecular outflows. Valusamy et al. (2007) reprocessed the IRAC observations of the HH 46/47 outflow using a deconvolution algorithm and found a wide-angle biconical component in scattered light in addition to the previously reported bow-shock cavity. Finally, in some cases hydrocarbon emission is visible from outflow cavities, presumably due to the illumination of the cavity walls by UV radiation from the central source (van den Ancker et al. 2000).

We have observed a sample of nine high-mass star forming regions with the IRAC and MIPS instruments (PID: 3528, PI: Qizhou Zhang). These regions were chosen according to the following criteria: 1) already imaged with millimeter interferometers; 2) known to have molecular outflows; 3) outside of the GLIMPSE survey except IRAS 19410+2336; 4) at a distance of  $< 2.5\text{kpc}$  ( $< 5000\text{AU}$  at the resolution of IRAC). These regions exhibit far-infrared luminosities ranging from  $10^3$  to  $10^5 L_\odot$  (see Table 1 for source parameters). We carry out a census of YSOs toward each region, and simultaneously, zoom in on the central massive star formation sites with the aim of searching for infrared counterparts of millimeter continuum sources and infrared emission from outflows. In this paper we present initial results of the observations. In § 2, we describe the observations. We present observational results in § 3 and subsequent discussion in § 4. A brief summary is given in § 5.

## 2. Observations and Data Reduction

The IRAC (Fazio et al. 2004) observations were obtained from February to September 2005 except IRAS 19410+2336, which was observed in October 2004. Each region was observed in the High Dynamic Range mode with 0.4 second and 10.4 second integration times per dither, and 16 dithers per map position. The area covered by all four bands is roughly  $5' \times 5'$ . The total effective integration time per pixel is 166.4 seconds. The 0.4 second integration frames were used to obtain photometry for bright sources. The frames were processed by the Spitzer Science Center (SSC) using the standard pipeline version S13.2 to produce the standard Basic Calibrated Data (BCD) products. Additional bright source artifacts (“jailbar”, “pulldown”, “muxbleed”, and “banding”) were removed or mitigated using customized IDL scripts developed by the IRAC instrument team (Hora et al. 2004; Pipher et al. 2004). There are often “bandwidth” artifacts in the 5.8 and 8.0  $\mu\text{m}$  images, where a decaying trail of the 4th, 8th, and in some cases even 12th pixels to the right of a bright or saturated spot is found. Currently there is no correction for this effect. Mosaics were created at the native instrument resolution of 1.”2 per pixel from the BCD frames using Gutermuth’s WCSmosaic IDL package (Gutermuth et al. 2007). Since the IRAC data is under-sampled and the point-spread-function (PSF) varies in shape with position and signal, aperture photometry is currently preferred over the PSF-fitting photometry. Source finding and aperture photometry were performed using Gutermuth’s IDL photometry and visualization tool PhotVis, version 1.10 (Gutermuth et al. 2004, 2007). The radii of the source aperture, the inner and outer boundaries of the sky annulus were set to 2.”4, 2.”4 and 7.”2, respectively. IRAC photometry was calibrated using large-aperture measurements of several standard stars from observations obtained in flight (Reach et al. 2005). There is a  $\sim 5\%$  calibration uncertainty due to a position dependent gain for point sources which is not corrected by the flat field. It is the dominant source of uncertainty in the photometry of IRAC images. Fluxes at zero mag are 280.9 Jy at 3.6  $\mu\text{m}$ , 179.7 Jy at 4.5  $\mu\text{m}$ , 115.0 Jy at 5.8  $\mu\text{m}$ , and 64.1 Jy at 8.0  $\mu\text{m}$ . Magnitudes for 1 DN/s are set to 19.455 at 3.6  $\mu\text{m}$ , 18.699 at 4.5  $\mu\text{m}$ , 16.498 at 5.8  $\mu\text{m}$ , and 16.892 at 8.0  $\mu\text{m}$ , using standard aperture corrections for the radii adopted (see Table 5.7 in IRAC Data Handbook v3.0). Since regions of active star formation often have bright nebulosity in the 5.8 and 8.0  $\mu\text{m}$  bands, we rejected detections with photometric uncertainties above 0.25 mag in these two bands, while for the 3.6 and 4.5  $\mu\text{m}$  bands detections with uncertainties above 0.2 mag were rejected. The number of detected sources and the limiting magnitude for each band toward each region are listed in Table 2.

The MIPS (Rieke et al. 2004) observations were undertaken in the photometry mode during campaigns separated by less than 1 month from the IRAC observations with the exception of IRAS 22172+5549 (1.5 months separation) and HH 80-81 (5 months separation).

The target sources were mapped in the 24 and  $70\mu\text{m}$  bands. The MIPS  $70\mu\text{m}$  images were severely saturated and not included in this paper. The  $24\mu\text{m}$  observations consist of 400 frames with an integration of 2.62 seconds per frame, resulting in a total effective integration time of 1048 seconds. The frames were processed by the SSC standard pipeline S16.0 for AFGL 5142, IRAS 05358+3543, and G192.16-3.82, and by pipeline S16.1 for the other regions. Mosaics were created based on the BCD frames using the SSC MOPEX package, with a pixel size of  $1.^{\prime\prime}225$  (half of the native instrument resolution). The central brightest sources in all the regions except IRAS 22172+5549 were significantly saturated. Unsaturated point sources with peaks more than 10 times the RMS noise level were identified using Photvis 1.10. Aperture photometry with a 5 pixel aperture and a sky annulus from 12 to 15 pixels was performed on these sources. Multiplying by  $\frac{1}{4}$  to correct for the smaller mosaic pixels and by 1.708 to correct from a 5 pixel aperture to infinite, and using a zero mag flux of 7.3 Jy, the aperture photometry was converted to magnitudes (Winston et al. 2007). The detections with photometric uncertainties above 0.25 mag were rejected. The number of detected sources and the limiting magnitude toward each region are listed in Table 2.

The PSF-fitting photometry is preferred in crowded fields with multiple point-sources. While in our MIPS  $24\mu\text{m}$  images, only about 10 to 20 unsaturated objects were detected in each field with a sparse distribution, and in some fields the PSF-fitting photometry is limited by the lack of ideal PSF-generating stars which are supposed to be bright, unsaturated, and uncontaminated by nebulosity. To further evaluate the aperture photometry quantitatively, we performed PSF-fitting photometry on all the  $24\mu\text{m}$  detections using the IDL DAOPHOT package. The reference PSF was generated from one to two objects chosen from the available in the field to be most suitable for PSF-generating. We then compared the returns from the PSF-fitting with the aperture photometry and found that the majority of unsaturated objects agree with each other in 0.2 mag; a few objects show differences of 0.3 to 0.4 mag but these objects are relatively faint and located in a spatially varying background, thus the differences are probably due to background subtraction, a limitation to both aperture and PSF-fitting photometry. Therefore, in Table 3 we show the aperture photometry with the exception of four objects. These four objects are blended with a neighboring brighter object; the resulting magnitudes derived from the contaminated aperture photometry is consequently 0.5 to 0.6 mag brighter than those determined with the PSF-fitting photometry. We show the PSF-fitting photometry for these objects and have annotated the table to identify these objects.

In addition, there are three slightly saturated objects in our sample (annotated in Table 3); we derived their magnitudes by manually scaling the PSF, subtracting the PSF from the image, and comparing the averaged residual of the PSF wing with a sky value taken from an annulus of 12 to 15 pixels. The tabulated magnitudes give an averaged residual closest to

the sky value. Since raising/lowering the magnitudes by 0.1 would give an averaged residual distinctly higher/lower than the sky value, we adopt an uncertainty of 0.1 mag for these objects.

### 3. Results

#### 3.1. Young Stellar Objects Census

In this section, we carry out a census of YSOs and classify them using their positions in near- to mid-infrared color-color diagrams. The results of this analysis are shown in Figure 1, where we display the colors of the detected YSOs in all nine regions, and Figure 2, where we show color-composite images of the regions with the identified YSOs overlaid. We list the number of identified YSOs in Table 1, and present the multi-band photometry of each YSO in Table 3.

Although the criteria we have used to identify YSOs were developed primarily for low-mass stars, we do not select sources in specific mass ranges. The census will be dominated by low-mass YSOs, but intermediate-mass YSOs, such as Herbig Ae/Be stars with disks and intermediate-mass protostars, may be identified by the same method. Since we are observing high-mass star forming regions, high-mass young stars and protostars certainly exist in our fields. Candidate massive protostellar objects in the IRAC bands have been identified with the GLIMPSE survey (Kumar & Grave 2007); however, the colors of those objects are less well understood. It is unclear whether this method is effective for identifying high-mass stars with disks or envelopes. In our sample, there are twelve objects exhibiting obvious infrared excess in one or more color-color diagrams and also showing evidence of being an intermediate- to high-mass star (labelled as “High” in the last column of Table 3 and marked with blue crosses in Figure 2). These objects show no or weak dust emission in the millimeter continuum (except the exciting star of the HII region W75 N (A), which is within a warm dust shell) and appear very bright in near-infrared, suggesting the lack of dense envelopes thus more evolved than typical protostars. Part of these objects are identified as candidate exciting sources of the surrounding UV-heated reflection nebulae (§3.3). In contrast, the youngest high-mass stars in our sample are still deeply embedded in dense dusty cores which were identified as millimeter continuum sources in previous interferometric observations. Most of these millimeter sources are not detected shortward of  $3.6 \mu\text{m}$ , and in some cases even undetectable at longer wavelengths. Given the extra level of complication and uncertainty in identifying and classifying these youngest high-mass objects, we exclude these objects from this section and discuss them in more detail in §3.2.

### 3.1.1. *IRAC diagram*

Allen et al. (2004) and Megeath et al. (2004) have established a YSOs classification scheme in the IRAC color-color diagram [3.6]-[4.5] vs. [5.8]-[8.0]. This scheme was confirmed by Hartmann et al. (2005) with an IRAC survey of a sample of known Taurus pre-main-sequence stars, even though some ambiguities were found in a few cases. Here we adopt this scheme to classify YSOs detected in all four IRAC bands. The [5.8]-[8.0] color is insensitive to reddening and is effective at distinguishing between highly reddened background stars with photospheric emission only and young stars with circumstellar material. Thus we require  $[5.8] - [8.0] > 0.2$  for all the identified YSOs. Bright nebulosity dominated by hydrocarbon emission features can be found in all the regions and have a very red [5.8]-[8.0] color.

To assess the impact of nebulosity on creating false detections, we added artificial stars to each of the mosaics. Each artificial star was 10 pixel ( $12''$ ) to the west of an actual source that was detected in the 3.6 and 4.5  $\mu\text{m}$  bands, and the magnitude of the artificial star in all four IRAC bands was set to the 3.6  $\mu\text{m}$  magnitude of the actual source. Thus, the artificial stars had  $[3.6] - [4.5]$  and  $[5.8] - [8.0]$  colors equal to 0. These sources accurately sampled the range of magnitudes and background nebulosities found in the image. We then recovered the photometry to determine how many such stars would be mistaken as having infrared excesses due to the nebulosity. Although there were about 10 to 30 sources with  $[5.8] - [8.0] > 0.2$ , only 1 to 3 of the sources had a color of  $[3.6] - [4.5] > 0.2$ .

Hence we require  $[3.6] - [4.5] > 0.2$  to eliminate pure photospheres contaminated by hydrocarbon emission nebulosity. Figure 1a shows the [3.6]-[4.5] vs. [5.8]-[8.0] diagram for objects merged from all 9 regions and detectable in all four IRAC bands. In this diagram, objects with  $0.2 < [3.6] - [4.5] < 0.8$  and  $0.4 < [5.8] - [8.0] < 1.1$  are classified Class II; objects with  $[3.6] - [4.5] > 0.8$  and  $[5.8] - [8.0] > 0.2$ , or,  $[3.6] - [4.5] \geq 0.4$  and  $[5.8] - [8.0] > 1.1$  are classified protostars (including Class 0 and Class I objects); while objects with  $[5.8] - [8.0] > 1.1$ , which is consistent with that of protostars, but with  $0.2 < [3.6] - [4.5] < 0.4$ , which is lower than that of protostars, are classified class I/II. For those detected in the 24  $\mu\text{m}$  band, we re-examine them in the IRAC-MIPS diagram.

From both observations and model calculations, the [3.6]-[4.5] vs [5.8]-[8.0] diagram has been proven quite effective in separating YSOs with dusty disks or envelopes from purely photospheric emission stars (Hartmann et al. 2005; Robitaille et al. 2006). The principal ambiguity for the [3.6]-[4.5] vs [5.8]-[8.0] classification scheme lies in distinguishing protostars from class II objects. From the direction of the reddening vector in Figure 1a, the identified protostars immediately above the class II rectangle ( $0.8 \lesssim [3.6] - [4.5] \lesssim 1.2$ ) are likely reddened class II objects. In addition, some of the objects immediately right to the class II rectangle ( $1.1 \lesssim [5.8] - [8.0] \lesssim 1.5$ ), which are identified as protostars or class

I/II, are likely class II objects contaminated by hydrocarbon emission. In addition, some intrinsic characteristics of YSOs make the classification ambiguous as well. For example, geometric effects including bipolar outflow cavities, flattened pattern of envelopes and pole-on geometry will all make the IRAC colors of protostars much bluer (Hartmann et al. 2005; Robitaille et al. 2006). In a few cases the discrimination between class II objects and class III/field stars is also ambiguous; some YSOs with circumstellar disks have an evacuated or very optically thin inner hole and show little infrared excess shortward of  $8.0 \mu\text{m}$  and then can be misidentified as class III/field stars.

### 3.1.2. 2MASS-IRAC diagrams

The IRAC 5.8 and  $8.0 \mu\text{m}$  bands are far less sensitive than the  $3.6$  and  $4.5 \mu\text{m}$  bands (see the limiting magnitudes in Table 2), and are often dominated by bright nebulosity in observations of active star forming regions. For this reason, we combine the IRAC photometric results with data from the 2MASS  $JHKs$  Point Source Catalog. We limit the  $JHKs$  photometric uncertainty to be less than 0.1 mag. Since the  $4.5 \mu\text{m}$  band is the most sensitive band to YSOs among all four IRAC bands (Gutermuth et al. 2004), we use the  $J - H$  vs.  $H - [4.5]$  and  $H - Ks$  vs.  $Ks - [4.5]$  diagrams (Figures 1b, 1c) to identify objects with infrared excess emission but not detected in the IRAC longer wavelength bands. In Figures 1b and 1c, objects with the  $H - [4.5]$  or  $Ks - [4.5]$  colors more than  $1\sigma$  beyond the reddening vectors are identified as objects with intrinsic infrared excess. The extinction law in the mid-infrared wavelengths toward star-forming regions, in particular toward distant high-mass star forming regions, has not been well established. Most recently, Flaherty et al. (2007) derived the interstellar extinction laws in IRAC bands toward five nearby star-forming regions. We adopt the average of the extinction laws derived by Flaherty et al. for our sample. From the dispersion of the objects left to the reddening vectors in these two diagrams, it seems the adopted reddening law is applicable for our high-mass star forming regions. The positions offsets of the reddening vectors in these two diagrams, which were determined by Winston et al. (2007) for Serpens, also appear to be a good approximation for our regions. However, the completeness of the YSOs identification from these two diagrams are significantly limited by the modest sensitivity of the 2MASS survey. Deeper near-infrared observations will not only improve the completeness but also help to derive a more accurate reddening law toward each region, which would improve the reliability of the YSOs identification.

### 3.1.3. IRAC-MIPS diagram

Including data at wavelengths longward of  $20\ \mu\text{m}$  is valuable for more reliable classification of YSOs (Robitaille et al. 2006). In Figure 1d, we use the [3.6]-[4.5] vs. [4.5]-[24] diagram to classify YSOs which are detectable both in the two most sensitive IRAC bands and in the MIPS  $24\ \mu\text{m}$  band. Sources with spectral indexes greater than -0.3 have IRAC-MIPS colors  $[3.6] - [4.5] > 0.652$  and  $[4.5] - [24] > 4.761$ . These sources would include both the flat spectrum and class I objects in the classification scheme of Greene et al. (1994). In addition, the high sensitivity of *Spitzer* data allows for the detection of previously identified class 0 sources in mid-infrared (Noriega-Crespo et al. 2004a; Rho et al. 2006; Hatchell et al. 2007; Winston et al. 2007); consequently, class 0 sources can also be identified by these criteria. Since an infalling envelope is required to explain the SEDs of flat spectrum, class I and class 0 sources (Calvet et al. 1994; Whitney et al. 2003), we refer to the combined set of these sources as protostars. In Figure 1d, there is clearly an isolated group close to (0, 0). The objects in this group are class III/field stars whose emission is dominantly from photospheres. In this diagram objects outside of the protostar region and not in the class III/field star group are classified as class II. There is an obvious gap between protostars/class II objects and class III/field stars, suggesting this diagram is very effective in distinguishing YSOs with circumstellar materials from purely photospheric objects. From the objects that can be classified both in the [3.6]-[4.5] vs. [5.8]-[8.0] and in the [3.6]-[4.5] vs. [4.5]-[24] diagrams, we find that the two classification schemes are in general consistent, otherwise we adopt the latter if there is an ambiguity. With the IRAC-MIPS diagram we also identify 15 class II objects and 2 protostars that cannot be identified in any of the other three color-color diagrams.

### 3.1.4. Removing extragalactic contaminants

There are mainly two classes of extragalactic contaminants that can be misidentified as YSOs (Stern et al. 2005). One is star forming galaxies and narrow-line active galactic nuclei (AGN) which have growing excess at  $5.8$  and  $8.0\ \mu\text{m}$  due to hydrocarbon emission. The other is broad-line AGN which have IRAC colors very similar to that of bona fide YSOs. Gutermuth et al. (2007) have developed a method based on the Boötes Shallow Survey data to substantially mitigate these contaminants. In this method, hydrocarbon emission sources, including galaxies and narrow-line AGN, can be eliminated by their positions in the [4.5]-[5.8] vs. [5.8]-[8.0] and [3.6]-[5.8] vs. [4.5]-[8.0] diagrams, while broad-line AGN, which are typically fainter than YSOs in the *Spitzer* bands, are identified by their positions in the [4.5] vs. [4.5]-[8.0] diagram. Here we adopt this method and lower the [4.5] limit in the [4.5]

vs. [4.5]-[8.0] diagram by 1 mag since our regions are far more distant. To further remove AGN, we set  $[3.6] < 16$  for YSOs not detected in the  $8.0 \mu\text{m}$  band and require  $[24] < 8.5$  for those only identifiable in the [3.6]-[4.5] vs. [4.5]-[24] diagram. We filter out a total of 11 extragalactic contaminants in all nine regions.

### 3.1.5. Completeness of the census

Although we are undertaking deep observations toward relatively nearby high-mass star forming regions, the completeness of the YSOs census is limited by a few factors. Bright extended nebulosity in the IRAC bands can be found in all the regions, which significantly limit the point source detection in these areas. The YSOs identification from the 2MASS-IRAC diagram is limited by the modest sensitivity of the 2MASS survey, while that from the IRAC-MIPS diagram suffers from the significant saturation in the MIPS  $24 \mu\text{m}$  image caused by the central luminous sources. To further evaluate the completeness of the census quantitatively, we plot histograms of the sources which are counted within 0.5 mag bins of the  $3.6 \mu\text{m}$  photometry in Figure 3. In this plot, all the  $3.6 \mu\text{m}$  detections with signal to noise ratios sufficient to be identified by our point source filter are plotted with the gray solid lines, and sources with corresponding multi-band photometry so that they can be placed on one or more color-color diagrams for an assessment of infrared excess are plotted with the dark dashed lines. The identified YSO members are also plotted with the gray dotted lines. There are two types of completeness in this diagram. The first is the completeness in the  $3.6 \mu\text{m}$  band, which declines strongly where a peak is evident in the solid gray line histogram. The second is the coupled multi-band completeness to infrared excess sources, which is approximately given where the dark dashed line diverges from the solid gray line. Since the  $3.6 \mu\text{m}$  band detects sources of fainter magnitudes than the other bands, we define the completeness magnitude as the point where the multi-band histogram declines more than 30% with respect to the  $3.6 \mu\text{m}$  histogram. A vertical dash-dotted line in each plot indicates the completeness magnitude. For sources with the  $3.6 \mu\text{m}$  photometry brighter than the completeness magnitude, we calculate the ratio of the number of sources that can be placed on one or more color-color diagrams for the search of infrared excess to the number of the total detections (Table 4). The actual completeness to infrared excess sources is presumably higher since they will have stronger emission in the IRAC bands than field stars and young stars without disks.

### 3.2. Central Massive Star formation Sites

Previous interferometric studies have identified dusty cores at the center of each region through the millimeter continuum emission, and so far five regions show multiple or a cluster of dusty cores. Of these millimeter sources, the deep IRAC imaging detects six at  $8.0\text{ }\mu\text{m}$ , five at  $5.8\text{ }\mu\text{m}$ , three at  $4.5\text{ }\mu\text{m}$ , and two at  $3.6\text{ }\mu\text{m}$ . The low detection rate is consistent with the deep IRAC observations of the other two nearby (1.7 kpc) high-mass star forming regions, NGC 6334 I and NGC 6334 I(N), where only one out of eleven SMA 1.3 mm sources shows a detectable infrared counterpart (Hunter et al. 2006). Kumar & Grave (2007) suggested that the IRAC band emission of candidate massive protostellar objects arises from the luminous envelopes around the protostars rather than their photospheres or disks. In our sample, the number of detected infrared counterparts increases with the increasing wavelength of the band, despite the fact that the  $3.6$  and  $4.5\text{ }\mu\text{m}$  bands are much more sensitive than the  $5.8$  and  $8.0\text{ }\mu\text{m}$  bands. This implies a steeply rising SED in the IRAC bands, which is consistent with the interpretation that the emission is mostly coming from the dense envelopes. All the six millimeter sources detected in one or more IRAC bands appear significantly saturated in the MIPS  $24\text{ }\mu\text{m}$  band, while there are two millimeter sources detected at  $24\text{ }\mu\text{m}$  without saturation but undetectable in any of the four IRAC bands. We list the IRAC or MIPS  $24\text{ }\mu\text{m}$  photometry of detected millimeter sources in Table 5. In our sample, high-mass stars deeply embedded in dusty cores are early-B types estimated from far-infrared luminosities, ionizing UV radiation fluxes (if UC HII regions detected), and core masses. Also considering they are associated with molecular outflows indicative of active accretion, we refer to these deeply embedded B stars as proto-B stars.

In all nine regions, massive molecular outflows have been identified in millimeter lines of CO and/or SiO. In the IRAC observations, the central high-mass sources are found to be associated with extended nebulosity. Several mechanisms produce extended nebulosity in the IRAC bands. Prominent features from hydrocarbons appear in the  $3.6$ ,  $5.8$ , and  $8.0\text{ }\mu\text{m}$  bands, with the strongest emission features in the  $8.0\text{ }\mu\text{m}$  band (Werner et al. 2004). Vibrational and rotational  $\text{H}_2$  lines appear in all four bands, with the weakest and most spatially confined emission in the  $3.6\text{ }\mu\text{m}$  band (Smith et al. 2006; Smith & Rosen 2005); this  $\text{H}_2$  emission is most apparent in the  $4.5\text{ }\mu\text{m}$  band due to the high sensitivity of this band and presence of strong rotational lines (Smith & Rosen 2005). Finally scattered light may also produce nebulosity which is expected to be the strongest in the  $3.6\text{ }\mu\text{m}$  band. To distinguish between these different mechanisms, we employ  $3.6/4.5\text{ }\mu\text{m}$  two-color and  $3.6/4.5/8.0\text{ }\mu\text{m}$  three-color composite images to highlight emission from shocked  $\text{H}_2$  in outflows, scattered light from outflow cavities, and emission from UV heated hydrocarbons. We identify a total of twelve outflows in eight out of the nine regions. Reflection nebulae and externally heated rimmed clouds are detected as well.

In the following subsections, we discuss each region separately. For Figures 4 to 16, the 3.6, 4.5 and 8.0  $\mu\text{m}$  emissions in color composites are coded in blue, green and red, respectively; millimeter continuum cores from previous observations are marked as plus signs; CO and SiO outflows from previous observations are shown in contours; additional symbols (arrows, dashed curves, etc.) are merely to highlight the IRAC outflows from the ambient reflection nebulae or scattered light.

### 3.2.1. *AFGL 5142*

In Figure 4a, a short jet in the east and a long jet in the west are detected. The short jet coincides with the axis of one of the three jet-like molecular outflows detected in the CO (2-1) and SO ( $6_5 - 5_4$ ) with the SMA (outflow B in Zhang et al. 2007, see contours in Figure 4b). The long jet, on the other hand, coincides with the axis of an extended remnant outflow detected in CO (2-1) with the CSO telescope (Hunter et al. 1995). The emission from these two jets is most prominent in the 4.5  $\mu\text{m}$  band, in agreement with the previous ground-based 2.12  $\mu\text{m}$   $\text{H}_2$   $v=1-0$   $S(1)$  observations (Hunter et al. 1995; Chen et al. 2005). Apparently the IRAC imaging of this region reveals internal driving agents of two molecular outflows.

Toward the center of AFGL 5142, Zhang et al. (2007) detected five millimeter continuum sources (MM1 to MM5 in Figure 5). In Figure 5, a bright source residing  $0.^{\circ}8$  northwest to MM1 (marked with a star symbol) is detected in the 2MASS  $K_s$  band, all four IRAC bands and MIPS 24  $\mu\text{m}$  band (see the detection at  $\alpha(\text{J2000.0}) = 05^{\text{h}}30^{\text{m}}47.98^{\text{s}}$ ,  $\delta(\text{J2000.0}) = 33^{\circ}47'54.9''$  in Table 3). It is classified as a protostar in the [3.6]-[4.5] vs. [5.8]-[8.0] and [3.6]-[4.5] vs. [4.5]-[24] diagrams. The projected offset between this source and MM1 is marginally within the IRAC astrometry allowance. Thus it is still possible that this source is the infrared counterpart of MM1. However, Zhang et al. (2007) detected a forest of molecular lines toward MM1 and suggested it to be the driving source of a jet-like molecular outflow, which implies that the protostar deeply embedded in MM1 is actively accreting. Such a protostellar core is usually obscured in  $K$  band (e.g. Walther et al. 1990; Aspin et al. 1991, and observations of other regions in our sample). Considering the source is detected in the 2MASS  $K_s$  band, a survey with limited sensitivity, we suggest that it is most likely a different source rather than the infrared counterpart of MM1. But the 24  $\mu\text{m}$  emission can still arise from MM1 and/or other millimeter sources given its relatively low resolution ( $\sim 5''$ ), thus we list the 24  $\mu\text{m}$  photometry in Table 5. The 24  $\mu\text{m}$  detection is located at the bright PSF wing of a nearby saturated source, resulting in a potential overestimate of the flux by about 0.3 to 0.4 Jy. The driving sources of the multiple CO/SO outflows have not been unambiguously identified. Zhang et al. (2007) suggested MM3 may be the powering source of the CO outflow

coincident with the short jet in Figure 4b. The long jet is apparently powered by a relatively more evolved young B star (denoted by a blue cross in Figure 2a).

### 3.2.2. *IRAS 05358+3543*

In Figure 6, three highly collimated jets emanating from a group of millimeter continuum sources are detected in the central part of IRAS 05358+3543 (hereafter referred as IRAS 05358). Jet1 coincides a well collimated outflow in CO (1-0) reported by Beuther et al. (2002) (see contours in Figure 6). Jet2 coincides with the axis of a high-velocity CO outflow (outflow B in Beuther et al. (2002)). Several knots from these two jets are almost exactly coincident with the previously identified  $2.12\text{ }\mu\text{m}$   $\text{H}_2$  knots (Porras et al. 2000; Jiang et al. 2001; Beuther et al. 2002; Kumar et al. 2002). Beuther et al. (2002) did not report the identification of Jet3, but weak emission features coincident with this jet can be found in their  $2.12\text{ }\mu\text{m}$   $\text{H}_2$  image. Kumar et al. (2002) suggested the existence of this jet, but the emission appears to be weaker since their  $\text{H}_2$  observations are less deep than that of Beuther et al. (2002). In the IRAC imaging (Figure 6), a chain of emission knots in this jet can be identified and even its tip can be identified despite the contamination by a nebulous knot. There is no reported detection of an outflow toward this jet in millimeter CO or SiO observations. However, in the northern lobe of the SiO (2-1) outflow proposed by Beuther et al. (2002) (their Fig. 8b), the highest contours show elongation coincident with Jet3. Considering SiO is a good shock tracer at (sub)millimeter wavelengths, the elongated SiO emission could be at least partially powered by Jet3.

At the center of this region, Beuther et al. (2002, 2007) detected three millimeter continuum sources at  $\sim 2 - 3''$  resolutions (marked as MM1 to MM3 in Figure 7). The brightest emission feature in Figure 7 coincides with MM1; two northern “red” features (denoted by two white dashed circles) are not real but “bandwidth” artifacts. An investigation of the emission in individual bands shows that emission features coincident with MM2 and MM3 are discernible in the  $3.6$  and  $4.5\text{ }\mu\text{m}$  bands but is not identified by our point source filter. The emission feature coincident with MM1 is marginally discernible in the  $3.6\text{ }\mu\text{m}$  band, and identified as a point source longward of  $4.5\text{ }\mu\text{m}$ . The MIPS  $24\text{ }\mu\text{m}$  emission from this area is significantly saturated. From its extremely red IRAC colors ( $[4.5]-[5.8] = 1.33$  and  $[5.8]-[8.0] = 1.15$ ) and position coincidence with MM1, we suggest this source to be the infrared counterpart of MM1 and list its photometry in Table 5. At higher resolutions ( $\lesssim 1''$ ), the MM1 core splits into two sub-cores at  $875\text{ }\mu\text{m}$  and  $1.2\text{ mm}$  (Beuther et al. 2007). One of the two sub-cores coincides with a point source at  $7.9\text{ }\mu\text{m}$  detected with the Gemini North telescope (Longmore et al. 2006). The sub-structure of MM1 cannot be resolved in the IRAC obser-

vations. The flux of 0.586 Jy at  $8.0\text{ }\mu\text{m}$  ( $[8.0] = 5.098$ ) is consistent with the flux of 0.68 Jy at  $7.9\text{ }\mu\text{m}$  reported in Longmore et al. (2006), suggesting that the flux of the IRAC source is dominated by the sub-core coincident with the  $7.9\text{ }\mu\text{m}$  detection. MM1 (or more precisely, one of the two sub-cores in MM1) is suggested to be the driving source of Jet1 (Beuther et al. 2007). A reliable one-to-one association between Jet2, Jet3 and any two millimeter sources in this region cannot be established with the current data.

### 3.2.3. G192.16-3.82

Shepherd et al. (1998) detected a west-east bipolar outflow in CO (1-0) in G192.16-3.82 (hereafter referred as G192). The eastern lobe of this outflow is detected in the 3.6 and 4.5  $\mu\text{m}$  bands. In Figure 8, the most prominent features of this lobe are “green” nebulosities within the area outlined by two dashed lines. The emission to the west of these features is confused by the bright reflection nebula, but a “blue” V-shaped structure, with the millimeter source at the tip, is still discernable in the three-color composite of the field (Figure 2c). The overall structure of the eastern lobe in the IRAC imaging, i.e., the “green” features as well as the V-shaped inner part, roughly coincides with but far exceeds the eastern lobe of the CO outflow. The prominence in the 4.5  $\mu\text{m}$  band and coincidence with previous H $\alpha$  and [SII] detections (Devine et al. 1999) strongly suggest that the “green” nebulosities are shock excited H $_2$  knots. The base of the western lobe of the CO outflow is also detected in the IRAC imaging, with the prominent feature being a candle-flame-shaped structure (delineated by a dashed curve in Figure 8, but more prominent in Figure 2c); this structure is previously detected in the  $K$ -band imaging (Shepherd et al. 1998; Devine et al. 1999). One interesting aspect of this outflow is that although the eastern lobe is filled with shocked H $_2$  knots, a collimated component cannot be found either in our IRAC imaging or previous observations. The CO outflow appears to be driven by a wide-angle wind revealed in the IRAC, H $\alpha$  and [SII] observations.

A proto-B star surrounded by an UC HII region and embedded in a dense dusty core was suggested to be the driving source of the outflow (Shepherd et al. 1999, 2004a). A bright source coincident with the millimeter continuum peak is detected in the IRAC bands and show very red IRAC colors (Figure 9). We suggest it to be the infrared counterpart of the millimeter source and list its photometry in Table 5. A detailed comparison between the infrared and millimeter emission in the region will be presented in a future work (Shepherd et al., in prep.).

### 3.2.4. HH 80-81

An extraordinarily well-collimated and powerful radio jet was previously detected in HH 80-81 (Martí et al. 1993, 1995, 1998, see contours in Figure 10). Having the radio jet right at the axis, the *Spitzer* data for the first time reveals a bipolar cone-shaped cavity with its emission most prominent in the  $8.0 \mu\text{m}$  band with an extent of about 4pc (Figure 10). Low-mass protostellar outflows are often found to consist of two components, with an axial narrow jet-like component surrounded by a wide-angle biconical component (Lee et al. 2006; Palau et al. 2006). It is unclear whether outflows emanating from high-mass young stars or protostars may exhibit two components similar to low-mass outflows. Our IRAC imaging as well as previous radio continuum observations of the HH 80-81 outflow provides the best case of a two-component outflow emanating from a  $10^4 L_\odot$  source. The remarkable prominence in the  $8.0 \mu\text{m}$  band suggests that the emission of the IRAC biconical structure is from hydrocarbons heated by UV photons from the central source. Single-dish observations revealed a large bipolar outflow in CO (1-0) (Yamashita et al. 1989; Benedettini et al. 2004), with the northern lobe being blueshifted and the southern lobe redshifted. The orientation of the CO outflow is roughly consistent with the IRAC outflow structure. In the three-color composite image (Figure 2d), a curved structure in the northern lobe stands out in the  $3.6 \mu\text{m}$  emission (blue). This curved structure is very bright in previous near-infrared *K*-band observations and has been suggested as the wall of a parabolic cavity (Aspin et al. 1991). The dominant  $3.6 \mu\text{m}$  emission from this structure may be partly explained by the scattered light in this structure being enhanced by forward scattering and lower extinction. The  $8.0 \mu\text{m}$  emission within this structure is spatially limited to the inner edge of the parabolic wall. This may suggest that part of the northern lobe cavity is shielded from the UV photons by gas and dust in the outflow and perhaps by the circumstellar environment around the central source. Two additional reflection nebulae are found on both sides of the bipolar cavity; these appear to be heated by two young B stars (see Table 3) and not directly connected to the outflow cavity.

The central driving source of the outflow has been detected in the centimeter (Martí et al. 1993, 1999) and millimeter (Gómez et al. 2003) continuum. Mid-infrared emission from this source has been detected at  $4.7$  to  $13 \mu\text{m}$  in the ground-based observations (Aspin et al. 1994; Stecklum et al. 1997). In Figure 11, the centroid of the emission feature in the  $3.6 \mu\text{m}$  band is about  $2''$  northeast offset from the millimeter peak. This feature coincides with a *K*-band knot detected in previous ground-based observations (their IRS 2, Aspin et al. 1991, 1994; Stecklum et al. 1997). From its high polarization and relatively large FWHM, Aspin et al. (1991) argued that it is a nebulous knot of gas/dust rather than a point source. The emission feature in the  $4.5 \mu\text{m}$  band shows elongation toward the position of the millimeter peak. The centroid of the emission feature in the  $5.8$  and  $8.0 \mu\text{m}$  bands, discarding the “bandwidth”

artifact in the north, coincides with the millimeter peak. We suggest that the emission in the 3.6 and 4.5  $\mu\text{m}$  bands is mostly attributed to the IRS 2 knot, while that in the long wavelength bands is mostly coming from the millimeter core and their photometry is listed in Table 5. The MIPS 24  $\mu\text{m}$  emission in the central part of this region is significantly saturated.

### 3.2.5. *IRAS 19410+2336*

As outlined with a dashed ellipse in Figure 12, an elliptical nebula orientated in the northeast-southwest direction can be identified from the extended emission in the central part of IRAS 19410+2336 (hereafter IRAS 19410). In interferometric CO observations, multiple outflows emanating from the center of this region show very complex morphologies (Beuther et al. 2003). The axis of one outflow proposed by Beuther et al., which is shown in contours in Figure 12, coincides with the major axis of the IRAC elliptical nebula. Jet-like 2.12  $\mu\text{m}$  H<sub>2</sub> emission along the axis of this outflow was detected as well (Beuther et al. 2003). The elliptical nebula, with two local cavities at the ends of the major axis, is only detectable in the 3.6 and 4.5  $\mu\text{m}$  bands and appears more prominent in the 3.6  $\mu\text{m}$  band, suggesting the emission is dominated by scattered light from the central source. Apparently the IRAC imaging of the IRAS 19410 outflow reveals a less collimated component than the 2.12  $\mu\text{m}$  H<sub>2</sub> jet.

The driving source of this outflow is suggested to be deeply embedded in a dusty core traced by millimeter continuum emission at a resolution of  $5.5'' \times 3.5''$  (Beuther et al. 2003). The infrared emission from this millimeter source is detected in all four IRAC bands and the photometry is listed in Table 5. There is a 2MASS *Ks* band detection, with the photometry of  $10.802 \pm 0.044$ , at  $\sim 0.7''$  away from the millimeter continuum peak. As we discussed in §3.2.1, it is more likely another star rather than the infrared counterpart of the millimeter source. The MIPS 24  $\mu\text{m}$  emission from the source is significantly saturated. At a higher resolution ( $1.5'' \times 1''$ ), the millimeter core splits into multiple sources (Beuther & Schilke 2004a); our IRAC observations cannot resolve those sources. A detailed comparison between the IRAC observations and high-spatial-resolution millimeter continuum observations of this region will be presented in a future work (Rodon et al., in prep.).

### 3.2.6. *IRAS 20126+4104*

In Figures 13a & 13c, a bipolar outflow in IRAS 20126+4104 (hereafter referred as IRAS 20126) is detected as a limb-brightened biconical cavity. The cavity structure, in particular the wall of the northwestern lobe, is clearly detected in the 3.6, 4.5, and 5.8  $\mu\text{m}$  bands and its prominence in the 3.6 and 4.5  $\mu\text{m}$  bands suggests that the emission is dominated by the scattered light. The molecular outflow in IRAS 20126 has been interpreted as driven by a precessing jet based on the S-shaped locus of the 2.12  $\mu\text{m}$   $\text{H}_2$  knots and the orientation variation between the inner jet-like SiO outflow and the larger CO outflow (Cesaroni et al. 1997, 1999; Shepherd et al. 2000; Lebrón et al. 2006; Su et al. 2007). The jet-precessing scenario is also consistent with the presence of a double system detected at centimeter and near-infrared wavelengths (Sridharan et al. 2005; Hofner et al. 1999, 2007). Our IRAC observations put new insight into the outflow property of this luminous source. The IRAC biconical structure far exceeds inner SiO outflow and covers part of the larger CO outflow. From the limb-brightening, the cavity wall has PAs from  $\sim -33^\circ$  to  $\sim -65^\circ$ . The PA  $\sim -33^\circ$  wall is significantly offset from the axis of the larger CO outflow which is nearly in a N-S orientation (Shepherd et al. 2000; Lebrón et al. 2006), while the PA  $\sim -65^\circ$  wall has an approximately same orientation as the jet-like SiO outflow. A natural interpretation of the cavity (with the limb-brightening) is that it traces a less collimated biconical component of the IRAS 20126 outflow, rather than being swept up by a jet precessing from N-S to the current-position of PA  $\sim 33^\circ$ . However, in contrast to the HH 80-81 outflow (§3.2.4), the jet component in this region coincides with the wall, not the axis, of the biconical cavity. While multiple outflows can be one possibility, another possibility can be derived by adopting the precessing scenario and the theoretical model unifying the jet-driven and wind-driven low-mass outflows (Shang et al. 2007): when the underlying axial jet and the co-existing wind are precessing, the dense jet is more efficient in entraining a collimated molecular outflow via strong shock activities, while the cavity evacuating by the more tenuous wind component is less efficient. Consequently, the jet-like SiO outflow can be detected very close to the current-position of the precessing jet while the cavity revealed by the scattered light more or less lags behind.

A dense dusty core, which harbors a proto-B star driving the outflow, was previously detected in the millimeter continuum (Shepherd et al. 2000; Cesaroni et al. 2005). In the 4.5 and 5.8  $\mu\text{m}$  bands the emission feature coincident with the millimeter source is discernible. In the 8.0  $\mu\text{m}$  band (Figure 13b), a point source at this position is detected and the photometry is listed in Table 5. At higher resolutions ( $\lesssim 0.5''$ ), two emission regions oriented along the outflow axis and separated by a dark lane were detected at near- and mid-infrared wavelengths (Sridharan et al. 2005; De Buizer 2007). The source in the 8.0  $\mu\text{m}$  band may encompass the previously detected double sources.

### 3.2.7. *IRAS 20293+3952*

In Figure 14, ahead of a previously detected high-velocity CO outflow (Beuther et al. 2004b), a short jet is detected in the IRAC imaging with an extent of about  $10''$ . with the most prominent emission in the  $4.5 \mu\text{m}$  band. In orientation the IRAC jet well coincides with the CO outflow. This outflow was also detected in thermal emissions of SiO and  $\text{CH}_3\text{OH}$  (Beuther et al. 2004b; Palau et al. 2007), which often trace shock activities in outflows. In the previous  $2.12 \mu\text{m}$   $\text{H}_2$  observations, the overall structure was not detected but a faint knot can be found at the southeastern end of the IRAC jet (knot “C” in Fig. 2 of Kumar et al. (2002)). We suggest that the IRAC imaging for the first time reveals the interval driving agent of the CO/SiO/ $\text{CH}_3\text{OH}$  outflow.

A millimeter continuum source, which may harbor an intermediate-mass protostar, is suggested to be the driving source of the CO/SiO/ $\text{CH}_3\text{OH}$  outflow (Beuther et al. 2004b,c; Palau et al. 2007). The infrared emission from the millimeter source is only detected in the MIPS  $24 \mu\text{m}$  band (Table 5). As the case of AFGL 5142 (§3.2.1), the  $24 \mu\text{m}$  detection is located at the bright PSF wing of a nearby saturated source, resulting in a potential overestimate of the source flux by about 0.8 to 0.9 Jy.

### 3.2.8. *W75 N*

In Figure 15, multiple bow-shaped structures in W75 N can be identified. The most remarkable one, marked by the double arrows, form a large scale bipolar bow-shaped structure. The shell of the southwestern lobe and the tip of the northeastern lobe of this structure is clearly revealed in the  $4.5 \mu\text{m}$  band. This bow-shaped structure has previously been detected in the  $2.12 \mu\text{m}$   $\text{H}_2$  imaging by several authors (Davis et al. 1998; Shepherd et al. 2003; Davis et al. 2007), but not reported in previous IRAC observations toward the DR 21/W75 N region carried out during the science verification period of *Spitzer* (Persi et al. 2006; Davis et al. 2007), probably because their observations are far less deep in integration. The southwestern lobe coincides with the boundary of the redshifted lobe of a large outflow detected in CO (1-0) (Shepherd et al. 2003), suggesting the bow-shock-driven nature of this molecular outflow. In addition to this remarkable structure, at least five bow-shaped structures pointing to the southeast of the region can be found in Figure 15. These structures may be shocked  $\text{H}_2$  “fingers” tracing multiple bow-shocks driven from the center of the region, roughly in a fashion similar to the famous  $\text{H}_2$  “fingers” in the Orion KL region (Schultz et al. 1999; Nissen et al. 2007). Zooming in on the inner part of this region, the IRAC imaging reveals a new bow-shaped structure (outlined by a solid curve in Figure 16). This structure is clearly detected in the  $3.6$  and  $4.5 \mu\text{m}$  bands and appears more prominent

in the  $4.5 \mu\text{m}$  band (Figures 16a, 16b). Its orientation approximately coincides with the axis of a CO outflow proposed by Shepherd et al. (2003).

At the center of the large northeast-southwest bow-shaped structure, Shepherd (2001) detected a group of four millimeter continuum sources (labelled as MM1 to MM4 in Figure 16a). Embedded in MM1 is a cluster of four centimeter continuum sources, with three within an area of  $1''5$  and another about  $3''$  to the south (Figure 16c, Hunter et al. 1994; Torrelles et al. 1997; Shepherd et al. 2003). Of the four centimeter sources, the northernmost one was interpreted as an ionized radio jet while the other three were suggested to be UC H<sub>II</sub> regions excited by proto-B stars. It is still unclear which is driving the large scale CO outflow. Shepherd et al. (2003) suggested the first UC H<sub>II</sub> region from the north (namely VLA 2) is likely to be the driving source. The resolution of our IRAC observation does not allow us to shed any further light on this issue. Shepherd et al. (2003) suggested the second UC H<sub>II</sub> region from the north (namely VLA 3) to be the driving source of the CO outflow whose axis approximately coincides with the newly discovered small bow-shaped structure in the IRAC image. However, the CO outflow is very compact and confined to within  $\sim 5''$  from MM1 while the bow-shaped structure is about  $50''$  (0.5 pc in projection) away from the group of the millimeter sources. In projection MM3 is closer to the axis of this bow-shaped structure and thus more likely to be the driving source of this structure. The infrared emission from MM1 is marginally discernible in the  $3.6 \mu\text{m}$  band (Figure 16a). From  $4.5$  (Figure 16b) to  $8.0 \mu\text{m}$  it is clearly identified as a point source, and the photometry is listed in Table 5. The MIPS  $24 \mu\text{m}$  emission from the source is significantly saturated.

### 3.2.9. *IRAS 22172+5912*

IRAS 22172+5912 (hereafter IRAS 22172) is the only region in our sample toward which no outflow signature is found in the IRAC bands, though a bipolar outflow in CO and HCO<sup>+</sup> has been detected with the OVRO array (Molinari et al. 2002; Fontani et al. 2004). The peak of the dust emission, which was detected in the OVRO 2.6 mm and 3.4 mm continuum observations at  $\sim 4 - 6''$  resolutions, is about  $5''$  offset from the geometric center of the bipolar molecular outflow (Molinari et al. 2002; Fontani et al. 2004). The IRAC and MIPS  $24 \mu\text{m}$  imaging do not detect infrared emission from the millimeter source but reveals two protostars at the center of this field (see Figure 2i). The southern protostar coincides with the geometric center of the CO outflow and thus can be a candidate of the driving source of the outflow. For the millimeter source, the lack of infrared emission shortward of  $24 \mu\text{m}$  and the apparent non-association with the molecular outflow suggest the source to be at a very young evolutionary stage. Further (sub)millimeter continuum and line observations

with high sensitivity and higher resolutions are needed to verify whether it is at a prestellar stage or harbors deeply embedded protostars.

### 3.3. UV Heated Reflection Nebulae and Bright Rimmed Clouds

The IRAC imaging of the sample reveals mainly three classes of extended emission:  $H_2$  emission dominated nebulae most prominent in the  $4.5\ \mu m$  band (green); scattered light dominated nebulae most prominent in the  $3.6\ \mu m$  band (blue); UV heated hydrocarbon emission dominated reflection nebulae most prominent in the  $8.0\ \mu m$  band (red). The first two classes have been discussed in detail in §3.2.

The UV heated reflection nebulae can be found in most regions. While the first two classes of extended emission are found in outflows or outflow cavities and thus imply a very young evolutionary stage of the central source, most of the UV heated reflection nebulae are associated with young but relatively more evolved B stars (one exception being the biconical cavity of the HH 80-81 outflow). For the cometary nebula in AFGL 5142, the southwestern nebula in IRAS 05358, the southeastern and northerwestern nebulae in HH 80-81, the central nebula in IRAS 20293, and the northern and central nebulae in W75 N, a bright source at the center is detected (denoted as a blue cross in Figure 2). These sources show infrared excess in our censes of YSOs based on color-color diagrams, and most of them were previously suggested to be intermediate- to high-mass young stars (see annotation of Tabel 3). They are most likely the exciting sources of the surrounding reflection nebulae. Of these sources, the one in IRAS 20293 shows an UC H $\alpha$  region and the central one in W75 N is surrounded by a relatively extended H $\alpha$  region. The spectral types of the exciting stars of these two H $\alpha$  regions, derived from the Lyman continuum photos required to produce the observed ionized emission, are B1 and B0.5 for that in IRAS 20293 and W75 N, respectively (Palau et al. 2007; Shepherd et al. 2004b). Toward the two sources in HH 80-81, compact centimeter continuum was detected as well (Martí et al. 1993), and the estimated rates of Lyman continuum photos suggest B3 to B2 stars being the exciting sources of these two reflection nebulae. There is no reported detection of a distinct H $\alpha$  region surrounding the other candidate exciting sources. We suggest they are young B stars capable of providing strong FUV radiation to excite hydrocarbon emission but too weak EUV to ionize its environment. Spectroscopic studies are needed to further investigate whether these stars have circumstellar disks and to confirm their spectral types. There are also UV heated reflection nebulae for which an exciting source cannot be identified with the existing data, but the need of FUV photons to heat hydrocarbons and the lack of significant free-free emission also suggest a B type star being the exciting source. To lower the optical depth in FUV and consequently allow the stars to

heat the surrounding hydrocarbons, these B stars must have cleared most of the surrounding gas. On the other hand, as discussed in §3.2, the central massive star formation site in each region shows millimeter continuum cores harboring deeply imbedded proto-B stars. Thus it appears that most regions in the sample are forming B stars at a range of evolutionary stages.

In two regions, IRAS 20126 and IRAS 22172, the central massive star formation sites are embedded in a bright large scale structure which is prominent in the  $8.0\ \mu\text{m}$  band. These two structures are externally heated rimmed clouds.

## 4. Discussion

### 4.1. Clustering

One of the distinctive features of massive star formation is that it occurs in clusters. Consequently, understanding the role of clustering in the formation of high-mass stars is an essential step toward a theory of massive star formation. A controversial issue is whether clusters are necessary for the formation of high-mass stars, or whether clusters are merely the byproduct of the formation of high-mass stars in dense massive molecular cores. In a near-infrared survey of intermediate-mass Herbig Ae/Be stars, Testi et al. (1999) found a smooth transition between the low density aggregates of young stars associated with stars of spectral type A or later, and the dense clusters associated with O and early-B type stars. They argued that the presence of dense clusters is required for the formation of high-mass stars. The smooth transition suggested that there may be a fundamental relationship between the mass of the most massive star and the number and/or density of stars in a cluster. However, de Wit et al. (2005) found evidence that 4% of O stars form in isolation. This is evidence that clusters are not necessary for the formation of O stars, although Parker & Goodwin (2007) argued that the isolated O stars may actually form in small clusters.

To test whether massive stars can form without low-mass stars requires identification of young massive objects without associated clusters of low-mass stars; only in these cases, can we rule out the possibility that an attendant cluster dispersed due to dynamical evolution. In a  $K$ -band survey of eight high-mass star forming cores, Megeath et al. (2004) found one core, NGC 6334 I(North), showing evidence of high-mass star formation without evidence for a cluster of embedded low-mass stars (also see Megeath & Tieftrunk 1999; Hunter et al. 2006), although a cluster may still exist deeply embedded in the cloud (Persi et al. 2005). It is important to search for other potential examples of massive star formation without the presence of a dense cluster. With its ability to identify YSOs through infrared excesses and

detect deeply embedded protostars, *Spitzer* is well suited to this task. Although such regions may yet form clusters, the identification of high-mass young or protostars without a dense cluster would demonstrate that low-mass stars are not required for the formation of massive stars.

Our survey of young intermediate- to high-mass (proto)stars ( $\sim 10^3$  to  $10^5 L_\odot$ ) can directly address the role of clustering in the early stages of intermediate- and high-mass forming stars. The *Spitzer* data provides the ability to directly identify likely YSOs by the detection of mid-infrared excesses. The advantage of this approach over previous near-infrared source counting methods is that the sample does not significantly suffer from contamination by background stars which can be significant for high-mass star forming regions in the Galactic plane (Pratap et al. 1999). Also, the mid-infrared colors are much more sensitive to protostellar objects, and candidate protostellar objects can be identified through their colors. However, the bright mid-infrared nebulosity in high-mass star forming regions, the  $\sim 2 - 3''$  angular resolution of the IRAC data, and the modest sensitivity of the 2MASS photometry limit the detection of sources, in particular in regions of bright nebulosity. We expect the census of YSOs to be incomplete in all of the regions. Furthermore, we expect that a certain fraction of the stars do not have disks and will not be identified in our analysis; the fraction of stars without disks is approximately 30% for 1 Myr old low-mass stars (Hernández et al. 2007).

We group the objects by their total far-infrared luminosity, as measured from the IRAS point source catalog; this luminosity will be dominated by the most massive objects in the regions. In all the regions, associated low-mass YSOs are detected. The  $\sim 10^3 L_\odot$  regions, AFGL 5142, G192, IRAS 05358 and IRAS 20293, show parsec sized clusters with around 20 YSOs surrounded by a more extended and sparse distribution of young stars and protostars. The  $\sim 10^4 L_\odot$  regions IRAS 19410 and HH 80-81 also show clusters and extended components. Except AFGL 5142, the clusters associated with these regions do not show concentrations of stars toward the central massive objects. This may be due to the decrease in completeness toward the bright nebulosities in the central regions. Finally, the  $10^{5.1} L_\odot$  region W75 N shows a cluster that is both richer and more spatially extended. This region also shows a paucity of sources in the bright nebulous center of the region, further indicating the observations are significantly limited by completeness.

In Figure 17 we plot the number of sources as a function of the source luminosity. To mitigate the effects of incompleteness on our samples, we plot the number of sources with  $3.6 \mu\text{m}$  magnitudes lower than 13 and 14. Given a typical  $Ks - [3.6]$  color of 0.25, an extinction of  $A_K \sim 0.25$  at 1.8 kpc, and an age of 1 Myr, these limits correspond to masses of 1.2 and 0.5  $M_\odot$  (Baraffe et al. 1998). The two plots show a trend of increasing number

of associated YSOs with increasing total luminosity. In particular, the number of YSOs in the  $10^{5.1}L_{\odot}$  region (W75 N) is significant higher than those in  $\sim 10^4L_{\odot}$  regions, which again are somewhat higher in number than the  $\sim 10^3L_{\odot}$  regions. It is possible that a trend of increasing incompleteness with higher far-infrared luminosities is decreasing the slope of this trend.

There are two main exceptions to this trend: IRAS 22172 and IRAS 20126. IRAS 22172 appears to be part of a larger, potentially more evolved region which has undergone significant gas clearing. The clearing of the gas would also lower the fraction of light absorbed by dust and re-emitted in the infrared; hence this region shows a large number of stars for its measured IRAS far-infrared luminosity. The other exception is IRAS 20126, which has the lowest number of associated YSOs in the sample. Unlike the other regions, IRAS 20126 shows no obvious cluster in the field. This is unlikely to be solely the effects of incompleteness, with the average signal of about 2.5 MJy/sr at 4.5  $\mu\text{m}$  and 52 MJy/sr at 8.0  $\mu\text{m}$  in the central parsec area, compared to 6.5 MJy/sr at 4.5  $\mu\text{m}$  and 67 MJy/sr at 8.0  $\mu\text{m}$  for HH 80-81 and 3.8 MJy/sr at 4.5  $\mu\text{m}$  and 72 MJy/sr at 8.0  $\mu\text{m}$  for IRAS 19410.

More rigorous studies of this sample await deeper near-infrared data to complement the *Spitzer* 3.6 and 4.5  $\mu\text{m}$  imaging. However, the analysis here already illustrates several features. First, there does seem to be a trend of the number of associated YSOs with luminosity. Second, these regions show both clusters in the central 1 pc as well as more extended halos of sources around the clusters. Finally, there does seem to be a significant dispersion in the number of associated YSOs for a given total far-infrared luminosity, with one luminous source, IRAS 20126, showing no obvious cluster. The lack of a cluster warrants future work; if confirmed this would demonstrate that the formation of  $\sim 10^4L_{\odot}$  sources is not dependent on the presence of deep clusters.

#### 4.2. Outflows and Outflow Cavities

For a sample of nine high-mass star forming regions associated with CO and/or SiO outflows, the deep IRAC imaging reveals outflows and outflow cavities toward eight regions, illustrating that the IRAC imaging can be an effective tool for outflow detection. For the jets in IRAS 05358, AFGL 5142, IRAS 20293, the bow-shock shells in W75 N, and the nebulosities in the eastern lobe of the G192 outflow, the prominence in the 4.5  $\mu\text{m}$  band and coincidence with the ground-based 2.12  $\mu\text{m}$  H<sub>2</sub> detections (if detected in the 2.12  $\mu\text{m}$  H<sub>2</sub> line) suggest the emission is mostly attributed to shocked H<sub>2</sub> emission, although the contribution from H<sub>i</sub> Br $\alpha$  (4.052  $\mu\text{m}$ ), CO v=1-0 (4.45-4.95  $\mu\text{m}$ ) lines cannot be ruled out without spectroscopic observations. A detailed investigation of the emission in the biconical cavity in IRAS 20126

shows strong evidence for the scattered light being dominant in the 3.6 and 4.5  $\mu\text{m}$  bands (Qiu et al., in prep.). The elliptical structure in IRAS 19410 appears relatively diffuse and most prominent in the 3.6  $\mu\text{m}$  band. The emission in this outflow can be dominated by the scattered light as well. The clear prominence of the biconical structure in HH 80-81 suggested is dominated by UV heated hydrocarbon emission.

#### 4.2.1. *An evolutionary picture of massive outflows?*

Both theoretical models and high spatial resolution observations suggest an evolutionary scenario for low-mass outflows: as low-mass stars evolve from class 0 through class I to class II stages, the mass loading in the winds and density structure in the cores conspire the widening of outflows (Fuller & Ladd 2002; Arce & Sargent 2006; Shang et al. 2007). While for massive outflows, whether an evolutionary picture exists is unknown (Beuther & Shepherd 2005).

The detected outflows in the sample show dramatically different morphologies. We detect highly collimated jets, bow-shock shells, and biconical cavities. Given the extreme complexity of the CO observations (Beuther et al. 2003) and relatively confused emission in the IRAC imaging compared with the other regions, we leave out the IRAS 19410 outflow in the following discussion. Considering Jet1 in IRAS 05358, the short jet in AFGL 5142, and the jet in IRAS 20293, the IRAC observations reveal the internal driving agents of well collimated CO outflows in these regions. The powering sources of Jet1 in IRAS 05358 and the short jet in AFGL 5142 are suggested to be deeply embedded proto-B stars, toward which only very weak radio continuum was detected (Beuther et al. 2007; Zhang et al. 2007). The jet in IRAS 20293 is most likely driven by an intermediate-mass protostar showing no detectable centimeter emission (Beuther et al. 2004b). In contrast, the large scale CO outflows in W75 N and G192 appear to be poorly collimated within  $\lesssim 0.5$  pc from the central driving sources. In W75 N, proper-motion observations of water masers by Torrelles et al. (2003) delineated a non-collimated, shell outflow at a 160 AU scale expanding in multiple directions with respect to the UC H $\text{II}$  region VLA 2, which may drive the large scale CO outflow as suggested by Shepherd et al. (2003). The bipolar bow-shaped structure beyond  $\sim 1$  pc detected in the 2.12  $\mu\text{m}$  H $_{\text{2}}$  and the IRAC 4.5  $\mu\text{m}$  imaging could be the remnant of a collimated component. For the G192 outflow, no collimated component can be found within  $\sim 2.4$  pc from the driving source. The proposed central driving sources of these two poorly collimated outflows are found to be surrounded by UC H $\text{II}$  regions. If we adopt the centimeter free-free emission as an indicator of the relative evolution between these sources, there seems to be a trend of evolution for the related outflows: both internal driving agents and entrained molecular outflows appear to be highly collimated for the youngest sources (e.g., IRAS 05358,

AFGL 5142, IRAS 20293); as the central source evolves to form a significant UC H<sub>II</sub> region, only poorly collimated outflow structures can be found around the central driving source (e.g., W75 N, G192).

For the IRAS 20126 outflow, it remains ambiguous whether it is merely composed of a precessing jet and consequently larger structures are all entrained/swept-up by this jet or it has a jet-like component as well as a biconical component with a moderate opening angle. Toward the central driving source of this outflow, very weak centimeter continuum was detected, presumably suggesting the source being at a very young evolutionary stage. For the HH 80-81 outflow, our *Spitzer* data and previous centimeter continuum reveal a remarkable two-component outflow with a biconical cavity surrounding an axial radio jet. Strong centimeter continuum was detected toward the central driving source of the HH 80-81 outflow, presumably suggesting the source being relatively more evolved compared with that of IRAS 20126. The outflow cavity of HH 80-81 also shows emission in the mid-infrared hydrocarbon features, suggesting that UV radiation from the central sources are heating the cavity walls. Therefore, if the IRAC biconical cavity in IRAS 20126 is a complementary less collimated component of the previously detected SiO jet, there will be a large evolutionary time scale for the existence of both a highly collimated jet-like component and a less collimated biconical component for outflows from proto-B stars. With the existing data it is very difficult to determine whether the central source of IRAS 20126 is more evolved than those of AFGL 5142 and IRAS 05358, and whether the central source of HH 80-81 is younger than those of W75 N and G192. Presumably it is likely that the IRAS 20126 and HH 80-81 outflows, with the former being younger, represent evolutionary stages between that of the AFGL 5142 & IRAS 05358 outflows, for which both internal driving agents and entrained gas appear well collimated, and that of the W75 N & G192 outflows, for which only poorly collimated structures can be found around the central driving sources.

However, such a trend is only a tentative interpretation based on current observations of a small sample. The question whether there is an evolutionary picture for massive outflows is far from conclusive, and remains an observational challenge. In high-mass star forming regions, multiple outflows with complicated structures are often detected. Due to relatively larger distances and crowded clustering mode, it is very difficult with the current facilities to reliably identify the driving source of a massive outflow. Also resolving the launching zone of a massive outflow, which is of great importance for investigate driving mechanisms, requires extremely high spatial resolution and high sensitivity. In addition, observations of outflows in more luminous objects ( $L \gtrsim 10^5 L_\odot$ ), in particular high spatial resolution observations, are still rare (the combined bolometric luminosity of UC H<sub>II</sub> regions in MM-1 in W75 N is  $10^{4.6} L_\odot$ ). Extensive and comprehensive studies of outflows in this luminosity regime would be crucial for testing possible evolutionary scenarios of massive outflows and understanding

formation processes of O type stars.

## 5. Summary

We have described initial results of mid-infrared imaging observations toward nine high-mass star forming regions made with the IRAC and MIPS cameras onboard *Spitzer*. The regions were selected for the presence of luminous ( $> 10^3 L_\odot$ ) young objects driving molecular outflows. The observed fields are approximately  $5' \times 5'$ , corresponding to physical widths of  $\sim 2.5 - 3.5$  pc for the source distances ranging from  $\sim 1.7 - 2.4$  kpc.

Using the  $3 - 24 \mu\text{m}$  *Spitzer* photometry in combination with near-infrared 2MASS data, we identify a total of 417 YSOs with infrared excesses attributed to circumstellar disks or envelopes, including at least 12 candidates of intermediate- to high-mass young stars. In most regions, the spatial distribution of these YSOs shows both a cluster component centered on the sites of massive star formation as well as a more extended distribution of YSOs outside the cluster. The number of YSOs grows with the total far-infrared luminosity, with two significant exceptions: IRAS 22172 appears to be part of a larger, more evolved region; IRAS 20126 appears to be a  $10^4 L_\odot$  protostar with only 19 associated YSOs and no central cluster.

Zooming in on the central massive star formation sites, we search for infrared counterparts toward millimeter continuum sources identified in interferometer observations. We detected counterparts for eight millimeter continuum sources in the IRAC bands or MIPS  $24 \mu\text{m}$  band. These eight sources appear to be natal cores of proto-B stars driving molecular outflows. All of the regions of massive star formation have bright associated nebulosity from scattered light, shocked  $\text{H}_2$  and/or UV heated hydrocarbon emission features. This nebulosity limits the completeness of our YSO survey in the central areas.

The deep IRAC imaging detects features associated with 12 outflows in eight of the surveyed regions. Compared with previous ground-based observations, our IRAC observations confirm previous  $2.12 \mu\text{m}$   $\text{H}_2$  jets or bow-shock shaped structures in AFGL 5142, IRAS 05358, and W75 N (the large bow-shock shaped structure), and previous  $\text{H}\alpha/\text{[SII]}$  features in G192; reveal new structures in HH 80-81, IRAS 20126, and IRAS 19410; detect a new  $\text{H}_2$  jet in IRAS 20293 and a new bow-shock shaped structure in W75 N (the small bow-shock shaped structure). In one case, HH 80-81, the inner surface of the outflow cavity shows strong  $8 \mu\text{m}$  emission indicative of hydrocarbons heated by UV radiation. Based on the morphological variations of the detected outflows in conjunction with previous observations, we outline a possible evolutionary picture for massive outflows.

UV heated reflection nebulae dominated by hydrocarbon emission in the 8.0  $\mu\text{m}$  band can be found in most regions. They may imply the presence of relatively more evolved young B stars. Externally heated bright rimmed clouds are found in IRAS 20126 and IRAS 22172.

We are grateful to Luis F. Rodríguez for providing us the VLA cm data on HH 80-81. This work is based on observations made with the *Spitzer* Space Telescope, which is operated by the Jet Propulsion Laboratory, California Institute of Technology under a contract with the National Aeronautics and Space Administration (NASA). This publication makes use of data products from the Two Micron All Sky Survey, which is a joint project of the University of Massachusetts and the Infrared Processing and Analysis Center/California Institute of Technology, funded by NASA and the National Science Foundation. K. Q. acknowledges the support of the Grant 10128306 from NSFC. H. B. acknowledges financial support by the Emmy-Noether-Program of the Deutsche Forschungsgemeinschaft (DFG, grant BE2578).

## REFERENCES

Allen, L. E., Calvet, N., D'Alessio, P., Merin, B., Hartmann, L., Megeath, S. T., Gutermuth, R. A., Muzerolle, J., Pipher, J. L., Myers, P. C., & Fazio, G. G. 2004, *ApJS*, 154, 363

Arce, H. G. & Sargent, A. I. 2006, *ApJ*, 646, 1070

Aspin, C. & Geballe, T. R. 1992, *A&A*, 266, 219

Aspin, C., McCaughrean, M. J., Casali, M. M., & Geballe, T. R. 1991, *A&A*, 252, 299

Aspin, C., Puxley, P. J., Blano, P. R., Piña, P. K., Pickup, D. A., Paterson, M. J., Sylvester, J., Laird, D. C., Bridger, A., Daly, P. N., & Griffin, J. L. 1994, *A&A*, 292, L9

Benedettini, M., Molinari, S., Testi, L., & Noriega-Crespo, A. 2004, *MNRAS*, 347, 295

Beuther, H., Leurini, S., Schike, P., Wyrowski, F., Menten, K. M., & Zhang, Q. 2007, *A&A*, 466, 1065

Beuther, H. & Schilke, P. 2004a, *Science*, 303, 1167

Beuther, H., Schike, P., & Gueth, F. 2004b, *ApJ*, 608, 330

Beuther, H., Schike, P., & Wyrowski, F. 2004c, *ApJ*, 615, 832

Beuther, H., Schike, P., Gueth, F., McCaughrean, M., Andersen, M., Sridharan, T. K., & Menten, K. M. 2002, *A&A*, 387, 931

Beuther, H., Schike, P., & Stanke, T. 2003, *A&A*, 408, 601

Beuther, H & Shepherd, D. S. 2005, in Cores to Clusters: Star Formation With Next Generation Telescopes, eds. M. S. N. Kumar et al., 105-119

Baraffe, I., Chabrier, G., Allard, F., & Hauschildt, P. H. 1998, *A&A*, 337, 403

Calvet, N., Hartmann, L., Kenyon, S. J., & Whitney, B. A. 1994, *ApJ*, 434, 330

Cesaroni, R., Felli, M., Jenness, T., Neri, R., Olmi, L., Robberto, M., Testi, L., & Walmsley, C. M. 1999, *A&A*, 345, 949

Cesaroni, R., Felli, M., Testi, L., Walmsley, C. M., & Olmi, L. 1997, *A&A*, 325, 725

Cesaroni, R., Neri, R., Olmi, L., Testi, L., Walmsley, C. M., & Hofner, P. 2005, *A&A*, 434, 1039

Chen Y., Yao, Y., Yang, J., & Zeng, Q. 2005, *ApJ*, 629, 288

Davis, C. J., Kumar, M. S. N., Sandell, G., Froebrich, D., Smith, M. D., & Currie, M. J. 2007, *MNRAS*, 374, 29

Davis, C. J., Smith, M. D., & Moriarty-Schieven, G. H. 1998, *MNRAS*, 299, 825

De Buizer, J. M. 2007, *ApJ*, 654, L147

Devine, D., Bally, J., Reipurth, B., Shepherd, D., & Watson, A. 1999, *AJ*, 117, 2919

de Wit, W. J., Testi, L., Palla, F., & Zinnecker, H. 2005, *A&A*, 437, 247

Fazio, G. G. et al. 2004, *ApJS*, 154, 10

Flagey, N., Boulanger, F., Verstraete, L., Miville Deschénes, M. A., Grespo, A. N., & Reach, W. T. 2006, *A&A*, 453, 969

Flaherty, K. M., Pipher, J. L., Megeath, S. T., Winston, E. M., Gutermuth, R. A., Muzerolle, J., Allen, L. E., & Fazio, G. G. 2007, *ApJ*, 663, 1069

Fontani, F., Cesanori, R., Testi, L., Molinari, S., Zhang, Q., Brand, J., & Walmsley, C. M. 2004, *A&A*, 424, 179

Fuller, G. A. & Ladd, E. F. 2002, *ApJ*, 573, 699

Gómez, Y., Rodríguez, L. F., Girart, J. M., Garay, G., & Martí, J. 2003, *ApJ*, 597, 414

Greene, T. P., Wilking, B. A., André, P., Young, E. T., & Lada, C. J. 1994, *ApJ*, 434, 614

Gutermuth, R. A., Megeath, S. T., Muzerolle, J. M., Allen, L. E., Pipher, J. L., Myers, P. C., & Fazio, G. G. 2004, *ApJS*, 154, 374

Gutermuth, R. A., Megeath, S. T., Pipher, J. L., Williams, J. P., Allen, L. E., Myers, P. C., & Raines, N. 2005, *ApJ*, 632, 397

Gutermuth, R. A., Myers, P. C., Megeath, S. T., Allen, L. E., Pipher, J. L., Muzerolle, J., Porras, A., Winston, E., & Fazio, G. 2008, *ApJ*, 674, 336

Hartmann, L., Megeath, S. T., Allen, L., Luhman, K., Calvet, N., D'Alessio, P., Franco-Hernandez, R., & Fazio, G. 2005, *ApJ*, 629, 881

Hatchell, J., Fuller, G. A., Richer, J. S., Harries, T. J., & Ladd, E. F. 2007, *A&A*, 468, 1009

Haschick, A. D., Reid, M. J., Burke, B. F., Moran, J. M., & Miller, G. 1981, *ApJ*, 244, 76

Hernández, J., Hartmann, L., Megeath, S. T., Gutermuth, R., Muzerolle, J., Calvet, N., Vivas, A. K., Briceno, C., Allen, L., Stuffer, J., Young, E., & Fazio, G. 2007, *ApJ*, 662, 1067

Hofner, P., Cesaroni, R., Olmi, L., Rodríguez, L. F., Martí, J., & Araya, E. 2007, *A&A*, 465, 197

Hofner, P., Cesaroni, R., Rodríguez, L. F., & Martí, J. 1999, *A&A*, 345, L43

Hora J. L. et al. 2004, *Proc. SPIE*, 5487, 77

Hunter, T. R., Brogan, C. L., Megeath, S. T., Menten, K. M., Beuther, H., & Thorwirth, S. 2006, *ApJ*, 649, 888

Hunter, T. R., Taylor, G. B., Felli, M., & Tofani, G. 1994, *A&A*, 284, 215

Hunter, T. R., Testi, L., Taylor, G. B., Tofani, G., Felli, M., & Phillips, T. G. 1995, *A&A*, 302, 249

Jiang, Z., Yao, Y., Yang, J., Ishii, M., Nagata, T., Nakaya, H., & Sato, S. 2001, *AJ*, 122, 313

Kumar, M. S. N., Bachiller, R., & Davis, C. J. 2002, *ApJ*, 576, 313

Kumar, M. S. N. & Grave, J. M. C. 2007, *A&A*, 472, 155

Kumar, M. S. N., Keto, E., & Clerkin, E. 2006, *A&A*, 449, 1033

Lada, C. J. & Lada, E. A. 2003, *ARA&A*, 41, 57

Lebron, M., Beuther, H., Schike, P., & Stanke, Th. 2006, *A&A*, 448, 1037

Lee, C.-F., Ho, P. T. P., Beuther, H., Bourke, T. L., Zhang, Q., Hirano, N., & Shang, H. 2006, *ApJ*, 639, 292

Longmore, S. N., Burton, M. G., Minier, V., & Walsh, A. J. 2006, *MNRAS*, 369, 1196

Martí, J., Rodgríguez, L. F., & Reipurth, B., 1993, *ApJ*, 416, 208

Martí, J., Rodgríguez, L. F., & Reipurth, B., 1995, *ApJ*, 449, 184

Martí, J., Rodgríguez, L. F., & Reipurth, B., 1998, *ApJ*, 502, 337

Martí, J., Rodgríguez, L. F., & Torrelles, J. M. 1999, *A&A*, 345, L5

Megeath, S. T., Allen, L. E., Gutermuth, R. A., Pipher, J. L., Myers, P. C., Calvet, N., Hartmann, L., Muzerolle, J. & Fazio, G. G. 2004, *ApJS*, 154, 367

Megeath, S. T. & Tieftrunk, A. R. 1999, *ApJ*, 526, L113

Molinari, S., Testi, L., Rodríguez, L. F., & Zhang, Q. 2002, *ApJ*, 570, 758

Moore, T. J. T., Mountain, C. M., & Yamashita, T. 1991, *MNRAS*, 248, 79

Muzerolle, J., Megeath, S. T., Gutermuth, R. A., Allen, L. E., Pipher, J. L., Hartmann, L., Gordon, K. D., Padgett, D. L., Noriega-Crespo, A., Myers, P. C., Fazio, G. G., Rieke, G. H., Young, E. T., Morrison, J. E., Hines, D. C., Su, K. Y. L., Engelbracht, C. W., & Misselt, K. A. 2004, *ApJS*, 154, 379

Nissen, H. D., Gustafsson, M., Lemaire, J. L., Clénet, Y., Rouan, D., & Field, D. 2007, *A&A*, 466, 949

Noriega-Crespo, A., Moro-Martin, A. Garay, S., Morris, P. W., Padgett, D. L., Latter, W. B., & Muzerolle, J. 2004a, *ApJS*, 154, 402

Noriega-Crespo, A., Morris, P., Marleau, F. R., Carey, S., Boogert, A., van Dishoeck, E., Evans II, N. J., Keene, J., Muzerolle, J., Stapelfeldt, K., Pontoppidan, K., Lowrance, P., Allen, L., & Bourke, T. L. 2004b, *ApJS*, 154, 352

Palau, A., Ho, P. T. P., Zhang, Q., Estalella, R., Hirano, N., Shang, H., Lee, C.-F., Bourke, T. L., Beuther, H., & Kuan, Y.-J. 2006, *ApJ*, 636, L137

Palau, A., Estalella, R., Girart, J. M., Ho, P. T. P., Zhang, Q., & Beuther, H. 2007, A&A, 465, 219

Parker, R. J. & Goodwin, S. P. 2007, MNRAS, 380, 1271

Persi, P., Tapia, M., & Smith, H. A. 2006, A&A, 445, 971

Persi, P., Tapia, M., Roth, M., Gómez, M., & Marenzi, A. R. 2005, in Proceedings of IAU Symposium No. 227, Massive Star Birth: A Crossroad of Astrophysics, eds. Cesaroni, R. et al., 291-296

Pipher, J. L. et al. 2004, Proc. SPIE, 5487, 234

Porras, A., Cruz-González, I., & Salas, L. 2000, A&A, 361, 660

Pratap, P., Megeath, S. T., & Bergin, E. A. 1999, ApJ, 517, 799

Raga, A. C., Noriega-Crespo, A., González, R. F., & Velázquez, P. F. 2004, ApJS, 154, 346

Reach, W. T. et al. 2005, PASP, 117, 978

Rieke, G. H. et al. 2004, ApJS, 154, 25

Robitaille, T. P., Whitney, B. A., Indebetouw, R., Wood, K., & Denzmore, P. 2006, ApJS, 167, 256

Rho, J., Reach, W. T., Lefloch, B., & Fazio, G. G. 2006, ApJ, 643, 965

Schultz, A. S. B., Colgan, S. W. J., Erickson, E. F., Kaufman, M. J., Hollenbach, D. J., O'dell C. R., Young, E. T., & Chen, H. 1999, ApJ, 511, 282

Shang, H., Li, Z.-Y., & Hirano, N. 2007, in Protostars and Planets V., eds. B. Reipurth, D. Jewitt, & K. Keil, 261-276

Shepherd, D. S. 2001, ApJ, 546, 345

Shepherd, D. S., Borders, T., Claussen, M., Shirley, Y., & Kurtz, S. 2004a, ApJ, 614, 211

Shepherd, D. S. & Kurtz, S. E. 1999, ApJ, 523, 690

Shepherd, D. S., Kurtz, S. E., & Testi, L. 2004b, ApJ, 601, 952

Shepherd, D. S., Testi, L., & Stark, D. P. 2003, ApJ, 584, 882

Shepherd, D. S., Watson, A. M., Sargent, A. I., & Churchwell, E. 1998, ApJ, 507, 861

Shepherd, D. S., Yu, K. C., Bally, J., & Testi, L. 2000, *ApJ*, 535, 833

Smith, H. A., Hora, J. L., & Marengo, M. 2006, *ApJ*, 645, 1264

Smith, M. D. & Rosen, A. 2005, *MNRAS*, 357, 1370

Sollins, P. K. & Megeath, S. T. 2004, *AJ*, 128, 2374

Sridharan, T. K., Williams, S. J., & Fuller, G. A. 2005, *ApJ*, 631, L73

Stecklum, B., Feldt, M., Richichi, A., Calamai, G., & Lagage, P. O. 1997, *ApJ*, 479, 339

Stern, D., Eisenhardt, P., Gorjian, V. et al. 2005, *ApJ*, 631, 163

Su, Y. N., Liu, S.-Y., Chen, H.-R., Zhang, Q., Cesaroni, R. 2007, *ApJ*, accepted

Testi, L., Palla, F., & Natta, A. 1999, *A&A*, 342, 515

Tobin, J. L., Looney, L. W., Mundy, L. G., Kwon, W., & Hamidouche, M. 2007, *ApJ*, 659, 1404

Torrelles, J. M., Gómez, J. F., Rodríguez, L. F., Ho, P. T. P., Curiel, S., & Vázquez, R. 1997, *ApJ*, 489, 744

Torrelles, J. M., Patel, N. A., Anglada, G., Gómez, J. F., Ho, P. T. P., Lada, L., Alberdi, A., Cantó, J., Curiel, S., Garay, G., & Rodríguez, L. F. 2003, *ApJ*, 598, L115

Valusamy, T., William, D. L., & Marsh, K. A. 2007, *ApJ*, accepted

van den Ancker, M. E., Tielens, A. G. G. M., & Wesselius, P. R. 2000, *A&A*, 358, 1035

Walther, D. M., Aspin, C., & Mclean, I. S. 1990, *ApJ*, 356, 544

Winston, E., Megeath, S. T., Wolk, S. J., Muzerolle, J., Gutermuth, R., Hora, J. L., Allen, L. E., Spitzbart, B., Myers, P., & Fazio, G. G. 2007, *ApJ*, accepted

Werner, M. W., Uchida, K. I., Marengo, M., Gordon, K. D., Morris, P. W., Houck, J. R., & Stansberry, J. A. 2004, *ApJS*, 154, 309

Whitney, B. A., Indebetouw, R., Babler, B. L., Meade, M. R., Watson, C., Wolff, M. G., Clemens, D. P., Bania, T. M., Benjamin, R. A., Cohen, M., Devine, K. E., Dickey, J. M., Heitsch, F., Jackson, J. M., Kobulnicky, H. A., Marston, A. P., Mathis, J. S., Mercer, E. P., Stauffer, J. R., Stolovy, S. R., & Churchwell, E. 2004, *ApJS*, 154, 315

Whitney, B. A., Wood, K., Bjorkman, J. E., & Cohen, M. 2003, *ApJ*, 598, 1079

Yamshita, T., Murata, Y., Kawabe, R., Kaifu, N., & Tamura, M. 1991, ApJ, 373, 560

Yamashita, T., Suzuki, H., Kaifu, N., & Tamura, M. 1989, ApJ, 347, 894

Zhang, Q., Hunter, T. R., Beuther, H., Sridharan, T. K., Liu, S.-Y., Su, Y.-N., Chen, H.-R., & Chen, Y. 2007, 658, 1152

Table 1. Summary of the Sample

Source Name	Reference Center		IRAS Luminosity ( $L_{\odot}$ )	Distance (kpc)	Number of Identified YSOs
	RA(J2000)	DEC(J2000)			
AFGL 5142	05 30 48.00	+33 47 53.8	$10^{3.4}$	1.8	44
IRAS 05358+3543	05 39 12.78	+35 45 50.6	$10^{3.8}$	1.8	30
G192.16-3.82	05 58 13.52	+16 31 58.3	$10^{3.4}$	2.0	31
HH 80-81	18 19 12.09	-20 47 30.9	$10^{4.2}$	1.7	48
IRAS 19410+2336	19 43 11.00	+23 44 35.0	$10^{4.0}$	2.1	46
IRAS 20126+4104	20 14 26.00	+41 13 32.0	$10^{4.0}$	1.7	19
IRAS 20293+3952	20 31 10.70	+40 03 10.0	$10^{3.8}$	2.0	31
W75 N	20 38 36.45	+42 37 34.0	$10^{5.1}$	2.0	77
IRAS 22172+5549	22 19 08.60	+56 05 02.0	$10^{3.3}$	2.4	91

Table 2. Point Source Detections and Limiting Magnitudes

Source Name	3.6 $\mu$ m		4.5 $\mu$ m		5.8 $\mu$ m		8.0 $\mu$ m		24 $\mu$ m	
	number	limiting mag	number	limiting mag						
AFGL 5142	517	18.206 $\pm$ 0.166	545	17.790 $\pm$ 0.168	193	15.849 $\pm$ 0.170	128	15.073 $\pm$ 0.215	16	9.774 $\pm$ 0.131
IRAS 05358+3543	377	17.674 $\pm$ 0.120	410	17.522 $\pm$ 0.185	122	15.168 $\pm$ 0.187	76	13.973 $\pm$ 0.124	12	8.386 $\pm$ 0.148
G192.16-3.82	432	18.365 $\pm$ 0.158	449	17.788 $\pm$ 0.156	130	15.640 $\pm$ 0.199	75	15.271 $\pm$ 0.200	14	9.850 $\pm$ 0.084
HH 80-81	783	16.529 $\pm$ 0.129	862	16.057 $\pm$ 0.193	578	15.066 $\pm$ 0.217	402	13.930 $\pm$ 0.239	17	7.821 $\pm$ 0.184
IRAS 19410+2336	750	16.385 $\pm$ 0.127	844	16.181 $\pm$ 0.119	411	14.807 $\pm$ 0.181	203	13.849 $\pm$ 0.216	21	7.396 $\pm$ 0.067
IRAS 20126+4104	630	17.070 $\pm$ 0.146	808	16.942 $\pm$ 0.155	253	15.894 $\pm$ 0.241	154	14.807 $\pm$ 0.196	7	7.834 $\pm$ 0.174
IRAS 20293+3952	646	16.977 $\pm$ 0.130	769	16.609 $\pm$ 0.159	282	14.953 $\pm$ 0.198	137	13.417 $\pm$ 0.159	11	7.932 $\pm$ 0.133
W75 N	627	17.077 $\pm$ 0.140	798	16.869 $\pm$ 0.194	227	14.371 $\pm$ 0.235	115	12.732 $\pm$ 0.208	11	7.894 $\pm$ 0.144
IRAS 22172+5549	713	17.408 $\pm$ 0.085	869	17.053 $\pm$ 0.107	355	15.975 $\pm$ 0.238	250	15.248 $\pm$ 0.196	19	8.345 $\pm$ 0.093

Table 3. YSOs: 2MASS, IRAC, MIPS 24  $\mu$ m Photometry

RA <sup>†</sup>	DEC <sup>†</sup>	<i>J</i>	<i>H</i>	<i>Ks</i>	[3.6]	[4.5]	[5.8]	[8.0]	[24] <sup>‡</sup>	Remark*
AFGL 5142										
05 30 36.61	+33 49 18.9	—	—	—	14.945 $\pm$ 0.013	14.597 $\pm$ 0.015	14.330 $\pm$ 0.051	13.522 $\pm$ 0.073	—	II
05 30 36.79	+33 47 18.7	—	—	—	14.672 $\pm$ 0.014	14.345 $\pm$ 0.011	13.975 $\pm$ 0.053	13.331 $\pm$ 0.046	—	II
05 30 37.98	+33 49 02.2	—	—	—	11.907 $\pm$ 0.006	11.530 $\pm$ 0.005	11.264 $\pm$ 0.006	10.540 $\pm$ 0.021	7.149 $\pm$ 0.021	II
05 30 40.18	+33 46 18.2	—	—	—	15.257 $\pm$ 0.016	14.343 $\pm$ 0.011	13.485 $\pm$ 0.029	12.623 $\pm$ 0.029	9.156 $\pm$ 0.073	I
05 30 42.14	+33 48 32.8	—	—	—	15.162 $\pm$ 0.035	14.426 $\pm$ 0.036	13.428 $\pm$ 0.060	12.624 $\pm$ 0.061	—	II
05 30 42.36	+33 48 15.1	12.523 $\pm$ 0.023	11.502 $\pm$ 0.022	10.905 $\pm$ 0.019	9.896 $\pm$ 0.002	9.407 $\pm$ 0.002	8.877 $\pm$ 0.002	8.064 $\pm$ 0.002	4.982 $\pm$ 0.035	II
05 30 42.67	+33 48 59.7	—	—	—	14.783 $\pm$ 0.012	14.573 $\pm$ 0.015	14.510 $\pm$ 0.067	14.011 $\pm$ 0.099	—	II
05 30 43.39	+33 46 00.8	—	—	—	13.813 $\pm$ 0.014	13.143 $\pm$ 0.014	12.439 $\pm$ 0.019	11.216 $\pm$ 0.012	7.356 $\pm$ 0.021	I
05 30 45.26	+33 48 26.9	—	—	—	14.450 $\pm$ 0.031	13.467 $\pm$ 0.021	12.687 $\pm$ 0.103	11.950 $\pm$ 0.175	—	I
05 30 46.06	+33 47 54.2	12.467 $\pm$ 0.026	11.303 $\pm$ 0.026	10.350 $\pm$ 0.022	8.462 $\pm$ 0.014	7.806 $\pm$ 0.010	5.900 $\pm$ 0.024	4.010 $\pm$ 0.032	$\ll 0.626$	High <sup>1</sup>
05 30 46.26	+33 47 20.2	—	—	—	13.489 $\pm$ 0.014	12.706 $\pm$ 0.011	12.089 $\pm$ 0.124	10.928 $\pm$ 0.141	—	I
05 30 47.05	+33 47 31.5	14.889 $\pm$ 0.039	13.744 $\pm$ 0.037	13.163 $\pm$ 0.032	11.996 $\pm$ 0.011	11.568 $\pm$ 0.010	11.113 $\pm$ 0.067	10.261 $\pm$ 0.102	—	II
05 30 47.04	+33 48 43.3	—	—	—	14.041 $\pm$ 0.019	13.631 $\pm$ 0.016	13.510 $\pm$ 0.072	12.467 $\pm$ 0.049	—	II
05 30 47.10	+33 45 23.1	—	—	—	15.551 $\pm$ 0.032	15.094 $\pm$ 0.027	14.676 $\pm$ 0.103	14.152 $\pm$ 0.118	—	II
05 30 47.11	+33 50 55.4	12.920 $\pm$ 0.023	12.725 $\pm$ 0.024	12.615 $\pm$ 0.023	12.610 $\pm$ 0.004	12.201 $\pm$ 0.005	12.821 $\pm$ 0.039	12.544 $\pm$ 0.072	—	IRe <sup>36</sup>
05 30 47.53	+33 47 43.3	—	14.903 $\pm$ 0.084	13.580 $\pm$ 0.055	11.908 $\pm$ 0.020	10.881 $\pm$ 0.025	10.359 $\pm$ 0.080	—	—	IRe <sup>36</sup>
05 30 47.74	+33 47 32.9	—	14.544 $\pm$ 0.067	13.481 $\pm$ 0.042	12.402 $\pm$ 0.024	11.900 $\pm$ 0.021	11.405 $\pm$ 0.082	10.974 $\pm$ 0.169	—	II
05 30 47.78	+33 48 13.0	—	—	—	11.712 $\pm$ 0.010	10.483 $\pm$ 0.008	9.731 $\pm$ 0.018	8.841 $\pm$ 0.031	—	I
05 30 47.98	+33 47 54.9	—	—	13.923 $\pm$ 0.079	11.716 $\pm$ 0.041	10.504 $\pm$ 0.056	9.772 $\pm$ 0.089	9.096 $\pm$ 0.104	0.632 $\pm$ 0.005 <sup>▲</sup>	I
05 30 48.04	+33 48 21.4	—	—	14.354 $\pm$ 0.084	12.906 $\pm$ 0.033	12.009 $\pm$ 0.037	11.112 $\pm$ 0.032	9.920 $\pm$ 0.050	4.018 $\pm$ 0.036	I
05 30 47.98	+33 47 10.0	15.174 $\pm$ 0.045	14.210 $\pm$ 0.044	13.702 $\pm$ 0.039	13.059 $\pm$ 0.005	12.827 $\pm$ 0.005	12.496 $\pm$ 0.029	11.731 $\pm$ 0.033	—	II
05 30 48.31	+33 47 34.6	—	—	—	14.149 $\pm$ 0.040	13.612 $\pm$ 0.050	12.972 $\pm$ 0.157	11.634 $\pm$ 0.166	—	I
05 30 48.33	+33 48 04.6	—	—	—	13.683 $\pm$ 0.111	12.278 $\pm$ 0.071	11.535 $\pm$ 0.105	10.707 $\pm$ 0.134	—	I
05 30 48.41	+33 47 23.8	—	—	—	14.799 $\pm$ 0.045	14.283 $\pm$ 0.044	13.709 $\pm$ 0.137	13.131 $\pm$ 0.239	—	II
05 30 48.85	+33 50 21.7	—	—	14.769 $\pm$ 0.100	13.923 $\pm$ 0.009	13.229 $\pm$ 0.006	12.869 $\pm$ 0.015	12.137 $\pm$ 0.034	9.139 $\pm$ 0.101	II
05 30 49.08	+33 47 45.7	—	—	—	12.087 $\pm$ 0.008	10.958 $\pm$ 0.010	10.315 $\pm$ 0.015	9.883 $\pm$ 0.032	—	I
05 30 49.19	+33 48 18.8	—	—	—	13.976 $\pm$ 0.026	13.054 $\pm$ 0.027	12.327 $\pm$ 0.060	11.419 $\pm$ 0.075	—	I
05 30 49.21	+33 47 38.5	—	15.284 $\pm$ 0.090	—	14.097 $\pm$ 0.036	13.716 $\pm$ 0.052	13.283 $\pm$ 0.149	12.758 $\pm$ 0.233	—	II
05 30 49.69	+33 46 24.7	—	—	—	14.108 $\pm$ 0.014	13.335 $\pm$ 0.010	12.595 $\pm$ 0.014	11.631 $\pm$ 0.013	7.681 $\pm$ 0.049	I
05 30 49.78	+33 47 36.9	—	—	—	14.808 $\pm$ 0.030	14.606 $\pm$ 0.042	14.454 $\pm$ 0.213	13.355 $\pm$ 0.137	—	II
05 30 49.82	+33 48 17.2	—	—	—	14.376 $\pm$ 0.032	12.950 $\pm$ 0.017	12.059 $\pm$ 0.027	10.956 $\pm$ 0.033	—	I
05 30 50.26	+33 47 03.0	—	—	—	14.636 $\pm$ 0.017	14.289 $\pm$ 0.015	13.808 $\pm$ 0.037	12.993 $\pm$ 0.038	—	II
05 30 50.51	+33 48 05.3	—	—	—	15.281 $\pm$ 0.032	13.538 $\pm$ 0.016	12.463 $\pm$ 0.034	11.220 $\pm$ 0.032	4.631 $\pm$ 0.052	I
05 30 51.09	+33 50 11.1	—	—	—	14.429 $\pm$ 0.012	13.876 $\pm$ 0.009	13.337 $\pm$ 0.027	12.524 $\pm$ 0.045	9.775 $\pm$ 0.131	II

Table 3—Continued

RA <sup>†</sup>	DEC <sup>†</sup>	<i>J</i>	<i>H</i>	<i>Ks</i>	[3.6]	[4.5]	[5.8]	[8.0]	[24] <sup>‡</sup>	Remark*
05 30 51.31	+33 48 04.7	—	15.279±0.087	14.735±0.090	14.023±0.010	13.643±0.010	13.313±0.042	12.468±0.044	—	II
05 30 51.41	+33 46 48.3	—	—	—	14.821±0.040	14.241±0.023	14.093±0.108	13.648±0.105	—	II
05 30 51.64	+33 48 42.7	—	—	—	14.825±0.017	14.403±0.014	14.020±0.042	13.212±0.070	—	II
05 30 51.74	+33 47 39.5	—	—	14.750±0.099	13.849±0.009	13.484±0.008	13.198±0.039	12.595±0.054	—	II
05 30 52.68	+33 47 59.5	—	—	—	13.904±0.009	13.477±0.007	13.341±0.050	12.776±0.051	—	II
05 30 53.23	+33 45 39.5	15.137±0.045	14.229±0.041	13.871±0.047	13.090±0.004	12.664±0.004	12.172±0.012	11.195±0.009	8.366±0.023	II
05 30 54.65	+33 47 30.8	15.639±0.060	14.561±0.050	13.749±0.040	11.958±0.002	11.329±0.003	10.797±0.004	10.139±0.003	7.343±0.037	II
05 30 54.92	+33 47 18.0	—	—	—	14.982±0.013	14.661±0.017	14.177±0.039	13.415±0.048	—	II
05 30 55.27	+33 46 53.4	—	—	—	14.625±0.009	14.244±0.010	13.835±0.050	13.053±0.043	—	II
05 30 57.18	+33 46 39.9	—	—	—	14.814±0.018	14.368±0.013	13.754±0.042	12.824±0.038	9.233±0.080	II
IRAS 05358+3543										
05 39 05.66	+35 47 03.0	—	—	13.869±0.048	11.536±0.004	10.554±0.003	9.983±0.003	9.357±0.012	6.341±0.033	II
05 39 07.22	+35 43 40.0	15.176±0.038	13.801±0.028	12.834±0.027	11.661±0.003	11.215±0.003	10.729±0.006	9.930±0.005	7.071±0.055	II
05 39 07.80	+35 43 59.1	14.911±0.044	13.835±0.041	13.255±0.039	12.760±0.007	12.548±0.008	12.345±0.037	11.978±0.041	7.003±0.104	II
05 39 08.11	+35 45 58.5	—	—	—	15.843±0.066	14.475±0.037	13.077±0.107	11.876±0.076	—	I
05 39 08.50	+35 46 37.7	—	—	—	15.321±0.041	12.477±0.010	10.898±0.012	9.760±0.020	3.409±0.008	I
05 39 08.91	+35 45 06.3	15.119±0.060	13.492±0.047	12.588±0.041	11.737±0.111	11.334±0.103	—	—	—	IRe
05 39 09.17	+35 45 03.2	15.477±0.063	14.259±0.064	13.566±0.061	12.057±0.167	11.545±0.154	—	—	—	IRe
05 39 09.17	+35 44 22.6	11.474±0.022	10.532±0.016	9.697±0.018	8.406±0.001	7.987±0.002	7.217±0.001	5.918±0.001	2.009±0.001	II
05 39 09.40	+35 46 08.2	—	—	—	15.603±0.145	13.431±0.059	13.382±0.165	12.814±0.165	—	I
05 39 09.54	+35 45 05.8	14.436±0.043	12.767±0.031	11.868±0.027	10.920±0.099	10.540±0.074	—	—	—	IRe
05 39 09.92	+35 45 17.2	12.371±0.026	10.631±0.021	9.251±0.019	6.973±0.007	6.236±0.004	5.386±0.019	4.325±0.051	≪ 0.626	High <sup>2</sup>
05 39 09.99	+35 46 27.1	—	—	—	15.851±0.051	13.459±0.019	12.387±0.043	11.472±0.026	—	I
05 39 10.15	+35 44 28.2	15.982±0.065	14.839±0.050	14.237±0.060	13.512±0.021	13.029±0.030	—	11.841±0.213	—	IRe
05 39 10.41	+35 45 03.5	13.699±0.027	12.346±0.019	11.598±0.020	10.882±0.020	10.233±0.012	9.104±0.080	7.760±0.096	—	I
05 39 11.27	+35 45 22.6	15.572±0.057	13.851±0.034	13.028±0.029	12.063±0.018	11.684±0.038	10.747±0.048	9.660±0.043	—	II
05 39 11.50	+35 43 33.7	—	—	—	13.904±0.010	13.367±0.009	12.735±0.025	12.267±0.049	—	II
05 39 11.58	+35 45 09.2	15.896±0.066	14.724±0.046	14.417±0.069	13.795±0.033	13.187±0.033	12.043±0.231	—	—	IRe
05 39 11.58	+35 46 22.2	—	15.470±0.093	13.834±0.044	12.326±0.006	11.664±0.009	11.230±0.027	10.656±0.067	—	II
05 39 11.75	+35 43 43.5	15.938±0.076	14.780±0.066	14.241±0.065	13.678±0.006	13.387±0.013	12.917±0.033	12.250±0.055	—	II
05 39 11.80	+35 44 24.9	—	—	—	16.143±0.079	14.693±0.047	13.896±0.115	13.323±0.235	—	I
05 39 12.13	+35 43 39.7	—	15.537±0.099	—	14.554±0.018	14.262±0.021	13.890±0.053	13.223±0.063	—	II
05 39 13.35	+35 44 17.0	14.108±0.034	13.012±0.027	12.537±0.025	11.532±0.002	11.154±0.003	10.727±0.007	10.228±0.012	6.328±0.099	II

Table 3—Continued

RA <sup>†</sup>	DEC <sup>†</sup>	<i>J</i>	<i>H</i>	<i>Ks</i>	[3.6]	[4.5]	[5.8]	[8.0]	[24] <sup>‡</sup>	Remark*
05 39 13.81	+35 45 35.5	—	—	—	13.524±0.058	12.413±0.064	11.913±0.124	11.229±0.091	—	I
05 39 14.66	+35 45 23.9	15.821±0.065	14.183±0.039	13.275±0.034	12.317±0.005	11.839±0.006	11.378±0.016	10.683±0.036	—	II
05 39 14.75	+35 45 39.6	—	—	13.814±0.040	12.025±0.024	11.161±0.024	10.602±0.034	9.924±0.035	—	I
05 39 14.79	+35 46 01.9	—	15.298±0.095	13.566±0.060	12.521±0.061	11.838±0.060	11.462±0.070	10.995±0.067	—	II
05 39 18.15	+35 46 08.6	12.327±0.022	11.586±0.018	11.223±0.019	11.014±0.004	10.923±0.004	10.813±0.029	10.432±0.101	5.735±0.110	II
05 39 21.03	+35 46 09.3	—	—	—	14.865±0.020	14.378±0.022	13.773±0.133	12.543±0.194	—	I
05 39 22.95	+35 44 49.6	15.792±0.059	14.551±0.042	14.025±0.049	13.303±0.006	12.945±0.005	12.558±0.033	11.792±0.056	8.386±0.148	II
05 39 24.79	+35 44 45.4	—	—	—	14.218±0.022	13.261±0.008	12.248±0.047	11.214±0.080	7.141±0.056	I
G192.16-3.82										
05 58 05.44	+16 34 17.8	15.827±0.061	15.049±0.054	—	14.080±0.009	13.863±0.015	13.758±0.079	13.245±0.117	—	II
05 58 09.98	+16 34 50.7	15.855±0.064	14.858±0.058	14.589±0.092	14.071±0.012	13.854±0.018	13.574±0.061	12.402±0.055	—	I/II
05 58 10.21	+16 34 34.5	16.193±0.088	15.333±0.084	14.758±0.087	14.353±0.012	14.053±0.013	13.906±0.094	12.693±0.154	7.897±0.067	II
05 58 10.37	+16 33 57.4	15.085±0.038	14.227±0.039	13.988±0.050	13.256±0.013	13.066±0.009	12.920±0.152	—	7.163±0.089	II
05 58 11.15	+16 31 20.0	14.373±0.029	13.392±0.027	12.821±0.028	12.331±0.013	12.129±0.013	10.477±0.050	8.737±0.074	—	I/II
05 58 11.91	+16 32 54.3	15.811±0.074	14.114±0.040	13.272±0.039	12.226±0.027	11.886±0.009	10.913±0.130	9.527±0.177	—	I/II
05 58 12.16	+16 31 25.1	14.834±0.034	13.653±0.021	13.293±0.030	12.647±0.007	12.329±0.006	11.848±0.042	10.987±0.099	—	II
05 58 13.84	+16 31 57.1	15.898±0.075	13.322±0.051	11.130±0.056	8.983±0.015	8.104±0.018	7.748±0.026	—	—	IRe
05 58 13.93	+16 30 00.0	13.328±0.022	12.765±0.019	12.377±0.019	12.050±0.004	11.827±0.004	10.773±0.006	9.324±0.004	7.346±0.021	II
05 58 13.95	+16 31 31.0	—	—	—	13.234±0.029	11.950±0.016	11.085±0.037	10.064±0.040	—	I
05 58 13.99	+16 30 18.8	—	—	—	13.349±0.015	12.752±0.010	12.207±0.032	11.691±0.036	—	II
05 58 14.21	+16 30 46.1	16.106±0.069	14.993±0.051	14.404±0.059	13.571±0.032	13.210±0.038	12.621±0.220	12.677±0.144	—	IRe
05 58 14.64	+16 31 54.7	—	15.291±0.077	13.063±0.034	10.578±0.013	9.645±0.009	8.854±0.005	8.010±0.027	—	I
05 58 14.74	+16 31 07.0	13.103±0.028	10.752±0.023	9.041±0.021	6.982±0.002	6.140±0.002	5.304±0.001	4.456±0.000	1.287±0.002	I
05 58 14.96	+16 30 22.9	11.460±0.021	10.546±0.018	10.261±0.019	9.851±0.003	9.663±0.003	9.211±0.006	8.766±0.008	5.967±0.033	II
05 58 15.23	+16 31 13.6	14.645±0.037	13.519±0.033	13.087±0.046	12.189±0.025	11.645±0.061	—	—	—	IRe
05 58 15.26	+16 31 39.2	15.412±0.055	14.248±0.038	13.615±0.039	12.305±0.084	12.094±0.084	—	—	—	IRe
05 58 15.44	+16 31 02.6	—	14.880±0.080	13.203±0.077	11.610±0.057	10.966±0.079	10.335±0.055	9.422±0.095	—	II
05 58 15.47	+16 33 57.7	—	15.405±0.066	14.722±0.085	13.706±0.036	13.274±0.033	12.378±0.188	10.854±0.235	—	I
05 58 15.60	+16 30 58.3	—	14.389±0.055	13.472±0.051	11.946±0.024	11.384±0.027	11.178±0.170	10.285±0.127	—	II
05 58 15.68	+16 32 30.0	15.508±0.047	13.803±0.030	12.686±0.023	11.464±0.009	10.930±0.005	10.521±0.090	9.571±0.224	—	II
05 58 15.78	+16 30 26.3	—	15.140±0.063	13.763±0.039	12.480±0.008	11.932±0.008	11.411±0.017	10.671±0.034	7.599±0.194	II
05 58 16.02	+16 31 01.2	16.328±0.085	14.459±0.040	13.353±0.032	11.942±0.011	11.406±0.017	10.986±0.081	10.508±0.108	—	II
05 58 16.38	+16 30 41.9	14.798±0.030	13.327±0.027	12.488±0.021	11.328±0.003	10.985±0.003	10.700±0.007	10.220±0.014	—	II

Table 3—Continued

RA <sup>†</sup>	DEC <sup>†</sup>	<i>J</i>	<i>H</i>	<i>Ks</i>	[3.6]	[4.5]	[5.8]	[8.0]	[24] <sup>‡</sup>	Remark*
05 58 16.49	+16 31 32.4	—	15.608±0.081	14.990±0.100	13.752±0.093	13.821±0.074	—	—	—	IRe
05 58 16.58	+16 30 29.7	—	—	—	13.091±0.007	12.501±0.006	12.071±0.017	11.477±0.034	7.919±0.051*	II
05 58 17.46	+16 30 15.4	14.983±0.039	13.827±0.033	13.347±0.034	12.814±0.005	12.544±0.005	12.147±0.014	11.372±0.022	8.214±0.026	II
05 58 17.53	+16 31 19.0	15.126±0.037	14.087±0.027	13.492±0.034	12.484±0.006	12.074±0.005	11.758±0.039	11.114±0.115	—	II
05 58 18.16	+16 34 39.9	16.572±0.097	15.699±0.087	—	14.671±0.018	14.238±0.013	13.856±0.106	12.750±0.210	—	I
05 58 21.27	+16 29 34.2	—	—	—	14.453±0.010	14.021±0.010	13.618±0.038	12.900±0.037	—	II
05 58 22.19	+16 33 12.1	—	—	—	16.903±0.065	16.627±0.075	—	—	7.927±0.041	II
HH 80-81										
18 18 59.59	-20 45 53.8	14.750±0.029	14.214±0.049	13.843±0.051	13.526±0.029	13.341±0.029	13.346±0.094	—	—	IRe
18 19 01.08	-20 45 47.7	—	—	—	14.154±0.048	13.571±0.046	13.226±0.051	12.630±0.090	—	II
18 19 02.02	-20 47 17.2	—	—	—	13.566±0.037	13.268±0.032	12.959±0.104	11.708±0.057	7.770±0.113	II
18 19 03.13	-20 47 00.9	15.435±0.089	—	—	12.508±0.018	12.156±0.013	11.710±0.031	10.861±0.078	—	II
18 19 03.81	-20 45 06.3	14.848±0.055	13.556±0.036	12.908±0.035	11.856±0.010	11.330±0.007	10.810±0.008	9.668±0.012	6.391±0.020	II
18 19 04.51	-20 45 26.8	—	—	—	14.027±0.056	13.717±0.044	13.556±0.084	12.538±0.133	—	II
18 19 05.77	-20 49 20.0	—	—	13.454±0.049	12.130±0.025	11.644±0.020	10.928±0.015	9.917±0.036	6.020±0.023	II
18 19 06.24	-20 49 19.3	14.851±0.038	13.755±0.047	13.107±0.037	12.160±0.012	11.791±0.011	11.382±0.018	10.570±0.031	—	I
18 19 07.77	-20 48 45.5	—	—	—	13.097±0.054	12.757±0.045	12.471±0.046	11.924±0.061	—	II
18 19 08.97	-20 47 36.0	15.070±0.030	14.285±0.021	13.954±0.050	13.324±0.061	13.108±0.066	—	—	—	IRe
18 19 09.11	-20 47 15.0	15.672±0.051	14.306±0.021	13.804±0.051	—	12.264±0.132	—	—	—	IRe
18 19 09.84	-20 47 15.6	15.719±0.070	13.538±0.021	12.077±0.020	10.275±0.039	9.748±0.026	—	—	—	IRe
18 19 09.98	-20 44 49.5	—	—	13.861±0.093	13.090±0.045	12.686±0.031	12.452±0.065	11.844±0.076	—	II
18 19 10.51	-20 46 57.8	11.209±0.030	10.496±0.029	10.022±0.029	9.737±0.053	9.479±0.066	—	—	« 0.626	High <sup>3</sup>
18 19 10.76	-20 46 41.4	—	14.780±0.060	12.527±0.031	9.911±0.025	9.119±0.015	8.612±0.101	—	—	IRe
18 19 11.00	-20 46 38.5	—	14.098±0.025	12.988±0.023	11.499±0.088	10.845±0.054	—	—	—	IRe
18 19 11.47	-20 48 47.8	—	—	—	13.621±0.044	12.345±0.016	11.687±0.110	11.018±0.091	—	I
18 19 12.08	-20 47 50.9	13.062±0.044	10.244±0.038	8.186±0.026	6.077±0.004	5.432±0.004	4.700±0.012	3.650±0.034	« 0.626	High <sup>4</sup>
18 19 12.26	-20 44 53.3	15.947±0.094	14.521±0.048	13.724±0.044	12.785±0.046	12.397±0.041	12.301±0.083	11.775±0.067	—	II
18 19 12.95	-20 48 45.6	—	—	14.200±0.063	12.377±0.011	11.587±0.005	11.156±0.047	10.438±0.014	—	II
18 19 13.43	-20 46 25.3	15.882±0.072	14.986±0.077	—	13.627±0.067	13.281±0.115	—	—	—	IRe
18 19 13.64	-20 47 50.5	14.782±0.037	13.090±0.022	12.055±0.019	10.849±0.019	10.371±0.027	9.693±0.081	8.324±0.117	—	I
18 19 13.79	-20 47 40.5	—	—	—	11.842±0.057	10.227±0.013	9.317±0.039	8.575±0.106	—	I
18 19 14.02	-20 45 09.7	—	15.161±0.071	14.282±0.069	13.311±0.027	13.064±0.024	12.790±0.096	11.826±0.134	—	II
18 19 14.19	-20 47 59.8	15.435±0.053	13.872±0.022	13.144±0.019	11.893±0.039	11.460±0.032	10.303±0.200	8.786±0.203	—	I

Table 3—Continued

RA <sup>†</sup>	DEC <sup>†</sup>	<i>J</i>	<i>H</i>	<i>Ks</i>	[3.6]	[4.5]	[5.8]	[8.0]	[24] <sup>‡</sup>	Remark*
18 19 14.53	-20 48 28.4	—	—	—	13.298±0.020	13.001±0.024	12.464±0.175	11.527±0.238	—	II
18 19 14.64	-20 46 59.2	13.009±0.026	12.342±0.025	11.869±0.037	11.482±0.084	11.228±0.111	9.664±0.062	7.576±0.044	—	I/II
18 19 14.68	-20 49 29.1	—	—	—	14.441±0.080	14.079±0.060	13.675±0.105	12.680±0.067	—	II
18 19 14.79	-20 45 58.7	—	14.239±0.066	12.551±0.034	11.536±0.010	11.307±0.011	11.031±0.053	10.291±0.168	—	II
18 19 14.83	-20 47 14.5	—	—	—	12.529±0.057	11.803±0.047	11.413±0.088	10.725±0.146	—	II
18 19 15.10	-20 47 46.0	11.553±0.039	10.734±0.047	10.051±0.035	8.324±0.026	7.845±0.019	5.617±0.048	3.802±0.062	≤ 0.626	High <sup>5</sup>
18 19 15.88	-20 46 05.7	—	—	—	13.244±0.026	12.690±0.029	12.062±0.089	10.893±0.054	—	I
18 19 16.16	-20 48 17.2	—	—	—	13.911±0.026	13.234±0.028	12.412±0.180	11.182±0.192	—	I
18 19 17.95	-20 45 10.4	13.699±0.028	13.325±0.038	13.146±0.044	12.624±0.014	12.541±0.019	—	—	—	IRe
18 19 20.89	-20 46 32.5	—	—	—	13.754±0.069	13.282±0.061	12.831±0.098	12.039±0.091	—	II
18 19 20.95	-20 46 09.6	13.080±0.029	11.920±0.031	11.079±0.026	9.930±0.005	9.330±0.005	8.827±0.004	8.014±0.006	4.206±0.005	II
18 19 21.10	-20 45 55.9	14.053±0.077	12.423±0.085	10.902±0.037	9.173±0.007	8.231±0.005	7.604±0.004	6.879±0.017	2.663±0.004	I
18 19 21.16	-20 47 41.8	—	—	—	13.718±0.022	12.925±0.015	12.476±0.030	12.014±0.076	—	II
18 19 21.37	-20 45 30.5	—	—	14.062±0.072	12.593±0.027	11.884±0.021	11.316±0.030	10.694±0.067	—	II
18 19 21.52	-20 45 56.6	14.107±0.057	12.352±0.052	11.007±0.039	9.283±0.006	8.511±0.006	7.884±0.003	6.961±0.002	—	II
18 19 21.78	-20 45 35.9	14.690±0.079	12.817±0.065	11.918±0.034	11.135±0.015	10.713±0.013	10.168±0.016	9.066±0.026	4.723±0.008	II
18 19 22.00	-20 48 51.5	14.530±0.044	12.569±0.029	11.152±0.023	9.587±0.003	8.959±0.003	8.410±0.002	7.636±0.002	4.640±0.006	II
18 19 22.08	-20 45 36.9	12.827±0.039	11.200±0.038	10.272±0.030	9.544±0.004	9.173±0.004	8.952±0.004	8.473±0.011	—	II
18 19 22.77	-20 46 45.2	14.968±0.046	14.039±0.053	13.502±0.034	12.579±0.006	12.185±0.004	11.780±0.016	11.016±0.043	—	II
18 19 22.86	-20 44 41.2	—	13.899±0.052	12.047±0.024	10.931±0.005	10.044±0.003	9.606±0.006	8.854±0.013	—	I
18 19 23.35	-20 47 54.1	—	—	—	14.643±0.037	14.274±0.030	13.988±0.082	13.492±0.211	—	II
18 19 23.53	-20 48 18.3	—	—	—	14.308±0.029	13.833±0.030	13.410±0.073	12.952±0.098	—	II
18 19 23.59	-20 45 43.0	—	—	14.161±0.059	12.401±0.011	11.709±0.010	11.180±0.014	10.213±0.012	—	II
IRAS 19410+2336										
19 42 56.93	+23 46 32.0	—	—	—	13.594±0.015	13.366±0.019	13.186±0.076	12.474±0.136	—	II
19 42 57.66	+23 44 49.3	15.520±0.074	14.756±0.078	14.076±0.062	13.660±0.030	13.563±0.044	—	—	—	IRe
19 43 02.75	+23 43 18.3	—	—	12.975±0.031	9.023±0.002	7.945±0.002	7.033±0.001	6.436±0.002	4.725±0.014	II
19 43 03.34	+23 45 09.4	—	13.997±0.061	—	12.760±0.010	12.651±0.016	12.614±0.061	11.935±0.122	6.491±0.012	II
19 43 03.60	+23 46 50.6	15.194±0.050	14.808±0.083	—	13.557±0.017	13.146±0.012	—	—	—	IRe
19 43 04.53	+23 42 32.8	14.914±0.037	14.250±0.058	13.849±0.048	13.317±0.024	13.187±0.023	—	—	—	IRe
19 43 05.75	+23 41 35.0	—	—	—	14.247±0.056	13.879±0.051	13.555±0.120	12.536±0.171	—	II
19 43 06.25	+23 42 44.2	—	14.837±0.082	13.891±0.059	12.872±0.007	12.422±0.008	12.110±0.032	11.851±0.068	—	IRe
19 43 06.91	+23 43 58.0	11.881±0.024	11.226±0.035	10.639±0.032	10.071±0.078	9.306±0.042	—	—	-0.4±0.1**	High <sup>6</sup>

Table 3—Continued

RA <sup>†</sup>	DEC <sup>†</sup>	<i>J</i>	<i>H</i>	<i>Ks</i>	[3.6]	[4.5]	[5.8]	[8.0]	[24] <sup>‡</sup>	Remark*
19 43 08.18	+23 43 41.4	—	—	13.717±0.046	10.600±0.009	9.516±0.005	8.593±0.018	7.855±0.045	—	I
19 43 08.60	+23 44 25.6	—	15.187±0.099	14.329±0.080	12.561±0.040	11.617±0.031	10.796±0.057	—	—	IRe
19 43 09.04	+23 44 08.9	—	—	12.164±0.043	10.247±0.010	9.069±0.004	7.811±0.011	5.720±0.016	1.981±0.027	I
19 43 09.18	+23 44 13.9	14.080±0.052	13.447±0.037	12.968±0.036	12.060±0.050	11.675±0.067	—	—	—	IRe
19 43 09.41	+23 47 05.9	14.507±0.040	13.557±0.045	12.901±0.039	12.034±0.008	11.750±0.007	11.502±0.018	10.545±0.025	7.133±0.018	II
19 43 09.43	+23 46 12.7	15.339±0.059	14.226±0.083	—	12.554±0.011	12.448±0.008	12.313±0.096	—	—	IRe
19 43 09.45	+23 44 34.0	13.407±0.031	12.409±0.039	11.690±0.033	10.243±0.051	9.956±0.041	7.387±0.096	5.765±0.112	1.420±0.008	II
19 43 09.78	+23 45 07.4	—	—	13.685±0.056	11.878±0.014	11.072±0.015	10.552±0.032	10.109±0.062	—	I
19 43 10.61	+23 44 57.6	—	14.202±0.056	12.527±0.033	11.000±0.009	10.024±0.011	9.207±0.021	8.487±0.041	1.724±0.003	I
19 43 10.77	+23 45 07.8	—	—	—	13.394±0.131	11.730±0.071	11.121±0.101	10.635±0.112	—	I
19 43 11.45	+23 44 50.6	—	—	—	14.025±0.065	12.963±0.058	12.033±0.106	10.991±0.130	—	I
19 43 11.53	+23 43 37.6	—	13.797±0.075	12.405±0.043	10.739±0.008	9.986±0.010	9.114±0.037	8.488±0.055	—	II
19 43 11.59	+23 47 28.6	13.822±0.027	13.267±0.030	13.111±0.033	13.013±0.009	12.806±0.008	13.010±0.041	12.438±0.086	—	II
19 43 11.60	+23 44 58.8	—	—	13.426±0.044	12.128±0.017	11.503±0.021	10.859±0.051	10.155±0.082	—	II
19 43 11.85	+23 43 53.5	15.002±0.056	12.998±0.041	11.514±0.028	9.812±0.010	9.090±0.029	8.727±0.074	8.066±0.040	—	II
19 43 11.91	+23 44 52.3	—	—	—	13.414±0.033	12.821±0.036	12.378±0.131	11.539±0.049	—	II
19 43 12.41	+23 45 25.5	—	—	—	13.823±0.043	12.941±0.023	12.517±0.133	11.276±0.122	—	I
19 43 12.85	+23 45 18.6	—	—	14.169±0.090	12.203±0.007	11.578±0.005	10.993±0.019	10.305±0.052	—	II
19 43 12.95	+23 45 01.7	—	14.738±0.068	13.915±0.056	12.906±0.008	12.550±0.008	12.587±0.081	—	—	IRe
19 43 13.33	+23 46 04.7	14.690±0.041	14.041±0.066	—	—	12.713±0.014	—	—	—	IRe
19 43 14.22	+23 45 26.9	—	—	—	11.550±0.004	10.402±0.003	9.436±0.008	8.733±0.023	—	I
19 43 14.72	+23 44 26.1	—	13.311±0.050	10.225±0.026	7.883±0.005	7.621±0.005	7.205±0.002	6.713±0.006	—	II
19 43 14.95	+23 45 33.9	15.816±0.078	14.002±0.052	13.023±0.036	11.542±0.006	10.875±0.005	10.310±0.010	9.541±0.027	5.851±0.024*	I
19 43 15.09	+23 44 38.4	—	—	13.382±0.036	12.309±0.023	12.076±0.039	11.817±0.094	11.385±0.250	—	II
19 43 15.29	+23 45 26.7	—	—	—	13.580±0.018	12.373±0.015	11.539±0.043	10.849±0.093	5.196±0.029	I
19 43 15.61	+23 43 56.1	—	14.866±0.087	14.049±0.068	12.754±0.091	12.460±0.143	—	—	—	IRe
19 43 16.01	+23 42 58.2	15.191±0.067	14.154±0.063	13.586±0.057	13.095±0.017	12.785±0.015	—	—	—	IRe
19 43 16.43	+23 44 21.2	15.342±0.057	14.459±0.060	14.249±0.073	13.221±0.112	13.297±0.128	—	—	—	IRe
19 43 16.73	+23 45 18.2	15.294±0.070	13.604±0.053	12.441±0.036	11.010±0.006	10.451±0.004	9.962±0.013	9.345±0.048	7.100±0.117	II
19 43 16.87	+23 45 08.9	—	—	14.192±0.095	12.996±0.015	12.600±0.021	12.442±0.043	11.779±0.066	—	II
19 43 16.90	+23 45 13.1	—	—	—	12.373±0.022	11.586±0.011	10.812±0.023	10.125±0.060	—	II
19 43 21.22	+23 46 25.0	15.669±0.071	14.541±0.061	14.000±0.059	13.052±0.012	12.706±0.010	12.590±0.050	12.252±0.105	—	IRe
19 43 21.59	+23 44 33.2	—	—	14.343±0.078	13.072±0.040	12.692±0.025	12.223±0.162	—	7.026±0.096	II
19 43 22.08	+23 46 06.6	—	—	14.456±0.083	13.815±0.027	13.542±0.029	13.500±0.120	13.055±0.209	—	II
19 43 22.12	+23 45 09.1	—	—	—	13.369±0.034	12.687±0.014	12.072±0.073	11.041±0.166	—	II

Table 3—Continued

RA <sup>†</sup>	DEC <sup>†</sup>	<i>J</i>	<i>H</i>	<i>Ks</i>	[3.6]	[4.5]	[5.8]	[8.0]	[24] <sup>‡</sup>	Remark*
19 43 22.10	+23 46 38.8	16.021±0.095	15.008±0.089	14.354±0.080	13.800±0.019	13.599±0.021	—	—	—	IRe
19 43 25.12	+23 43 02.0	—	14.327±0.062	13.377±0.049	12.413±0.014	11.791±0.007	11.259±0.029	10.668±0.033	—	II
IRAS 20126+4104										
20 14 18.59	+41 14 33.7	11.931±0.025	11.622±0.030	—	10.937±0.010	10.811±0.008	10.676±0.076	—	—	IRe
20 14 19.05	+41 13 36.3	9.419±0.020	9.323±0.017	9.251±0.020	9.328±0.002	9.303±0.002	9.257±0.006	9.140±0.039	4.594±0.046	II
20 14 20.46	+41 13 41.3	15.873±0.093	15.057±0.085	—	13.863±0.026	13.532±0.024	13.341±0.113	—	—	IRe
20 14 23.21	+41 13 25.1	—	—	13.675±0.062	11.893±0.007	11.286±0.014	10.733±0.037	10.022±0.080	—	II
20 14 24.51	+41 11 22.1	15.053±0.046	14.515±0.052	14.150±0.086	13.516±0.026	13.539±0.025	—	—	—	IRe
20 14 24.99	+41 13 32.0	12.064±0.021	11.683±0.019	11.485±0.031	10.685±0.038	10.348±0.083	8.125±0.037	6.367±0.060	—	I/II
20 14 26.57	+41 15 29.7	—	—	—	14.428±0.027	13.754±0.018	13.213±0.093	12.134±0.170	—	II
20 14 27.12	+41 14 44.0	15.200±0.053	14.167±0.042	14.018±0.079	13.044±0.054	12.902±0.044	—	—	—	IRe
20 14 28.18	+41 13 17.0	15.847±0.086	14.635±0.064	14.185±0.087	—	12.674±0.143	—	—	—	IRe
20 14 28.38	+41 13 51.7	12.669±0.021	11.557±0.019	10.815±0.023	9.905±0.005	9.593±0.004	9.250±0.032	8.660±0.094	—	II
20 14 33.58	+41 12 30.6	14.044±0.037	12.990±0.037	—	11.861±0.006	11.423±0.005	10.967±0.008	10.222±0.012	—	II
20 14 34.67	+41 10 59.6	—	14.981±0.085	14.245±0.083	13.766±0.013	12.829±0.011	12.411±0.025	11.767±0.037	—	I
20 14 34.91	+41 12 31.3	15.375±0.044	14.223±0.036	13.442±0.046	12.682±0.005	12.233±0.004	11.980±0.011	11.254±0.028	7.372±0.173	II
20 14 37.57	+41 12 34.8	15.698±0.067	14.661±0.055	14.090±0.075	12.956±0.005	12.326±0.004	11.791±0.009	10.771±0.026	7.834±0.174	II
20 14 38.69	+41 12 23.2	—	15.165±0.090	—	14.194±0.015	13.982±0.015	13.697±0.038	12.876±0.114	—	II
20 14 39.92	+41 14 35.4	15.361±0.080	14.216±0.067	13.634±0.058	13.056±0.012	12.674±0.008	12.247±0.021	11.049±0.028	—	I/II
20 14 41.17	+41 12 55.8	15.290±0.052	14.028±0.041	13.281±0.045	12.422±0.005	11.989±0.005	11.770±0.009	11.421±0.036	—	IRe
20 14 43.33	+41 13 40.7	13.937±0.028	12.997±0.023	12.575±0.027	12.164±0.004	11.934±0.004	11.715±0.014	10.711±0.037	—	II
20 14 44.47	+41 12 59.8	15.492±0.072	14.398±0.061	13.814±0.066	13.132±0.008	12.682±0.009	12.336±0.024	11.223±0.038	—	I
IRAS 20293+3952										
20 30 57.60	+40 02 22.7	16.327±0.096	11.954±0.019	9.509±0.016	7.538±0.002	7.392±0.002	7.236±0.002	6.732±0.002	—	IRe
20 31 00.75	+40 02 04.1	—	—	14.456±0.090	12.996±0.008	12.398±0.005	11.709±0.041	10.599±0.058	7.628±0.083	II
20 31 04.55	+40 01 46.0	—	—	—	14.132±0.019	13.636±0.014	13.274±0.082	12.257±0.149	—	II
20 31 08.05	+40 04 48.7	—	—	—	13.623±0.022	13.324±0.025	12.805±0.060	12.134±0.125	—	II
20 31 08.59	+40 02 37.5	16.156±0.084	15.038±0.074	14.087±0.067	13.467±0.037	13.109±0.070	12.550±0.238	—	—	IRe
20 31 08.68	+40 03 48.5	—	—	—	9.907±0.004	7.745±0.003	5.924±0.003	4.647±0.002	1.127±0.007	I
20 31 08.75	+40 02 47.4	—	—	12.249±0.027	9.227±0.003	8.203±0.003	7.375±0.005	6.675±0.011	2.616±0.009	I
20 31 09.52	+40 00 22.1	—	14.943±0.067	14.175±0.069	13.545±0.008	13.338±0.008	13.280±0.040	12.734±0.118	—	II

Table 3—Continued

RA <sup>†</sup>	DEC <sup>†</sup>	<i>J</i>	<i>H</i>	<i>Ks</i>	[3.6]	[4.5]	[5.8]	[8.0]	[24] <sup>‡</sup>	Remark*
20 31 09.59	+40 03 04.8	—	14.659±0.085	12.952±0.044	11.032±0.049	10.305±0.044	9.542±0.218	—	—	IRe
20 31 09.85	+40 02 37.6	—	—	13.741±0.053	11.988±0.016	11.381±0.015	11.021±0.074	10.401±0.140	—	II
20 31 10.32	+40 03 16.5	13.528±0.042	10.739±0.024	8.316±0.017	5.543±0.005	4.590±0.003	3.303±0.003	2.325±0.005	≤ 0.626	High <sup>7</sup>
20 31 10.41	+40 04 08.2	15.096±0.040	13.330±0.028	12.108±0.022	10.358±0.003	9.854±0.003	9.334±0.006	8.477±0.010	—	II
20 31 11.26	+40 03 07.6	11.403±0.032	9.439±0.024	8.049±0.016	6.775±0.016	6.269±0.013	5.774±0.116	—	≤ 0.626	High <sup>8</sup>
20 31 11.78	+40 03 48.8	—	14.997±0.068	13.814±0.052	12.160±0.011	11.537±0.010	11.004±0.052	10.403±0.107	—	II
20 31 12.38	+40 03 10.2	—	—	—	11.130±0.056	9.371±0.023	7.397±0.049	6.325±0.084	—	I
20 31 12.48	+40 03 20.0	—	14.873±0.076	12.809±0.040	9.594±0.016	8.484±0.011	7.494±0.041	6.632±0.083	—	I
20 31 13.87	+40 06 52.4	—	—	—	13.564±0.031	12.800±0.027	11.999±0.042	11.360±0.078	—	II
20 31 14.52	+40 03 26.1	13.446±0.023	12.534±0.026	12.040±0.028	11.656±0.028	11.293±0.043	11.189±0.120	—	—	IRe
20 31 14.64	+40 03 18.6	—	14.717±0.074	12.312±0.028	10.110±0.007	9.364±0.006	8.751±0.016	8.147±0.027	3.721±0.079	I
20 31 15.35	+40 02 53.8	—	—	14.257±0.078	12.146±0.008	11.394±0.008	10.673±0.025	9.817±0.061	—	II
20 31 15.69	+40 03 11.2	—	14.459±0.042	13.150±0.031	11.492±0.007	10.824±0.006	10.236±0.016	9.428±0.026	—	II
20 31 16.27	+40 02 55.2	—	—	14.381±0.099	12.059±0.007	11.277±0.009	10.634±0.020	9.898±0.043	—	II
20 31 17.05	+40 03 40.1	—	14.327±0.059	13.118±0.047	11.721±0.004	11.292±0.004	10.981±0.017	10.381±0.051	—	II
20 31 17.17	+40 03 49.8	—	—	—	14.618±0.032	13.905±0.030	13.519±0.147	12.638±0.200	—	II
20 31 17.46	+40 03 28.5	16.012±0.080	13.758±0.028	12.576±0.026	11.765±0.004	11.473±0.004	11.186±0.010	10.945±0.031	6.313±0.156	II
20 31 18.23	+40 02 53.9	—	—	—	13.548±0.028	12.675±0.018	11.700±0.022	10.437±0.046	4.856±0.016	I
20 31 22.88	+40 03 09.7	—	—	—	11.896±0.006	10.910±0.003	10.262±0.014	9.663±0.043	6.457±0.064	II
20 31 22.98	+40 02 21.1	—	—	—	14.660±0.015	14.365±0.026	13.879±0.100	12.890±0.181	—	II
20 31 25.54	+40 01 59.2	—	14.430±0.044	12.860±0.030	11.236±0.002	10.570±0.003	10.026±0.005	9.412±0.011	5.406±0.017	I
20 31 27.93	+40 03 35.6	14.312±0.027	13.540±0.031	13.236±0.040	12.782±0.044	12.417±0.071	—	—	—	IRe
20 31 28.05	+40 03 40.5	13.808±0.039	12.615±0.036	11.929±0.030	11.146±0.016	10.760±0.019	10.156±0.072	8.492±0.066	—	I/II
W75 N										
20 38 19.40	+42 36 57.1	—	—	12.029±0.047	9.531±0.003	8.465±0.003	7.431±0.002	6.154±0.002	—	I
20 38 20.48	+42 37 13.6	—	—	—	13.491±0.014	12.947±0.019	12.666±0.072	12.162±0.243	—	II
20 38 22.84	+42 37 41.9	15.671±0.071	14.019±0.041	12.928±0.027	11.770±0.003	11.366±0.003	11.011±0.016	10.659±0.055	—	IRe
20 38 23.18	+42 36 41.6	—	—	14.219±0.068	12.190±0.006	11.798±0.006	11.188±0.040	10.779±0.134	—	II
20 38 23.49	+42 37 37.4	—	15.191±0.097	13.968±0.041	12.702±0.011	12.156±0.006	11.856±0.028	11.700±0.111	—	IRe
20 38 25.02	+42 35 27.2	—	14.762±0.086	13.644±0.041	12.360±0.006	11.942±0.007	11.585±0.042	10.861±0.080	—	II
20 38 25.25	+42 36 26.9	—	—	14.648±0.095	13.424±0.018	12.937±0.023	12.495±0.063	11.309±0.144	—	I
20 38 25.89	+42 36 35.5	—	—	—	14.268±0.033	13.606±0.064	12.907±0.082	11.756±0.126	—	I
20 38 26.86	+42 39 29.1	—	—	—	12.491±0.015	11.801±0.008	11.148±0.061	10.273±0.093	—	II

Table 3—Continued

RA <sup>†</sup>	DEC <sup>†</sup>	<i>J</i>	<i>H</i>	<i>Ks</i>	[3.6]	[4.5]	[5.8]	[8.0]	[24] <sup>‡</sup>	Remark*
20 38 27.34	+42 38 29.8	—	14.387±0.057	13.284±0.039	12.301±0.006	11.824±0.004	11.451±0.035	10.699±0.100	—	II
20 38 28.58	+42 37 01.1	—	—	14.710±0.099	13.504±0.008	12.989±0.007	12.445±0.064	11.632±0.176	—	II
20 38 31.27	+42 38 24.9	—	—	14.287±0.075	12.250±0.008	11.526±0.005	10.921±0.023	10.285±0.078	—	II
20 38 31.63	+42 38 34.7	—	—	—	11.900±0.004	11.124±0.004	10.452±0.023	9.801±0.046	4.452±0.010	I
20 38 31.96	+42 37 40.9	15.507±0.062	13.837±0.042	13.002±0.030	12.109±0.012	11.668±0.013	11.090±0.096	10.706±0.229	—	IRe
20 38 32.20	+42 36 37.3	—	14.864±0.095	13.549±0.057	11.862±0.009	11.306±0.007	10.975±0.062	10.584±0.160	—	IRe
20 38 32.31	+42 39 45.2	—	—	14.735±0.095	10.431±0.002	9.006±0.002	7.888±0.003	7.108±0.003	3.228±0.015	I
20 38 32.29	+42 36 31.4	—	—	—	11.340±0.007	10.475±0.005	9.810±0.016	9.255±0.053	—	I
20 38 32.67	+42 40 07.1	—	—	—	14.162±0.032	13.264±0.021	12.589±0.087	11.403±0.121	—	I
20 38 32.82	+42 39 35.3	—	—	—	12.225±0.027	10.368±0.020	9.231±0.014	8.621±0.036	—	I
20 38 33.14	+42 38 07.4	—	—	—	13.172±0.028	12.570±0.023	12.042±0.166	10.892±0.157	—	I
20 38 33.29	+42 39 32.3	—	—	14.559±0.091	12.833±0.019	11.736±0.010	11.023±0.026	10.575±0.127	—	I
20 38 33.29	+42 39 38.5	—	—	—	11.734±0.006	9.848±0.004	8.429±0.004	7.377±0.013	3.152±0.010	I
20 38 33.42	+42 37 06.4	15.723±0.065	13.955±0.060	13.120±0.069	12.087±0.068	11.665±0.065	—	—	—	IRe
20 38 33.60	+42 37 27.3	—	—	14.320±0.068	11.537±0.019	10.690±0.023	10.093±0.155	9.298±0.157	—	I
20 38 33.64	+42 36 53.2	—	14.363±0.054	12.969±0.027	11.415±0.008	10.893±0.010	10.419±0.082	9.750±0.095	—	II
20 38 33.73	+42 39 21.9	—	—	14.560±0.100	12.090±0.012	11.167±0.008	10.350±0.014	9.675±0.066	—	I
20 38 33.83	+42 36 15.5	—	—	13.551±0.041	11.983±0.006	11.284±0.005	10.688±0.021	10.056±0.057	—	II
20 38 34.06	+42 39 55.8	—	—	—	13.791±0.029	12.447±0.025	12.017±0.093	12.116±0.183	5.685±0.061*	I
20 38 34.14	+42 37 58.2	—	14.147±0.054	12.890±0.039	11.404±0.019	10.708±0.011	10.000±0.087	9.208±0.197	—	II
20 38 34.17	+42 38 40.9	15.897±0.089	13.363±0.040	11.936±0.028	10.541±0.005	9.907±0.005	9.317±0.029	8.796±0.038	—	II
20 38 34.39	+42 39 18.1	15.990±0.092	14.084±0.053	13.152±0.037	11.793±0.006	11.288±0.007	10.795±0.040	10.380±0.098	—	II
20 38 34.51	+42 38 07.5	—	—	—	12.548±0.039	11.591±0.023	10.909±0.160	9.629±0.218	—	I
20 38 34.66	+42 36 20.5	—	14.795±0.087	13.826±0.051	12.847±0.012	12.511±0.008	11.939±0.089	10.731±0.160	—	I/II
20 38 35.28	+42 36 50.1	—	—	13.600±0.057	11.476±0.019	10.649±0.020	10.186±0.058	9.666±0.056	—	I
20 38 35.37	+42 37 13.7	—	12.771±0.045	9.482±0.028	5.817±0.004	4.757±0.003	3.556±0.009	2.451±0.010	≪ 0.626	High <sup>9</sup>
20 38 36.20	+42 38 07.8	15.614±0.075	13.649±0.049	12.522±0.046	10.824±0.150	10.570±0.151	—	—	—	IRe
20 38 36.26	+42 38 26.0	—	14.969±0.083	13.146±0.019	11.802±0.021	11.253±0.024	10.482±0.085	9.619±0.144	—	II
20 38 36.34	+42 39 47.6	14.821±0.040	12.920±0.027	11.784±0.023	10.352±0.007	9.698±0.005	9.020±0.018	8.250±0.064	—	II
20 38 36.43	+42 40 41.8	15.943±0.089	14.208±0.047	13.404±0.034	12.713±0.015	12.256±0.012	11.718±0.053	10.829±0.100	7.894±0.144	II
20 38 36.89	+42 39 52.1	15.753±0.073	14.848±0.071	14.374±0.069	13.709±0.082	13.432±0.098	—	—	—	IRe
20 38 37.01	+42 39 34.8	14.604±0.064	—	12.264±0.071	10.198±0.083	9.874±0.063	7.222±0.116	5.485±0.112	—	I/II
20 38 37.29	+42 39 33.0	13.623±0.063	—	11.078±0.063	9.493±0.057	8.956±0.032	—	5.288±0.114	0.2±0.1**	II
20 38 37.50	+42 39 10.4	15.681±0.073	13.739±0.045	12.655±0.036	11.377±0.009	10.815±0.010	10.204±0.023	9.532±0.062	—	II
20 38 37.52	+42 39 26.3	14.973±0.087	12.349±0.076	10.662±0.042	8.828±0.013	8.251±0.012	7.356±0.026	6.027±0.052	—	I

Table 3—Continued

RA <sup>†</sup>	DEC <sup>†</sup>	<i>J</i>	<i>H</i>	<i>Ks</i>	[3.6]	[4.5]	[5.8]	[8.0]	[24] <sup>‡</sup>	Remark*
20 38 37.73	+42 37 59.4	13.950±0.039	11.457±0.037	10.066±0.045	8.922±0.105	8.074±0.094	—	—	≪ 0.626	High <sup>10</sup>
20 38 37.87	+42 40 00.1	—	—	14.438±0.079	12.431±0.023	11.661±0.015	11.030±0.108	10.216±0.250	—	II
20 38 37.91	+42 39 21.4	14.707±0.040	12.805±0.034	11.714±0.024	10.091±0.012	9.495±0.009	8.857±0.022	7.834±0.037	—	II
20 38 38.15	+42 39 07.5	—	14.825±0.084	13.822±0.064	12.556±0.021	12.084±0.028	—	—	—	IRe
20 38 38.46	+42 39 50.0	—	—	11.608±0.019	10.560±0.014	9.386±0.031	8.097±0.051	—	—	I
20 38 38.64	+42 39 39.2	—	15.073±0.091	13.484±0.037	11.109±0.008	10.007±0.007	9.165±0.026	8.554±0.061	—	I
20 38 38.74	+42 39 52.3	15.103±0.048	13.418±0.041	12.415±0.027	11.192±0.021	10.785±0.041	—	—	—	IRe
20 38 38.82	+42 37 17.6	12.614±0.025	10.984±0.029	9.723±0.027	8.353±0.006	7.780±0.005	7.051±0.027	5.695±0.043	—	High <sup>11</sup>
20 38 38.83	+42 39 26.6	14.209±0.032	12.337±0.032	11.126±0.027	9.889±0.005	9.497±0.006	9.191±0.023	9.199±0.074	—	IRe
20 38 38.86	+42 37 43.9	—	13.672±0.023	12.129±0.023	10.325±0.044	9.725±0.047	8.590±0.160	7.186±0.205	—	I
20 38 39.01	+42 39 22.0	—	—	11.576±0.012	10.721±0.013	9.838±0.036	8.992±0.076	—	—	I
20 38 39.37	+42 37 11.6	—	13.657±0.090	12.261±0.081	10.923±0.063	10.144±0.047	9.276±0.034	—	—	IRe
20 38 39.47	+42 38 56.9	—	—	14.606±0.093	12.737±0.032	12.120±0.035	11.554±0.071	10.881±0.140	—	II
20 38 39.89	+42 36 42.6	—	—	14.575±0.099	13.998±0.107	13.792±0.122	12.758±0.177	12.158±0.187	—	II
20 38 40.07	+42 38 09.2	16.130±0.098	14.234±0.061	13.218±0.042	11.319±0.111	10.917±0.112	—	—	—	IRe
20 38 40.16	+42 39 53.5	—	14.383±0.082	12.799±0.055	11.294±0.094	10.535±0.067	8.885±0.171	—	0.900±0.004	High <sup>12</sup>
20 38 40.42	+42 35 45.9	15.159±0.045	14.505±0.065	14.286±0.071	13.551±0.126	13.399±0.111	—	—	—	IRe
20 38 41.16	+42 39 23.1	—	13.395±0.040	11.369±0.023	9.372±0.004	8.828±0.003	8.291±0.002	7.741±0.008	3.539±0.052	II
20 38 42.63	+42 35 43.7	—	—	11.737±0.033	10.489±0.003	9.997±0.003	9.686±0.012	9.224±0.022	5.681±0.169	II
20 38 43.05	+42 39 04.5	—	—	—	13.327±0.039	12.638±0.035	12.144±0.120	11.143±0.197	—	II
20 38 43.06	+42 36 59.7	—	—	13.593±0.056	10.989±0.009	10.306±0.007	9.797±0.025	9.316±0.042	—	II
20 38 43.84	+42 37 13.7	—	—	14.696±0.081	13.080±0.013	12.548±0.028	12.085±0.060	11.347±0.132	—	II
20 38 43.86	+42 36 52.9	—	—	14.213±0.060	12.138±0.013	11.345±0.007	10.842±0.017	10.219±0.085	—	II
20 38 43.93	+42 37 44.6	—	—	—	12.958±0.045	12.189±0.046	11.133±0.073	9.951±0.176	—	I
20 38 44.42	+42 38 58.4	—	—	14.520±0.081	13.101±0.020	12.514±0.013	11.638±0.094	10.666±0.242	—	II
20 38 45.04	+42 39 40.2	—	—	—	13.900±0.013	13.007±0.012	12.200±0.053	11.318±0.101	—	I
20 38 45.56	+42 38 01.9	—	—	—	12.996±0.025	12.278±0.014	11.392±0.081	10.126±0.066	—	I
20 38 46.22	+42 40 01.5	—	—	—	13.605±0.011	12.997±0.009	12.845±0.066	12.267±0.188	—	II
20 38 46.69	+42 37 44.0	—	—	13.625±0.044	12.178±0.008	11.885±0.010	11.480±0.064	10.949±0.174	—	II
20 38 47.43	+42 38 19.9	—	—	14.192±0.065	13.136±0.013	12.909±0.013	12.211±0.087	11.221±0.187	—	II
20 38 48.52	+42 37 30.0	—	—	—	13.911±0.020	13.383±0.015	12.589±0.099	11.545±0.159	—	II
20 38 49.47	+42 36 08.5	—	—	—	12.123±0.007	10.261±0.003	9.130±0.007	8.200±0.028	4.367±0.014	I
20 38 51.13	+42 35 51.7	—	—	—	13.737±0.016	13.167±0.020	12.645±0.062	11.538±0.185	—	I

Table 3—Continued

RA <sup>†</sup>	DEC <sup>†</sup>	<i>J</i>	<i>H</i>	<i>Ks</i>	[3.6]	[4.5]	[5.8]	[8.0]	[24] <sup>‡</sup>	Remark*
22 18 45.18	+56 04 49.3	15.020±0.052	14.149±0.059	13.530±0.052	12.824±0.010	12.451±0.010	12.185±0.078	11.147±0.169	—	II
22 18 45.73	+56 03 52.6	—	14.950±0.089	14.180±0.075	12.817±0.023	12.524±0.014	11.655±0.170	—	—	IRe
22 18 46.31	+56 05 03.4	—	—	—	14.182±0.016	13.874±0.018	13.703±0.037	13.058±0.071	—	II
22 18 47.26	+56 05 58.4	15.913±0.097	14.767±0.090	14.133±0.071	12.870±0.037	12.540±0.021	12.156±0.174	—	—	IRe
22 18 47.54	+56 05 11.2	—	—	—	15.043±0.021	14.544±0.023	14.133±0.061	13.072±0.070	—	II
22 18 48.01	+56 05 02.9	—	—	—	14.347±0.015	13.848±0.020	13.453±0.042	12.997±0.096	—	II
22 18 49.37	+56 05 46.5	14.128±0.031	13.120±0.037	12.394±0.033	11.297±0.003	10.824±0.003	10.320±0.004	9.549±0.010	—	II
22 18 49.40	+56 04 31.0	—	—	—	15.127±0.051	14.550±0.042	14.153±0.151	13.245±0.230	—	II
22 18 49.86	+56 06 18.5	—	—	—	13.732±0.016	13.486±0.014	13.500±0.090	12.536±0.111	—	II
22 18 50.13	+56 03 40.8	15.555±0.072	14.556±0.075	13.805±0.057	12.616±0.048	12.106±0.025	11.944±0.245	—	—	IRe
22 18 50.78	+56 05 06.8	—	—	—	14.304±0.038	13.990±0.022	13.566±0.044	12.893±0.064	—	II
22 18 52.22	+56 06 13.7	—	—	—	13.835±0.025	13.393±0.027	13.071±0.048	12.275±0.068	—	II
22 18 52.49	+56 06 48.8	15.849±0.086	—	—	13.861±0.013	13.587±0.015	13.036±0.079	12.612±0.141	—	II
22 18 52.69	+56 06 05.1	14.392±0.032	13.444±0.038	12.604±0.033	11.494±0.004	10.997±0.003	10.366±0.006	9.244±0.008	6.996±0.100	II
22 18 53.62	+56 06 24.8	15.779±0.084	—	14.292±0.091	13.682±0.016	13.410±0.016	13.149±0.055	12.151±0.087	—	II
22 18 54.35	+56 04 59.6	—	—	—	15.135±0.064	14.341±0.037	13.548±0.051	12.361±0.103	—	I
22 18 55.39	+56 05 12.9	—	—	—	13.456±0.025	13.088±0.031	12.710±0.047	11.766±0.051	—	II
22 18 55.67	+56 05 16.3	—	—	—	12.832±0.025	12.415±0.022	11.921±0.027	10.884±0.020	—	II
22 18 55.67	+56 04 55.4	—	—	—	14.589±0.039	14.275±0.037	13.948±0.086	13.240±0.117	—	II
22 18 56.14	+56 05 48.6	11.113±0.024	10.983±0.032	10.856±0.026	10.865±0.004	10.874±0.004	10.755±0.009	10.745±0.043	5.022±0.040	II
22 18 56.27	+56 05 32.3	—	—	—	13.709±0.021	13.371±0.025	13.113±0.058	12.284±0.076	—	II
22 18 57.18	+56 05 02.0	12.895±0.027	12.669±0.036	12.535±0.030	12.523±0.008	12.519±0.011	12.440±0.024	12.341±0.072	5.719±0.061*	II
22 18 57.62	+56 07 07.0	14.513±0.062	13.788±0.067	13.247±0.057	12.551±0.017	12.304±0.018	11.905±0.021	10.794±0.042	—	I/II
22 18 57.71	+56 04 27.5	—	—	—	14.889±0.053	14.477±0.040	14.013±0.136	13.007±0.147	—	II
22 18 57.82	+56 05 52.6	—	—	—	14.702±0.032	14.026±0.024	13.804±0.092	12.896±0.173	—	II
22 18 58.38	+56 04 23.3	15.038±0.054	14.818±0.095	14.452±0.091	14.145±0.054	13.946±0.041	—	—	—	IRe
22 18 58.68	+56 07 23.6	8.931±0.027	8.896±0.038	8.806±0.029	8.611±0.003	8.533±0.003	8.443±0.004	8.443±0.008	—	IRe
22 18 58.71	+56 04 54.5	—	—	—	14.739±0.018	14.022±0.012	13.410±0.058	12.698±0.087	—	II
22 18 58.76	+56 05 18.8	—	—	—	14.950±0.033	14.521±0.022	14.202±0.071	13.625±0.118	—	II
22 18 59.21	+56 05 00.6	—	—	—	13.446±0.009	13.065±0.008	12.663±0.033	12.208±0.069	—	II
22 18 59.72	+56 05 13.9	—	—	—	13.744±0.011	13.256±0.011	12.750±0.026	12.090±0.031	—	II
22 19 00.08	+56 03 14.8	14.409±0.041	14.326±0.084	14.223±0.075	13.747±0.077	13.742±0.066	—	—	—	IRe
22 19 00.18	+56 05 34.7	—	—	—	14.802±0.024	14.256±0.021	13.743±0.074	12.564±0.060	—	I
22 19 00.26	+56 06 41.4	—	—	—	13.707±0.016	13.249±0.011	12.780±0.045	12.298±0.112	—	II

Table 3—Continued

RA <sup>†</sup>	DEC <sup>†</sup>	<i>J</i>	<i>H</i>	<i>Ks</i>	[3.6]	[4.5]	[5.8]	[8.0]	[24] <sup>‡</sup>	Remark*
22 19 02.01	+56 07 08.5	15.270±0.056	14.481±0.053	13.862±0.052	13.070±0.014	12.676±0.012	12.327±0.024	11.843±0.047	—	II
22 19 02.01	+56 08 00.7	—	—	—	14.705±0.034	14.267±0.041	14.050±0.119	12.965±0.173	—	II
22 19 02.18	+56 07 25.8	—	—	—	13.747±0.037	13.380±0.038	13.006±0.054	12.336±0.065	—	II
22 19 02.26	+56 06 36.5	—	—	—	13.591±0.012	13.288±0.012	12.899±0.040	12.067±0.075	—	II
22 19 02.62	+56 06 17.3	—	—	—	14.959±0.031	14.574±0.028	14.038±0.082	13.163±0.177	—	II
22 19 02.77	+56 05 40.6	15.718±0.098	—	14.373±0.096	13.702±0.018	13.421±0.016	12.686±0.056	11.228±0.099	—	I/II
22 19 03.80	+56 05 10.3	—	—	14.352±0.086	13.326±0.017	12.954±0.017	12.516±0.058	11.574±0.073	—	II
22 19 04.36	+56 05 50.8	—	—	—	15.065±0.042	14.314±0.042	13.823±0.188	12.684±0.196	—	I
22 19 04.46	+56 05 36.0	—	—	14.400±0.089	13.276±0.014	12.792±0.014	12.347±0.080	11.694±0.097	—	II
22 19 04.50	+56 05 07.8	—	—	—	14.300±0.033	13.682±0.021	13.067±0.139	11.783±0.206	—	I
22 19 05.21	+56 08 25.8	15.052±0.061	14.240±0.068	13.573±0.055	12.759±0.006	12.454±0.007	12.038±0.022	11.079±0.043	—	II
22 19 05.72	+56 04 52.7	—	14.742±0.092	13.724±0.067	12.543±0.127	11.716±0.049	—	—	—	IRe
22 19 05.82	+56 05 18.8	—	15.059±0.097	14.139±0.061	12.013±0.008	11.568±0.008	11.249±0.050	10.421±0.100	—	II
22 19 05.79	+56 07 05.9	—	—	—	13.806±0.007	13.569±0.013	13.200±0.029	12.794±0.054	—	II
22 19 05.94	+56 05 41.7	—	—	—	14.125±0.018	13.725±0.025	12.992±0.163	11.932±0.146	—	II
22 19 06.02	+56 05 55.3	15.355±0.061	14.251±0.054	13.557±0.047	12.410±0.006	11.978±0.004	11.629±0.024	10.753±0.043	—	II
22 19 07.65	+56 05 28.6	15.827±0.092	14.675±0.064	13.733±0.058	12.327±0.025	11.811±0.028	11.646±0.166	—	—	IRe
22 19 08.03	+56 04 11.1	—	14.842±0.086	13.321±0.047	10.996±0.007	10.090±0.003	9.156±0.016	8.190±0.039	4.487±0.069	I
22 19 08.30	+56 05 11.0	11.965±0.035	11.228±0.045	10.474±0.033	9.074±0.011	8.562±0.012	7.390±0.028	5.902±0.038	1.305±0.008	II
22 19 08.45	+56 05 28.7	15.626±0.092	14.406±0.068	13.727±0.064	12.688±0.039	12.071±0.047	11.519±0.160	—	—	IRe
22 19 09.39	+56 04 45.7	15.279±0.071	14.094±0.056	13.175±0.046	10.549±0.017	10.256±0.037	7.507±0.015	5.775±0.018	1.175±0.002	II
22 19 09.38	+56 05 00.4	—	13.306±0.092	11.331±0.052	7.882±0.007	6.685±0.005	5.552±0.007	4.449±0.012	0.3±0.1**	I
22 19 09.70	+56 05 04.8	—	—	—	8.097±0.008	7.042±0.007	5.969±0.008	4.969±0.016	—	I
22 19 09.84	+56 07 37.4	—	—	—	14.546±0.067	14.064±0.032	13.684±0.059	13.006±0.133	—	II
22 19 09.94	+56 08 20.5	—	—	—	14.614±0.017	14.099±0.018	13.705±0.070	12.698±0.138	—	II
22 19 10.42	+56 02 11.5	13.786±0.027	12.895±0.039	12.215±0.025	11.363±0.005	10.926±0.003	10.527±0.022	9.633±0.052	—	II
22 19 10.94	+56 06 07.6	—	—	—	14.477±0.025	14.199±0.022	13.795±0.048	13.171±0.088	—	II
22 19 11.45	+56 02 53.2	15.832±0.087	14.918±0.094	14.261±0.076	13.261±0.015	12.845±0.014	12.947±0.109	—	—	IRe
22 19 11.62	+56 02 36.6	11.025±0.038	10.874±0.039	10.782±0.033	10.772±0.008	10.671±0.009	10.583±0.025	9.777±0.054	4.561±0.026	II
22 19 12.07	+56 07 09.1	—	—	—	14.114±0.021	13.791±0.017	12.987±0.067	11.655±0.077	—	I/II
22 19 12.65	+56 02 03.6	15.064±0.054	14.353±0.084	13.829±0.066	12.865±0.015	12.427±0.008	12.052±0.083	11.098±0.173	—	II
22 19 13.80	+56 07 48.4	14.745±0.053	14.444±0.074	14.067±0.071	13.764±0.010	13.675±0.010	13.636±0.064	—	—	IRe
22 19 15.06	+56 06 53.0	—	—	—	14.043±0.008	13.752±0.010	13.465±0.029	12.844±0.045	—	II
22 19 15.18	+56 07 02.8	—	—	—	14.478±0.026	14.241±0.043	13.909±0.069	13.280±0.084	—	II
22 19 17.51	+56 03 14.2	—	—	—	14.814±0.026	14.445±0.023	14.085±0.049	13.401±0.090	—	II

Table 3—Continued

RA <sup>†</sup>	DEC <sup>†</sup>	<i>J</i>	<i>H</i>	<i>Ks</i>	[3.6]	[4.5]	[5.8]	[8.0]	[24] <sup>‡</sup>	Remark*
22 19 17.89	+56 04 01.7	—	—	—	14.444±0.015	14.057±0.017	13.886±0.104	13.136±0.213	—	II
22 19 18.33	+56 02 56.0	—	—	—	15.177±0.034	14.934±0.027	14.756±0.084	14.151±0.121	—	II
22 19 19.80	+56 03 01.5	—	—	—	14.251±0.025	13.386±0.015	12.660±0.016	11.928±0.031	7.246±0.038	I
22 19 20.39	+56 03 49.3	—	—	—	15.110±0.025	14.846±0.032	14.733±0.128	14.031±0.137	—	II
22 19 20.78	+56 06 12.3	—	—	—	15.509±0.039	15.072±0.040	14.546±0.096	13.892±0.105	—	II
22 19 21.06	+56 06 31.0	—	—	—	14.443±0.013	14.111±0.013	13.777±0.055	13.367±0.066	—	II
22 19 21.24	+56 06 40.1	—	—	—	14.756±0.020	14.584±0.016	14.480±0.114	13.548±0.116	8.345±0.093	II
22 19 21.35	+56 04 48.3	11.740±0.024	11.571±0.032	11.473±0.023	11.446±0.002	11.460±0.003	11.472±0.008	11.374±0.018	6.394±0.016	II
22 19 21.58	+56 04 20.8	—	—	—	13.740±0.014	13.315±0.012	12.919±0.024	12.136±0.047	—	II
22 19 21.80	+56 06 03.9	—	—	—	15.277±0.019	15.059±0.030	14.670±0.067	14.258±0.091	—	II
22 19 21.81	+56 03 06.1	11.624±0.024	11.480±0.031	11.341±0.022	11.371±0.005	11.415±0.005	11.359±0.009	11.084±0.031	5.497±0.011	II
22 19 22.67	+56 05 57.0	—	—	—	15.179±0.017	14.699±0.020	14.466±0.058	13.643±0.060	—	II
22 19 22.85	+56 06 02.3	—	—	—	13.969±0.012	13.736±0.013	13.611±0.045	13.074±0.049	—	II
22 19 23.28	+56 03 54.9	—	—	—	14.338±0.009	14.060±0.013	13.701±0.037	12.926±0.051	—	II
22 19 23.81	+56 06 00.4	—	—	—	14.304±0.012	14.034±0.015	13.774±0.044	13.223±0.071	—	II
22 19 24.50	+56 03 36.0	—	—	—	14.487±0.031	14.195±0.025	13.920±0.053	13.399±0.118	—	II
22 19 24.54	+56 03 21.3	12.454±0.026	12.308±0.036	12.279±0.034	12.350±0.023	12.264±0.016	12.414±0.061	12.226±0.082	7.554±0.070	II
22 19 25.98	+56 04 10.2	12.667±0.022	12.489±0.032	12.414±0.028	12.428±0.007	12.414±0.006	12.382±0.024	12.159±0.053	6.440±0.026	II
22 19 27.48	+56 04 47.8	—	—	—	14.483±0.026	13.967±0.029	13.786±0.046	13.071±0.048	—	II
22 19 27.90	+56 06 08.2	—	—	—	14.861±0.012	14.536±0.020	14.172±0.065	13.716±0.108	—	II
22 19 28.81	+56 04 53.9	—	—	—	14.948±0.014	14.686±0.021	14.458±0.049	13.808±0.066	—	II
22 19 31.32	+56 06 00.8	15.960±0.095	15.054±0.092	14.496±0.089	13.821±0.011	13.447±0.012	13.350±0.043	12.831±0.067	—	II

<sup>†</sup>J2000.0 coordinates

<sup>‡</sup>source significantly saturated in the MIPS 24  $\mu\text{m}$  band are marked with the photometry of  $\ll 0.626$ , implying a flux level much higher than the saturation limit of 4.1 Jy

\*I — protostars; II — class II; I/II — class I/II; IRe — YSOs only identifiable in the 2MASS-IRAC diagrams; High — candidates of intermediate- to high-mass YSOs, see the notes below for details

▲ most likely attributed to the millimeter source(s) in Zhang et al. (2007)

\*blended with a neighboring brighter object in the MIPS 24  $\mu\text{m}$  band — magnitudes derived from the PSF-fitting photometry

\*\*slightly saturated in the MIPS 24  $\mu\text{m}$  band — magnitudes derived by manually scaling the PSF, subtracting the PSF from the image, and comparing the residual of the PSF wing with a sky value

<sup>1</sup>the exciting source of the surrounding reflection nebula, associated with the luminous IRAS source (Hunter et al. 1995), a B2 star at 3 Myr from its position in the *J* vs.

*J – H* diagram (Chen et al. 2005)

<sup>2</sup>the exciting source of the surrounding reflection nebula, coincident with the IRAS 12  $\mu\text{m}$  emission peak, a candidate Herbig Ae/Be star suggested by Porras et al. (2000)

<sup>3</sup>the exciting source of the surrounding reflection nebula, spectral type of B2 to B3 estimated from the centimeter free-free emission observed by Martí et al. (1993)

<sup>4</sup>an intermediate- to high-mass pre-main-sequence star suggested by Aspin & Geballe (1992)

<sup>5</sup>the exciting source of the surrounding reflection nebula, spectral type of B2 to B3 estimated from the centimeter free-free emission observed by Martí et al. (1993), an intermediate- to high-mass pre-main-sequence star suggested by Aspin & Geballe (1992)

<sup>6</sup>the exciting source of the surrounding reflection nebula

<sup>7</sup>an intermediate-mass YSO suggested by Palau et al. (2007)

<sup>8</sup>the exciting source of the surrounding reflection nebula, a young B1 star surrounded by a relatively extended UC HII region (Palau et al. 2007)

<sup>9</sup>a young B star with a 1 – 20  $\mu\text{m}$  luminosity of  $254L_\odot$  (Persi et al. 2006) to  $540L_\odot$  (Moore et al. 1991)

<sup>10</sup>the exciting source of the surrounding reflection nebula, a B0.5 star at 1 – 5 Myr surrounded by the expanding HII region W75 N(A) and within a warm dust shell (Haschick et al. 1981; Shepherd et al. 2003, 2004b)

<sup>11</sup>a young intermediate-mass star with a 1 – 20  $\mu\text{m}$  luminosity of  $36L_\odot$  (Persi et al. 2006)

<sup>12</sup>the exciting source of the surrounding reflection nebula

Table 4. Completeness Estimates

Source Name	[3.6] <sup>a</sup>	Completeness <sup>b</sup>
AFGL 5142	15	84%
IRAS 05358+3543	14.5	79%
G192.16-3.82	15	81%
HH 80-81	13.5	84%
IRAS 19410+2336	13.5	73%
IRAS 20126+4104	14.5	73%
IRAS 20293+3952	13	85%
W75 N	12.5	75%
IRAS 22172+5549	14.5	76%

<sup>a</sup>Completeness magnitudes at 3.6  $\mu$ m derived from Figure 3.

<sup>b</sup>For sources with the 3.6  $\mu$ m photometry brighter than the completeness magnitude, the fraction of the sources that can be placed on one or more color-color diagrams.

Table 5. Infrared Counterparts of Millimeter Cores

Source	R.A. (J2000)	Decl. (J2000)	[3.6]	[4.5]	[5.8]	[8.0]	[24]	Ref. <sup>†</sup>
AFGL 5142	05 30 47.94	+33 47 54.2	—	—	—	—	0.632±0.005	1
IRAS 05358+3543	05 39 13.04	+35 45 51.2	—	7.582±0.020	6.250±0.015	5.098±0.011	≤0.626	2, 3
G192.16-3.82	05 58 13.55	+16 31 58.2	9.063±0.009	7.726±0.007	6.915±0.007	5.954±0.014	≤0.626	4, 5
HH 80-81	18 19 12.11	-20 47 31.0	—	—	4.104±0.050	3.040±0.081	≤0.626	6
IRAS 19410+2336	19 43 11.25	+23 44 03.2	6.682±0.018	4.624±0.008	3.365±0.004	2.780±0.008	≤0.626	7, 8
IRAS 20126+4104	20 14 25.97	+41 13 33.1	—	—	—	5.422±0.060	≤0.626	9, 10
IRAS 20293+3952	20 31 12.92	+40 03 23.0	—	—	—	—	1.123±0.021	11, 12, 13
W75 N	20 38 36.49	+42 37 33.5	—	6.161±0.22	4.451±0.017	3.346±0.018	≤0.626	14

<sup>†</sup>References of interferometric millimeter continuum observations: 1. Zhang et al. (2007); 2. Beuther et al. (2002); 3. Beuther et al. (2007); 4. Shepherd et al. (1999); 5. Shepherd et al. (2004a); 6. Gómez et al. (2003); 7. Beuther et al. (2003); 8. Beuther & Schilke (2004a); 9. Shepherd et al. (2000); 10. Cesaroni et al. (2005); 11. Beuther et al. (2004b); 12. Beuther et al. (2004c); 13. Palau et al. (2007); 14. Shepherd (2001)

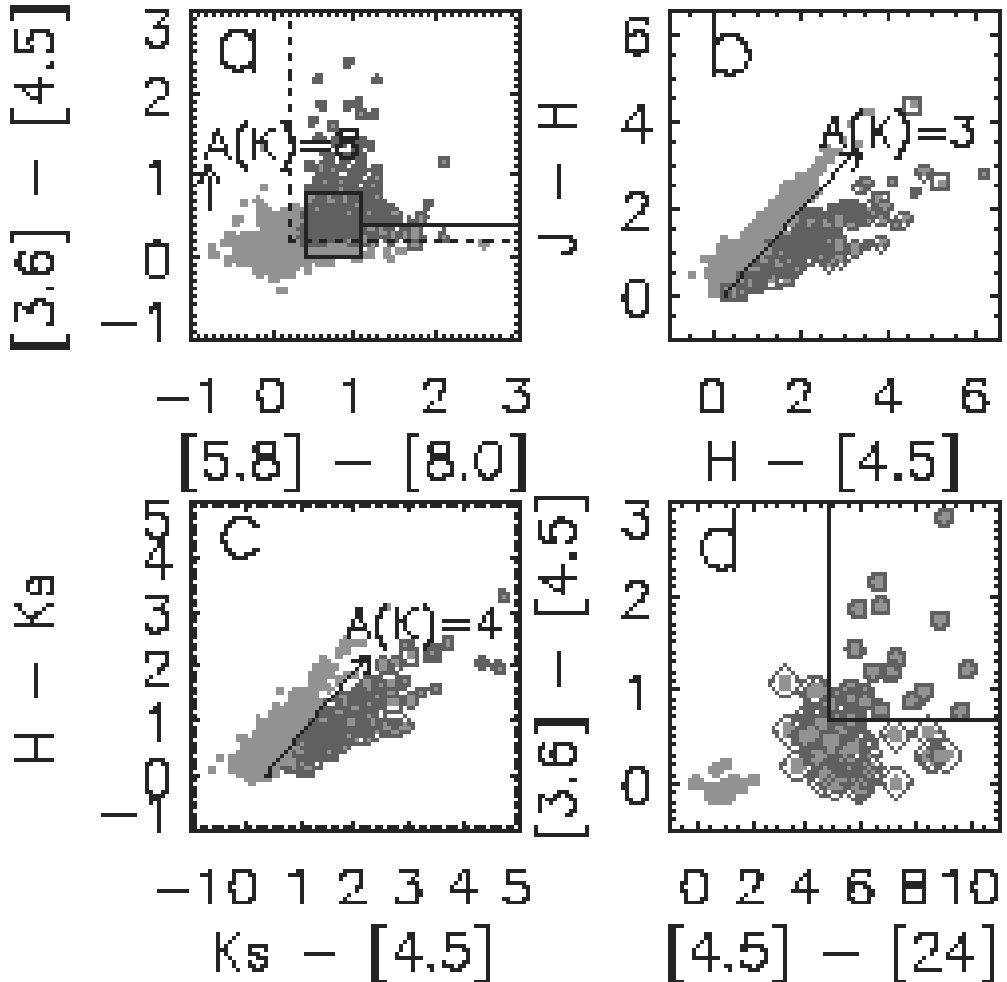


Fig. 1.— Color-color diagrams used to identify and classify YSOs. Protostars, class I/II, and class II objects are encircled with circles, triangles, and diamonds, respectively. YSOs that can only be identified in the IRAC-2MASS diagrams are encircled with squares. Arrows in the first three diagrams are reddening vectors derived from an averaged reddening law in nearby star forming regions (Flaherty et al. 2007). (a) The IRAC diagram. The rectangle marks the class II region determined by Allen et al. (2004) and Megeath et al. (2004). The vertical and horizontal dotted lines represent the requirements of  $[5.8] - [8.0] > 0.2$  and  $[3.6] - [4.5] > 0.2$ , respectively. The horizontal solid line to the right of the class II rectangle labels the criterion of  $[3.6] - [4.5] = 0.4$  and  $[5.8] - [8.0] > 1.1$ , which is used to distinguish between protostars and class I/II objects (Megeath et al. 2004). (b) and (c) IRAC-2MASS diagrams. Sources more than  $1\sigma$  to the right of the reddening vectors are identified as having intrinsic infrared excesses. (d) The IRAC-MIPS diagram. The outlined region in the upper right corner represents the protostar region. An isolated group of sources in the lower left of the diagram are recognized as class III/field stars. Objects located outside of the protostar region and not in the class III/field stars group are classified as class II.

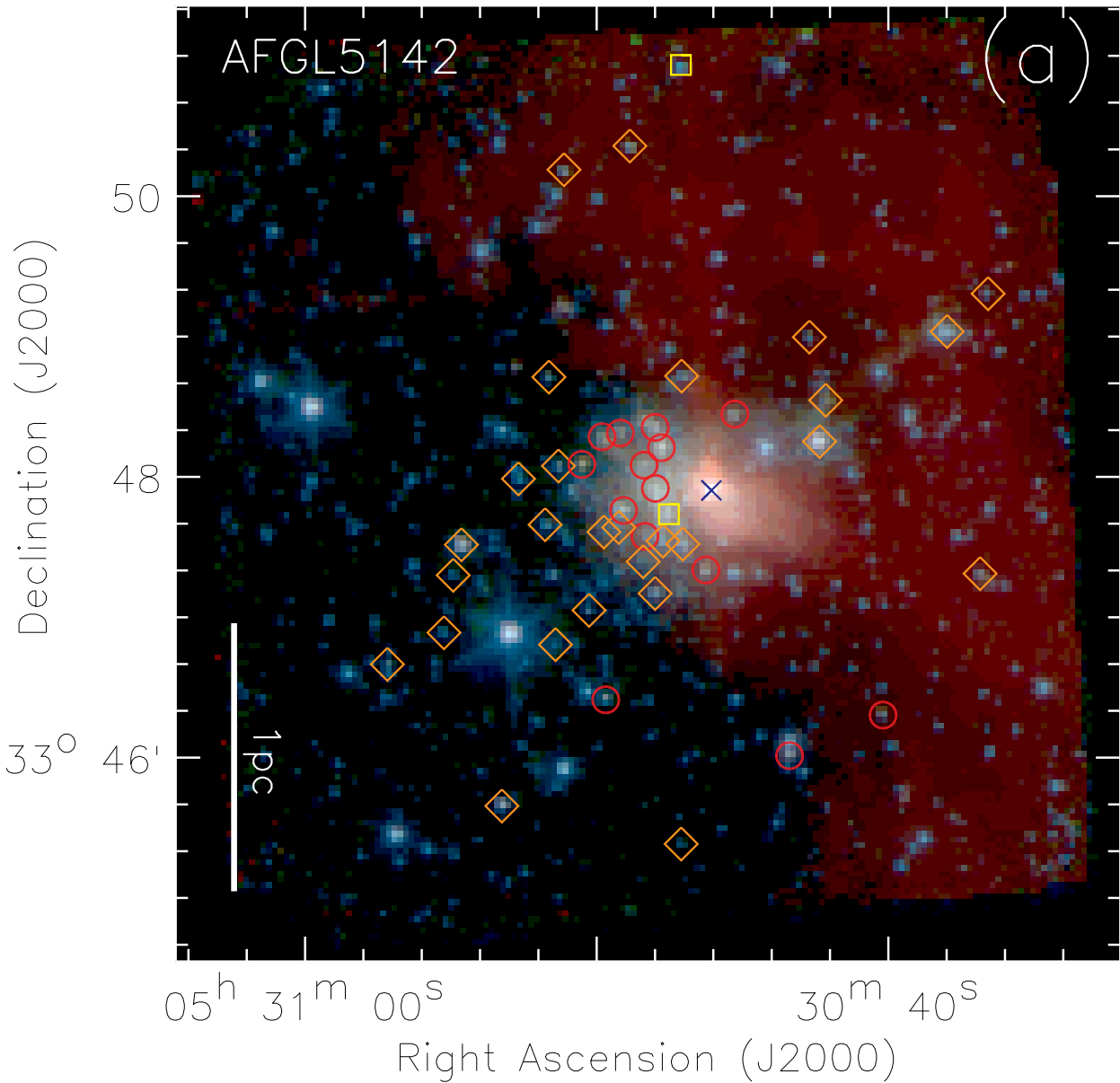


Fig. 2.— IRAC 3.6/4.5/8.0  $\mu\text{m}$  (Blue/Green/Red) three-color composite images of all 9 regions. Red circles, red triangles, and brown diamonds represent protostars, class I/II, and class II objects, respectively. Yellow squares mark YSOs that can only be identified in the IRAC-2MASS diagrams. Blue crosses label candidates of intermediate- to high-mass young stars (see “high” sources in Table 3 for details).

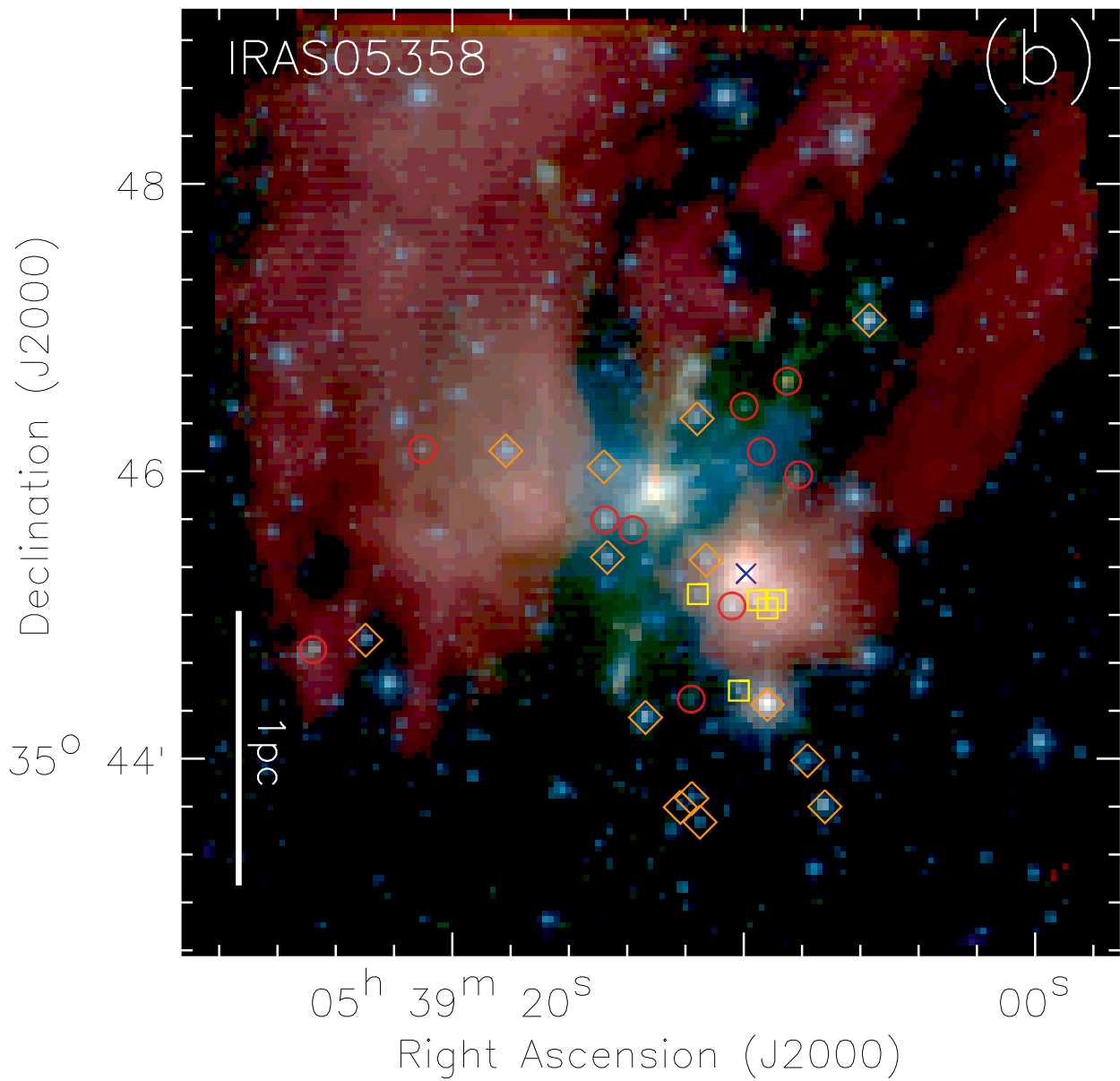


Fig. 2. — Continued

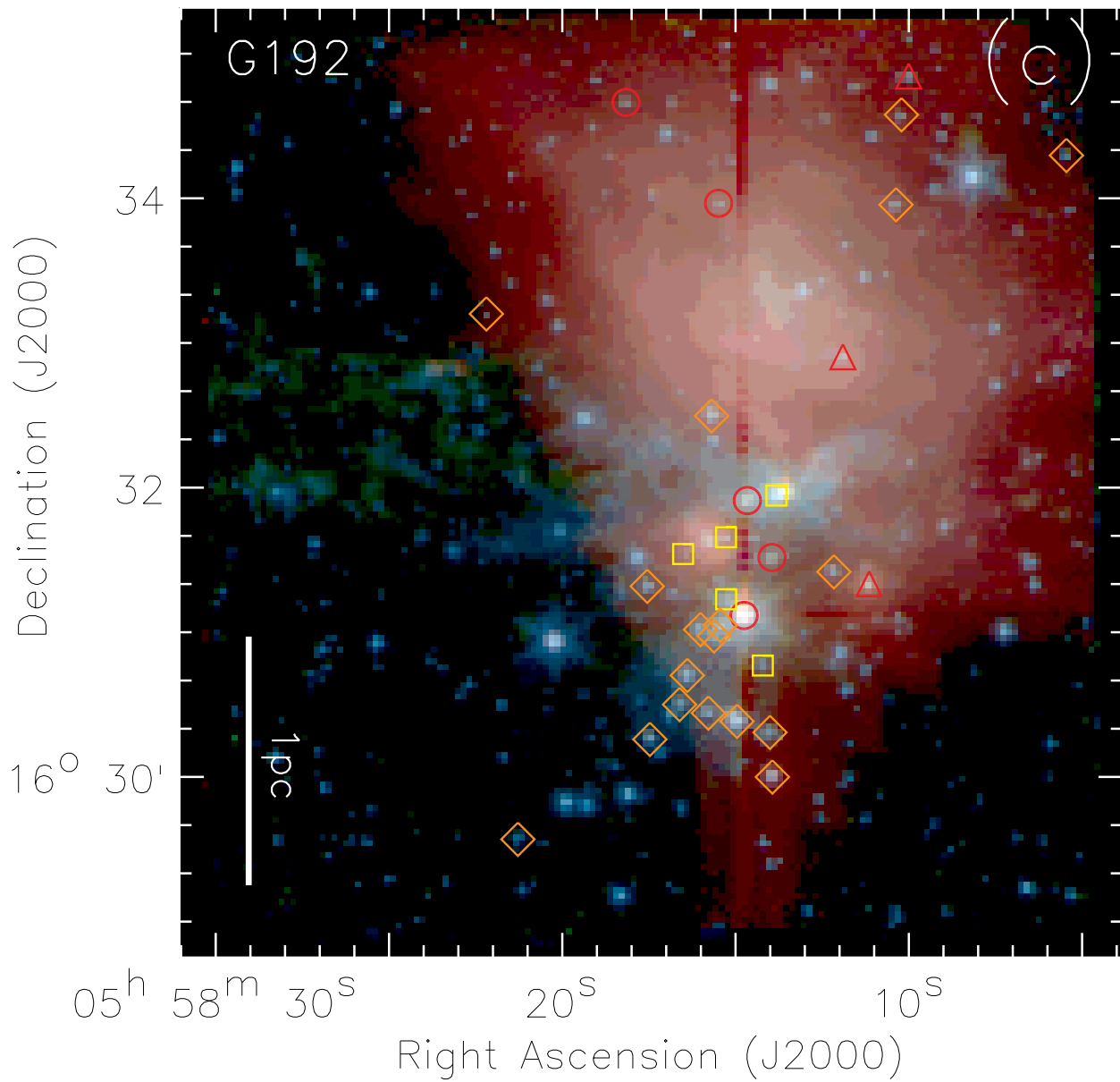


Fig. 2. — Continued

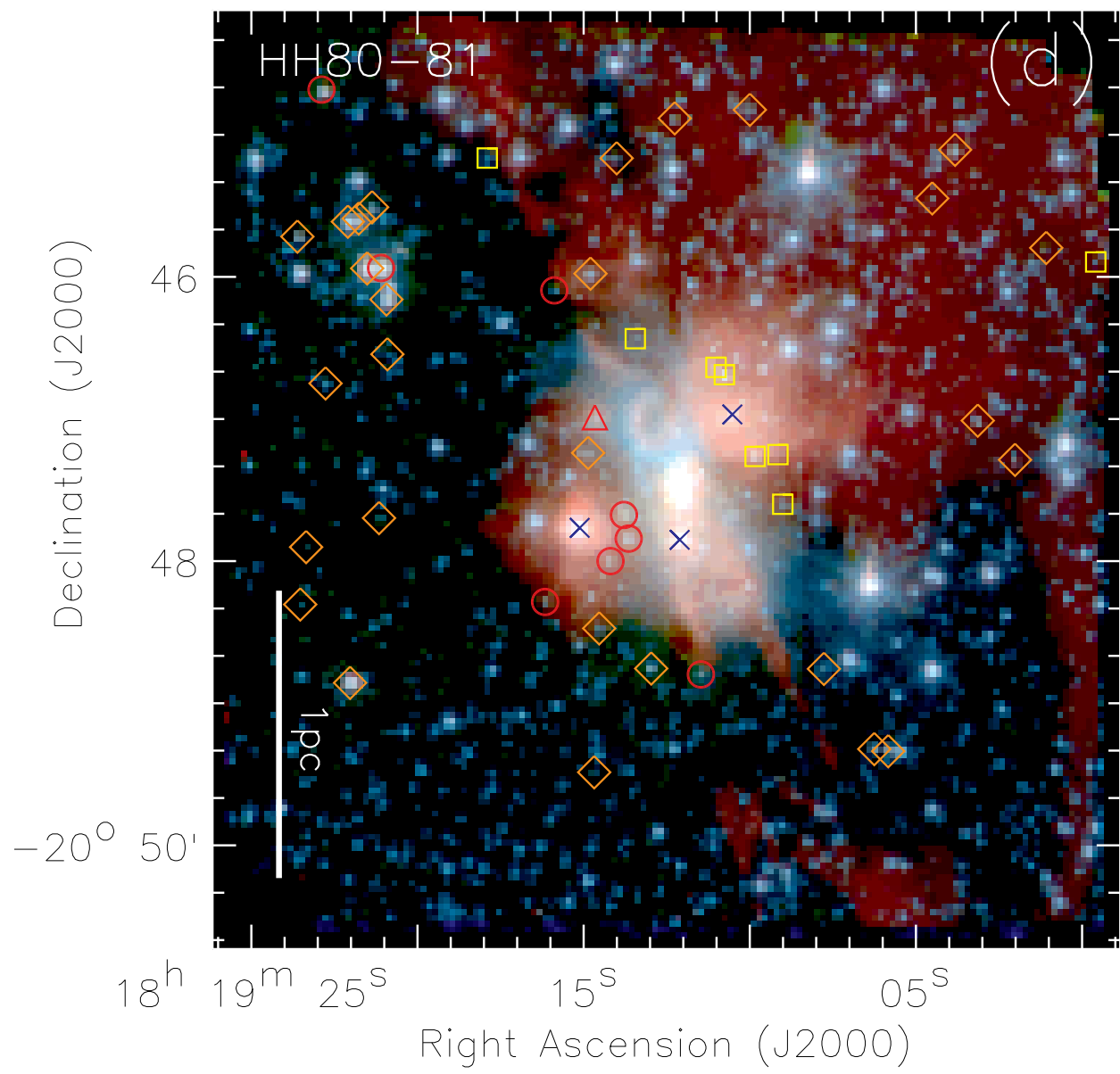


Fig. 2. — Continued

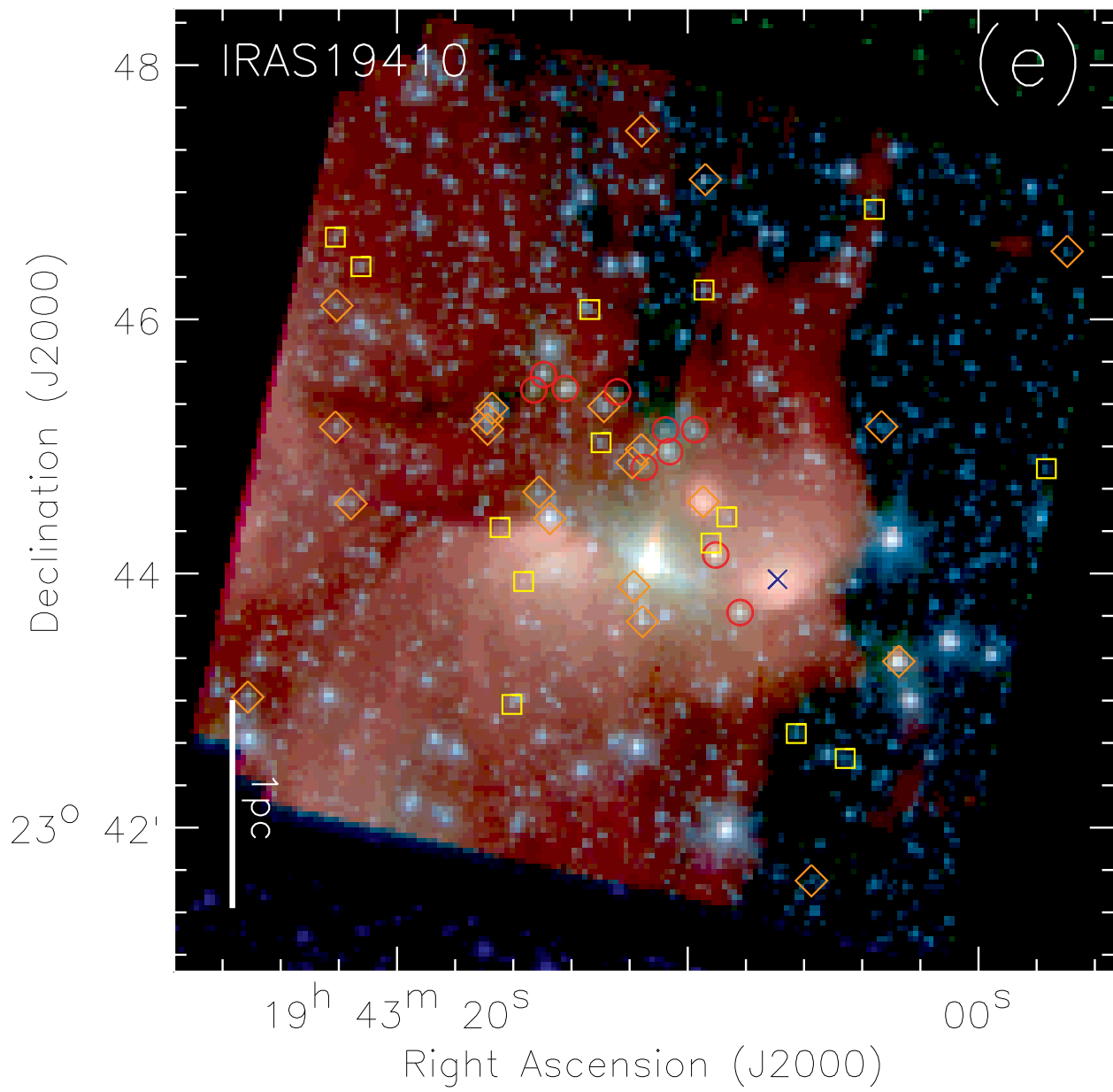


Fig. 2. — Continued

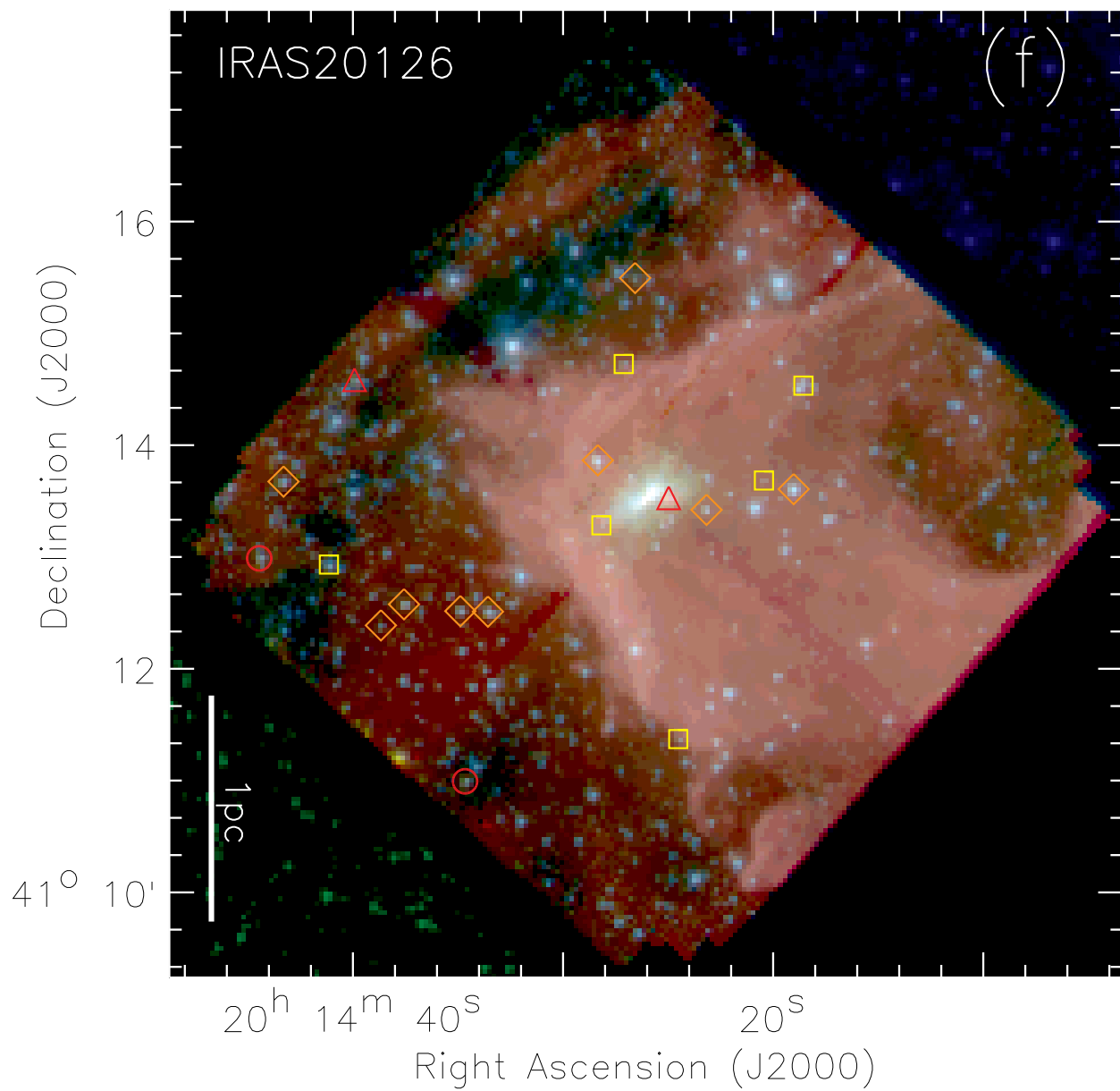


Fig. 2. — Continued

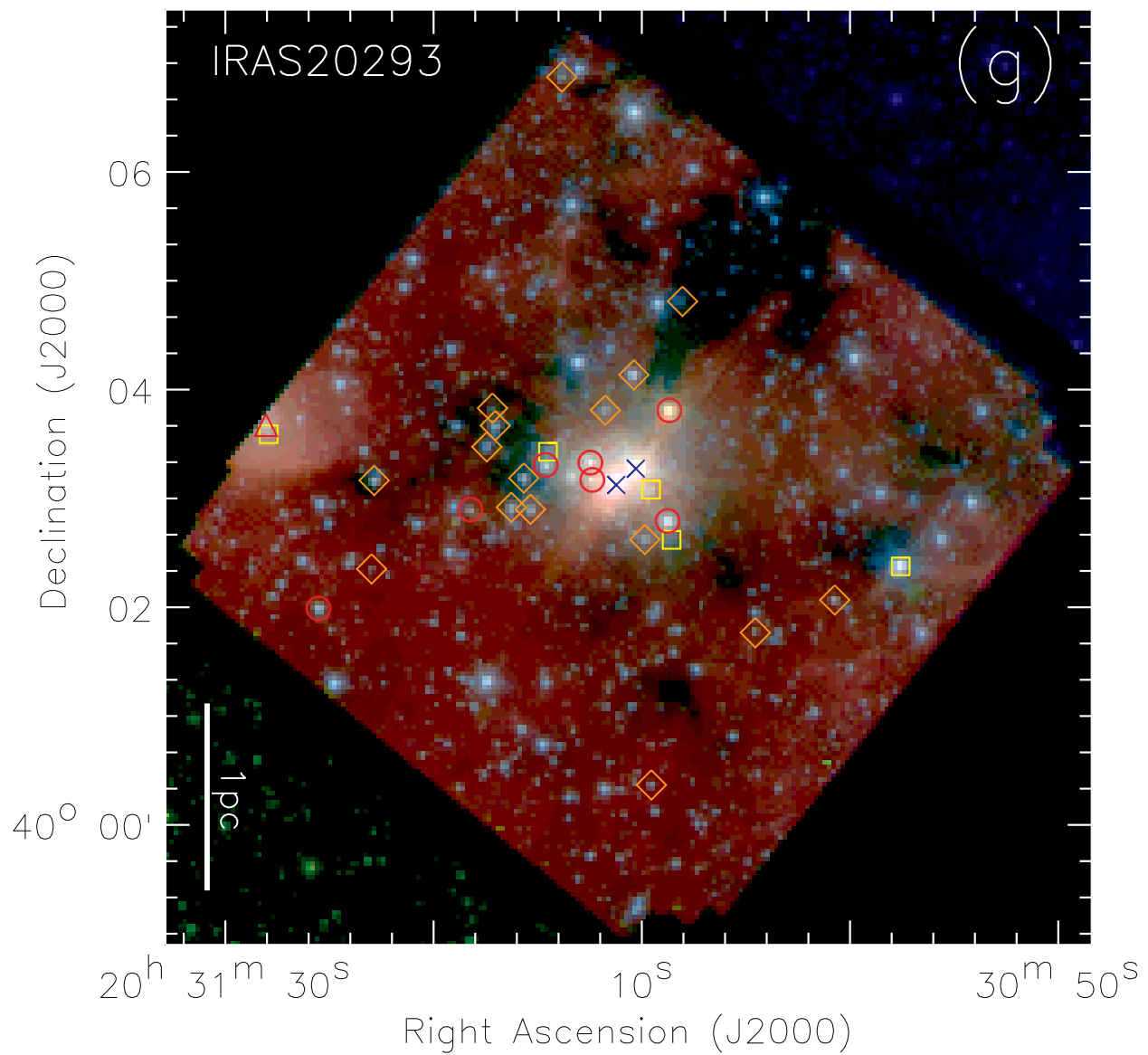


Fig. 2. — Continued

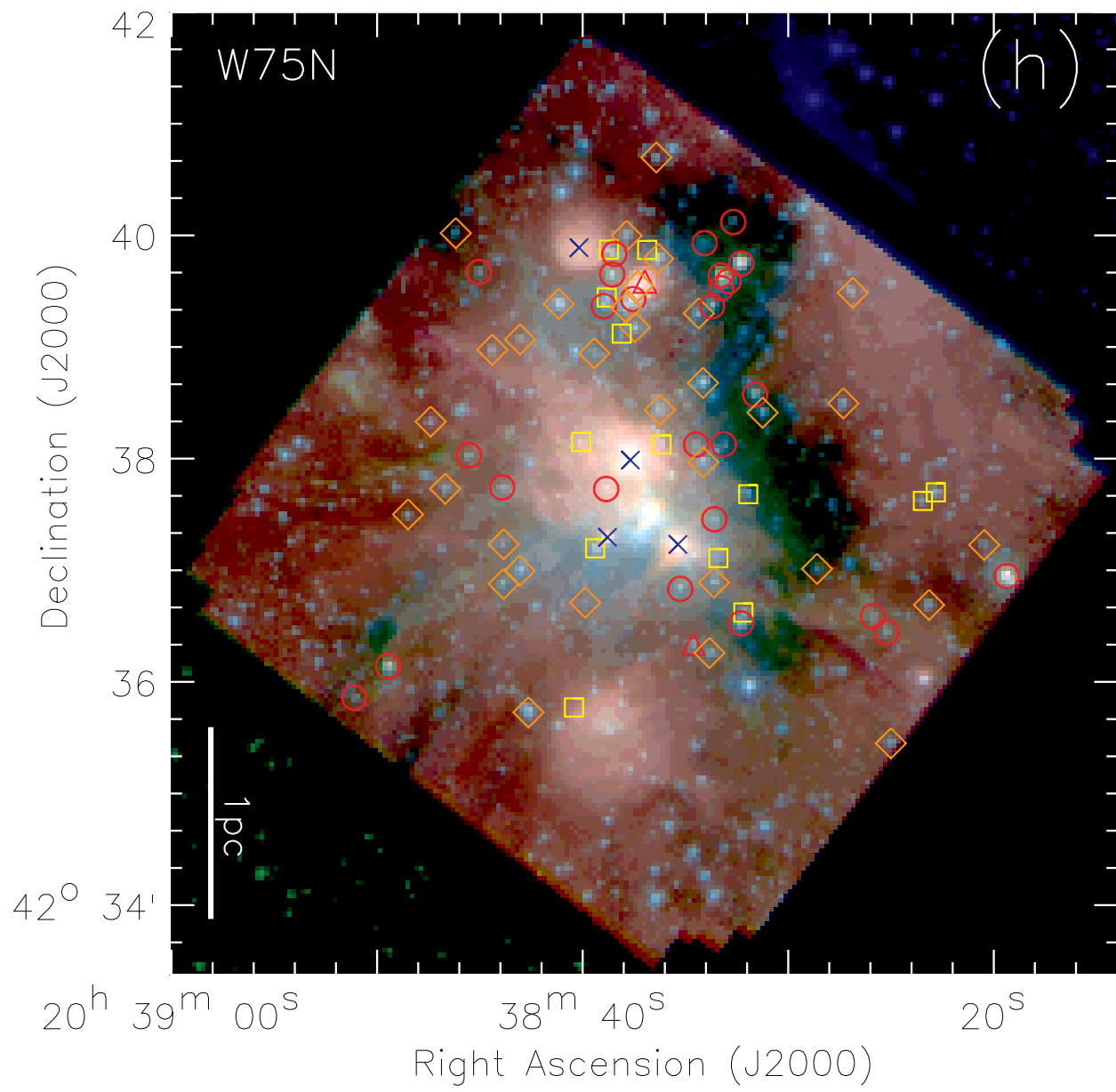


Fig. 2. — Continued

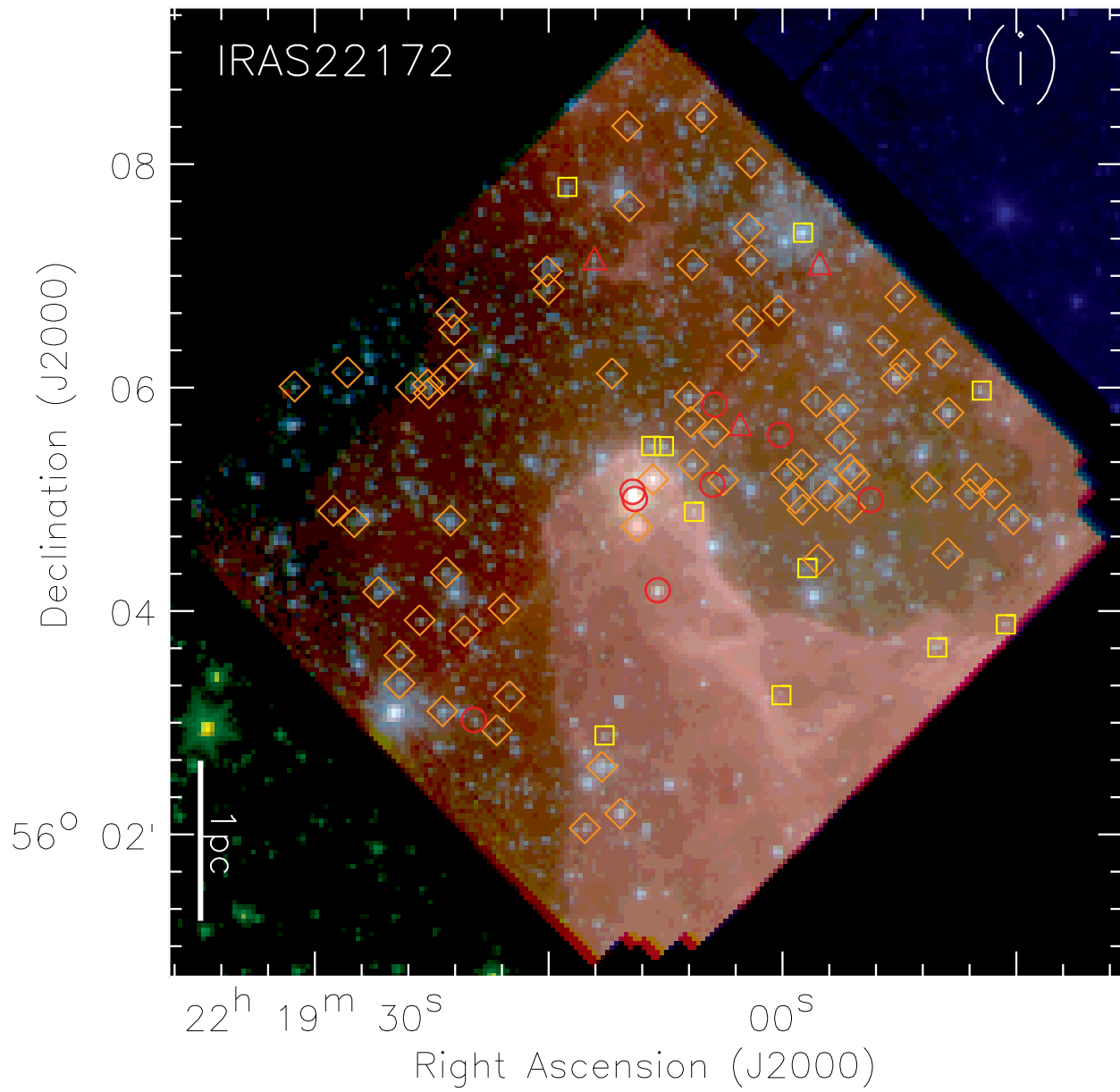


Fig. 2. — Continued

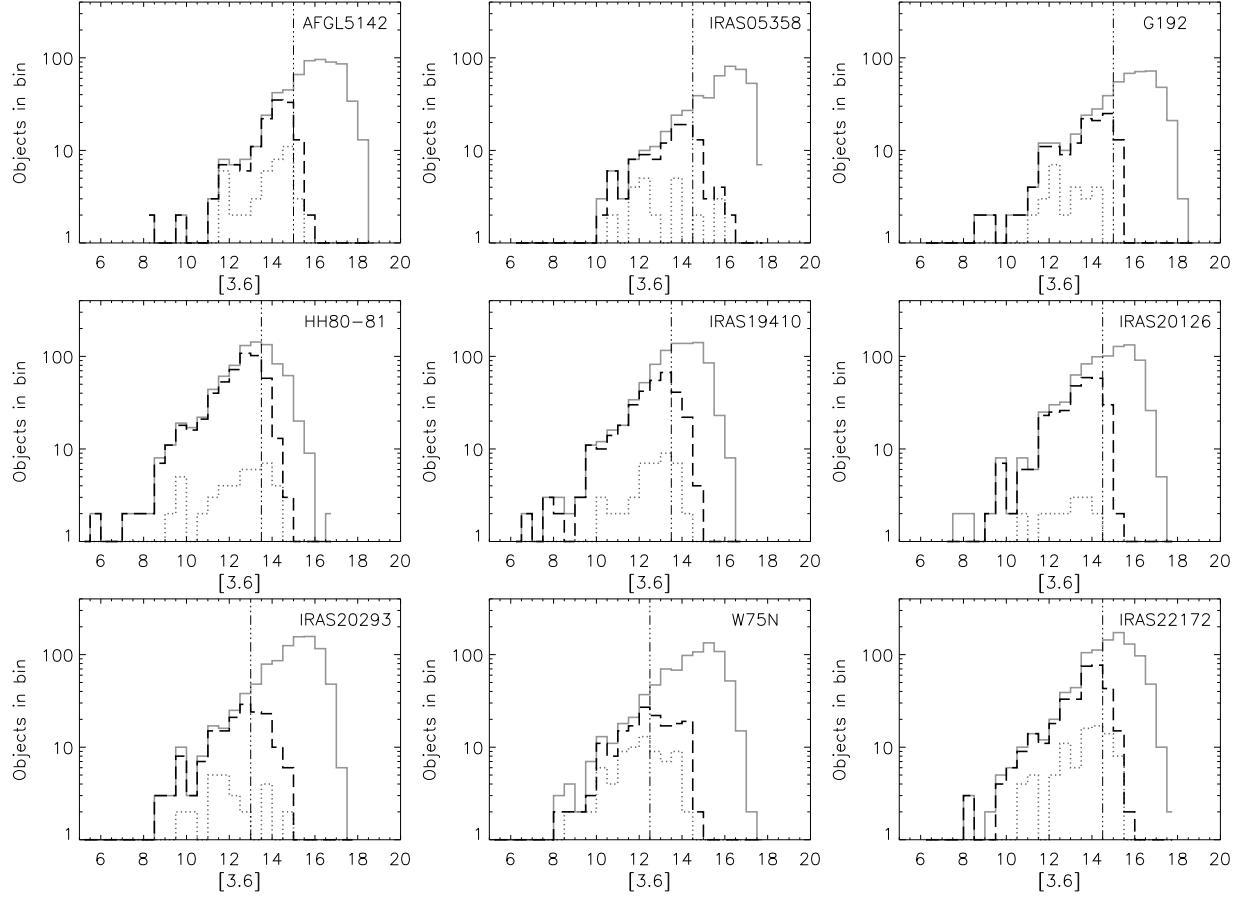


Fig. 3.— Histograms of sources in the 0.5 mag bins as a function of the  $3.6 \mu\text{m}$  magnitudes. The gray solid lines plot all the  $3.6 \mu\text{m}$  detections in each field. The dark dashed lines show sources with multi-band photometry, which can be placed on one or more color-color diagrams for search of infrared excess. The gray dotted lines represent sources that are identified as YSOs.

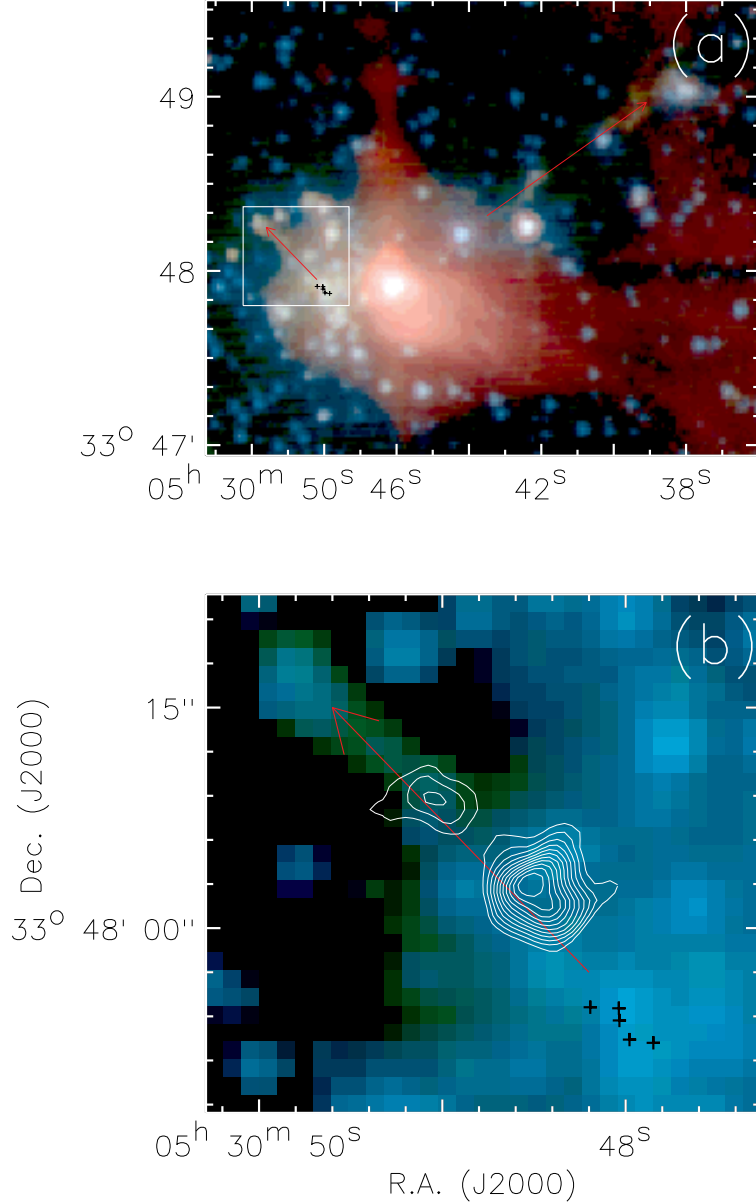


Fig. 4.— AFGL 5142: (a) The  $3.6/4.5/8.0 \mu\text{m}$  (B/G/R) three-color composite of the central part. The short and long arrows mark the orientations of two detected jets. (b) The  $3.6/4.5 \mu\text{m}$  (B/G) two-color composite of the area labelled by a rectangle in (a), to more clearly show the short jet prominent in the  $4.5 \mu\text{m}$  band. Contours are high-velocity CO emission from outflow B in Zhang et al. (2007). Plus signs in both panels mark the millimeter continuum peaks (MM1 to MM5) from Zhang et al. (2007).

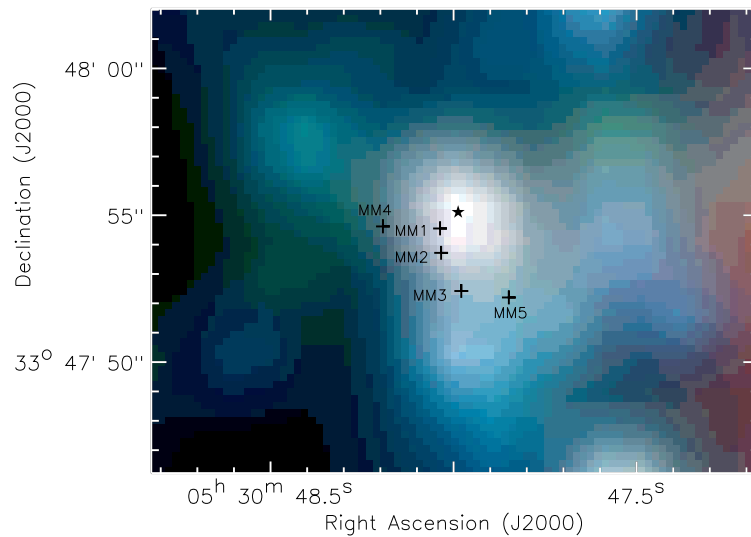


Fig. 5.— AFGL 5142: the 3.6/4.5/8.0  $\mu\text{m}$  (B/G/R) three-color composite of the inner massive star formation site, to show a comparison between the point-source detections in the IRAC bands and previous millimeter continuum observation. The star symbol denotes a protostar identified from the color-color diagrams. Plus signs mark the millimeter continuum peaks (MM1 to MM5) from Zhang et al. (2007).

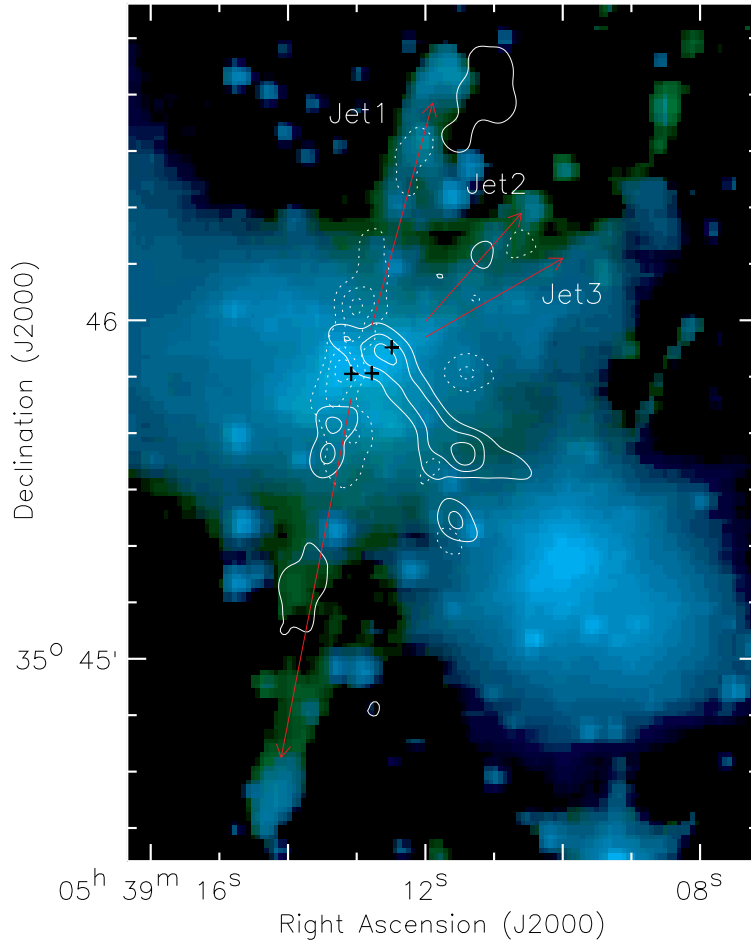


Fig. 6.— IRAS 05358: the  $3.6/4.5 \mu\text{m}$  two-color composite of the central part. The arrows mark the orientations of three detected jets, which are labelled as “Jet1”, “Jet2”, and “Jet3” from east to west. Solid and dashed contours show blue- and redshifted lobes of CO outflows from Beuther et al. (2002), respectively. Plus signs mark the  $3.1 \text{ mm}$  continuum peaks from Beuther et al. (2007).

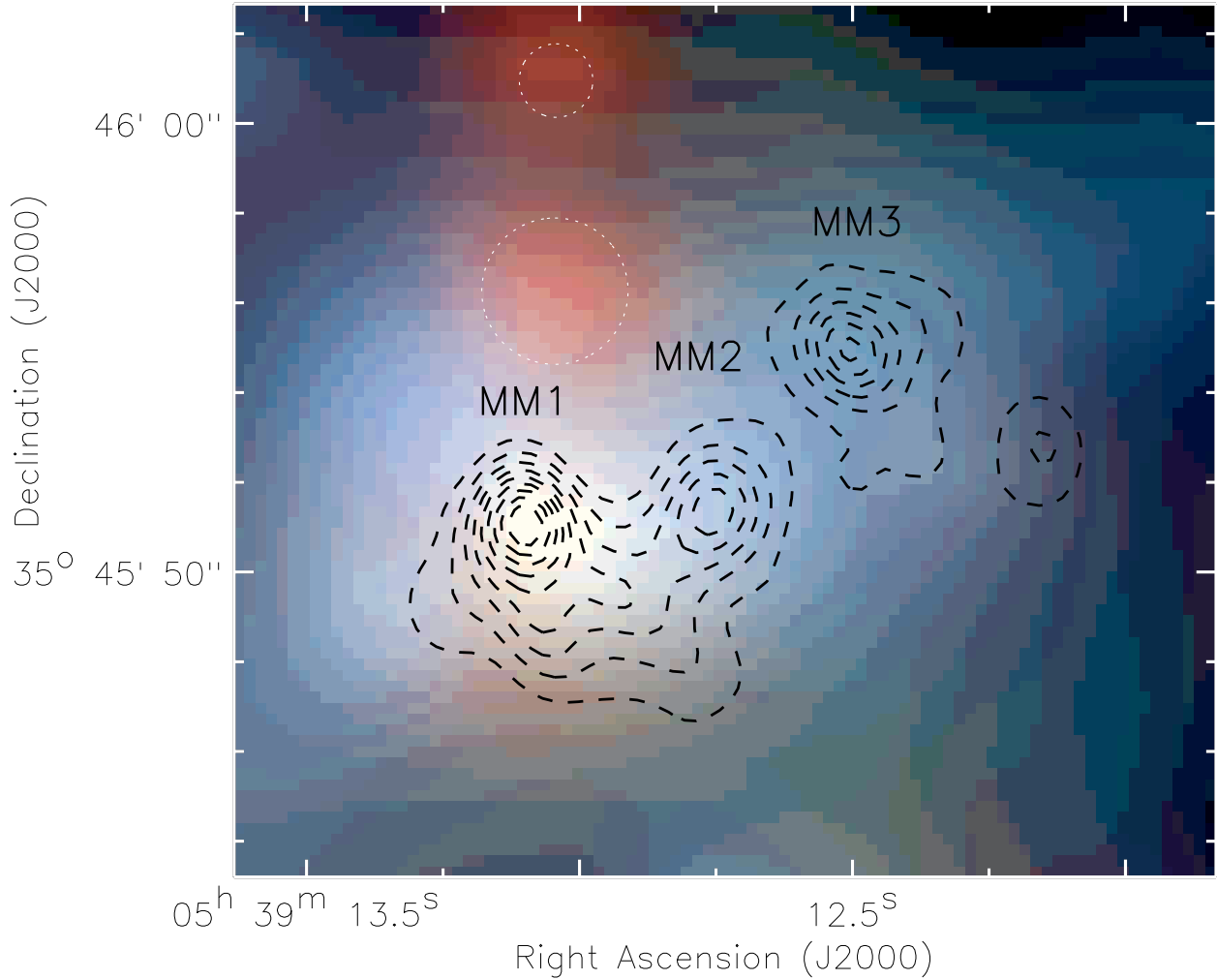


Fig. 7.— IRAS 05358: the 3.6/4.5/8.0  $\mu$ m three-color composite of the inner massive star formation site, to show a comparison between the point-source detections in the IRAC bands and previous millimeter continuum observation. The dashed contours are for the 3.1 mm continuum emission with three peaks labelled as “MM1”, “MM2”, “MM3” (Beuther et al. 2007). The two white dashed circles denote “bandwidth” artifacts in the 8.0  $\mu$ m band.

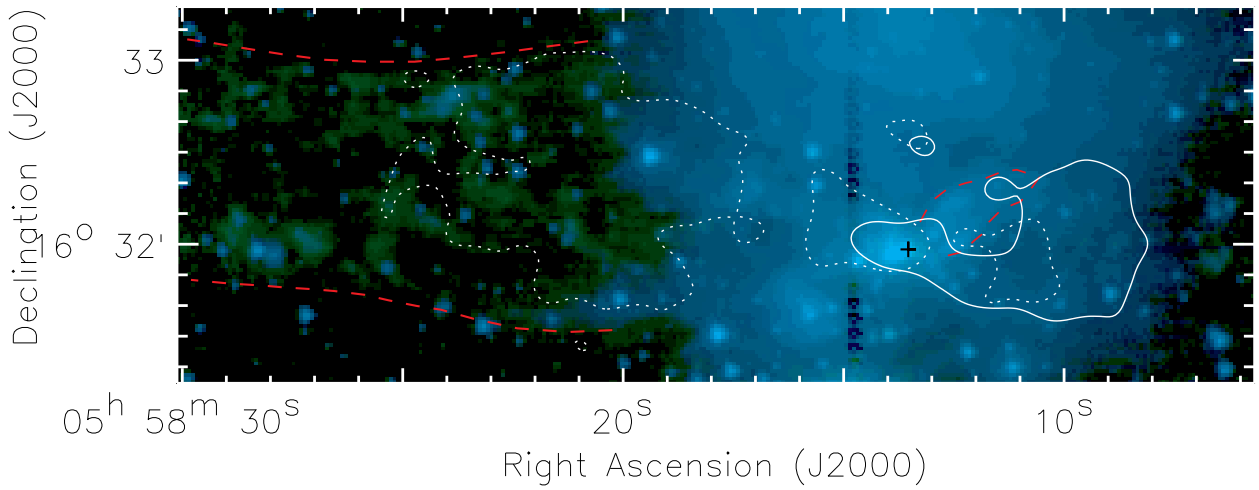


Fig. 8.— G192: the  $3.6/4.5 \mu\text{m}$  two-color composite of the central part. Solid and dashed contours are the lowest contours of red- and blueshifted CO outflow, respectively (Shepherd et al. 1998). Two red dashed lines in the east outline the area filled with “green” nebulosities, and the red dashed curve in the west the candle-flame-shaped structure (this structure is more prominent in the three-color composite Figure 2c). The plus sign marks the millimeter continuum peak from Shepherd et al. (1998).

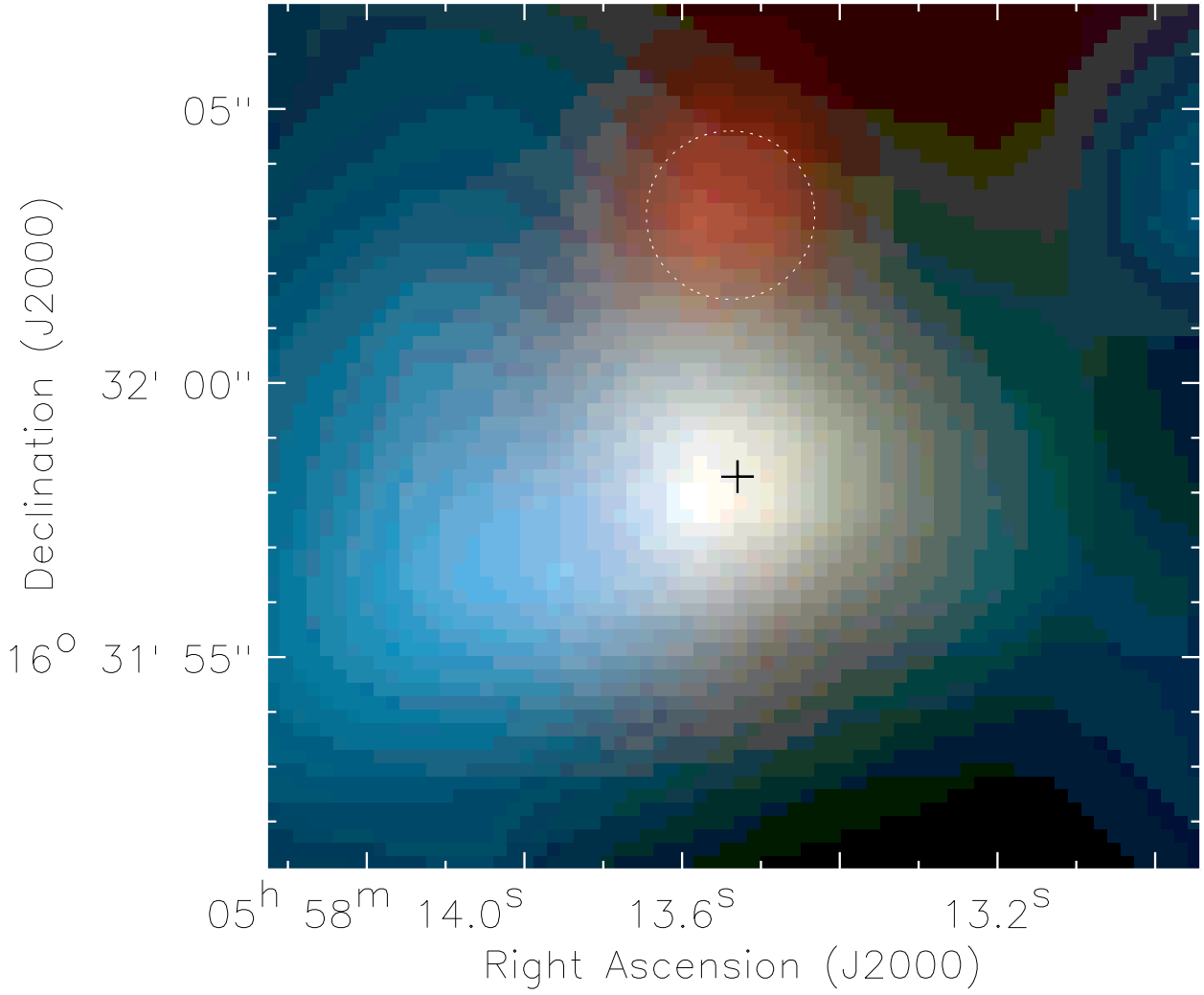


Fig. 9.— G192: the 3.6/4.5/8.0  $\mu\text{m}$  three-color composite of the inner massive star formation site, to show a comparison between the point-source detections in the IRAC bands and previous millimeter continuum observation. The plus sign marks the millimeter continuum peak from Shepherd et al. (1998).

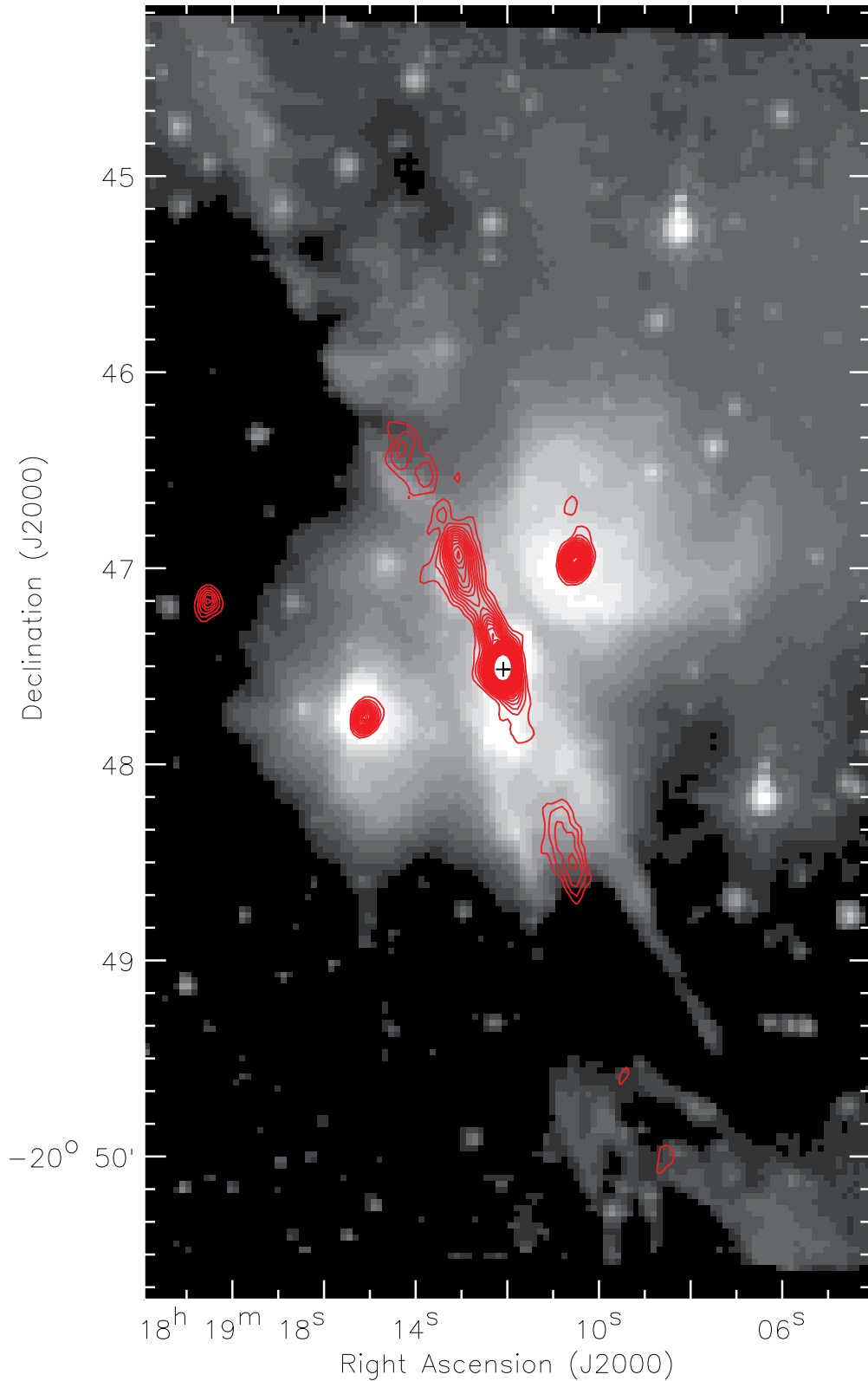


Fig. 10.— HH 80-81: the  $8.0 \mu\text{m}$  band emission in grayscale and the  $6 \text{ cm}$  continuum emission from Martí et al. (1993) in contours. The plus sign marks the  $7 \text{ mm}$  continuum peak from Gómez et al. (2003).

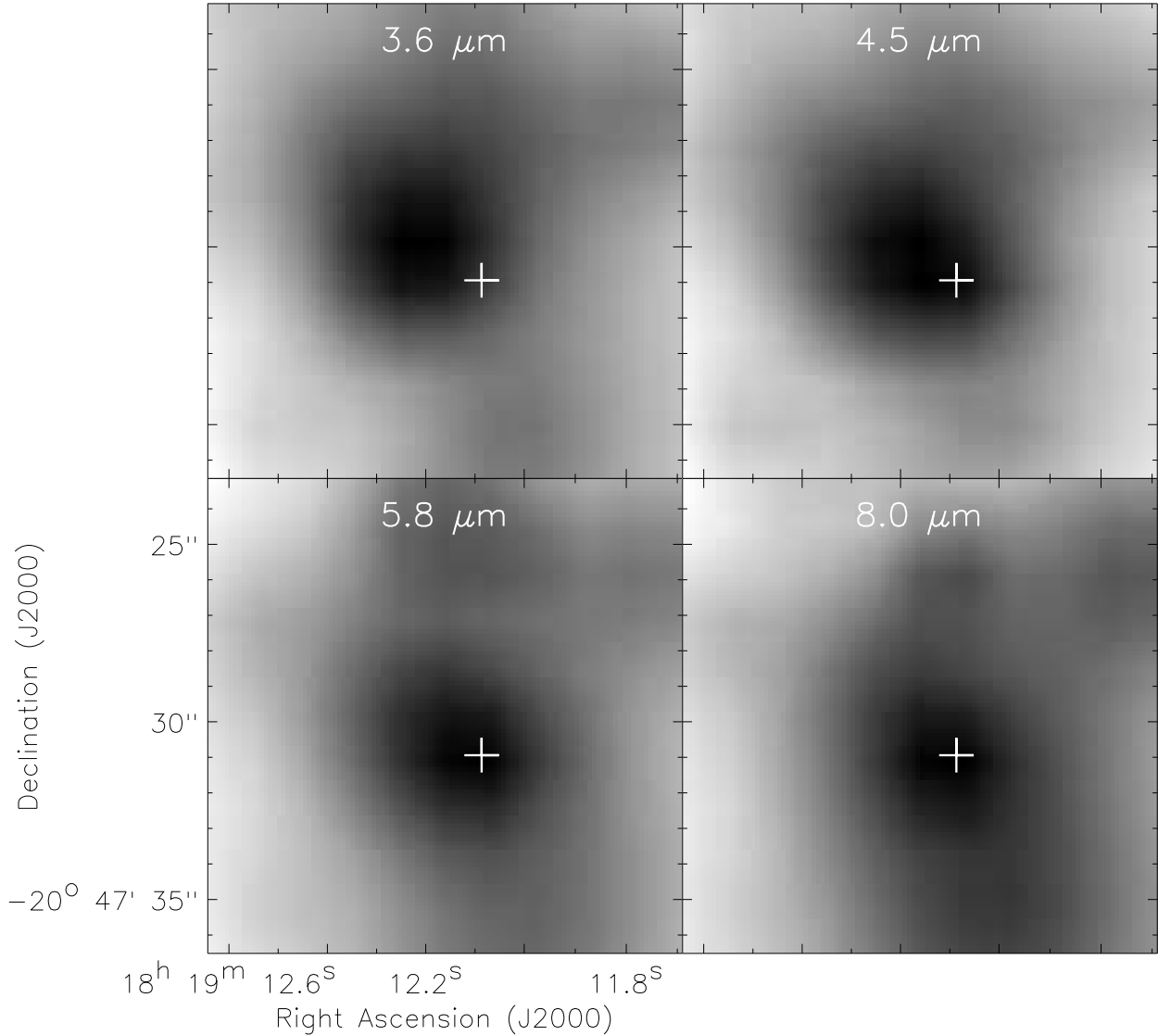


Fig. 11.— HH 80-81: the IRAC band emission from the inner massive star formation site, to show a comparison between the point-source detections in the IRAC bands and previous millimeter continuum observation. The plus sign marks the 7 mm continuum peak from Gómez et al. (2003).

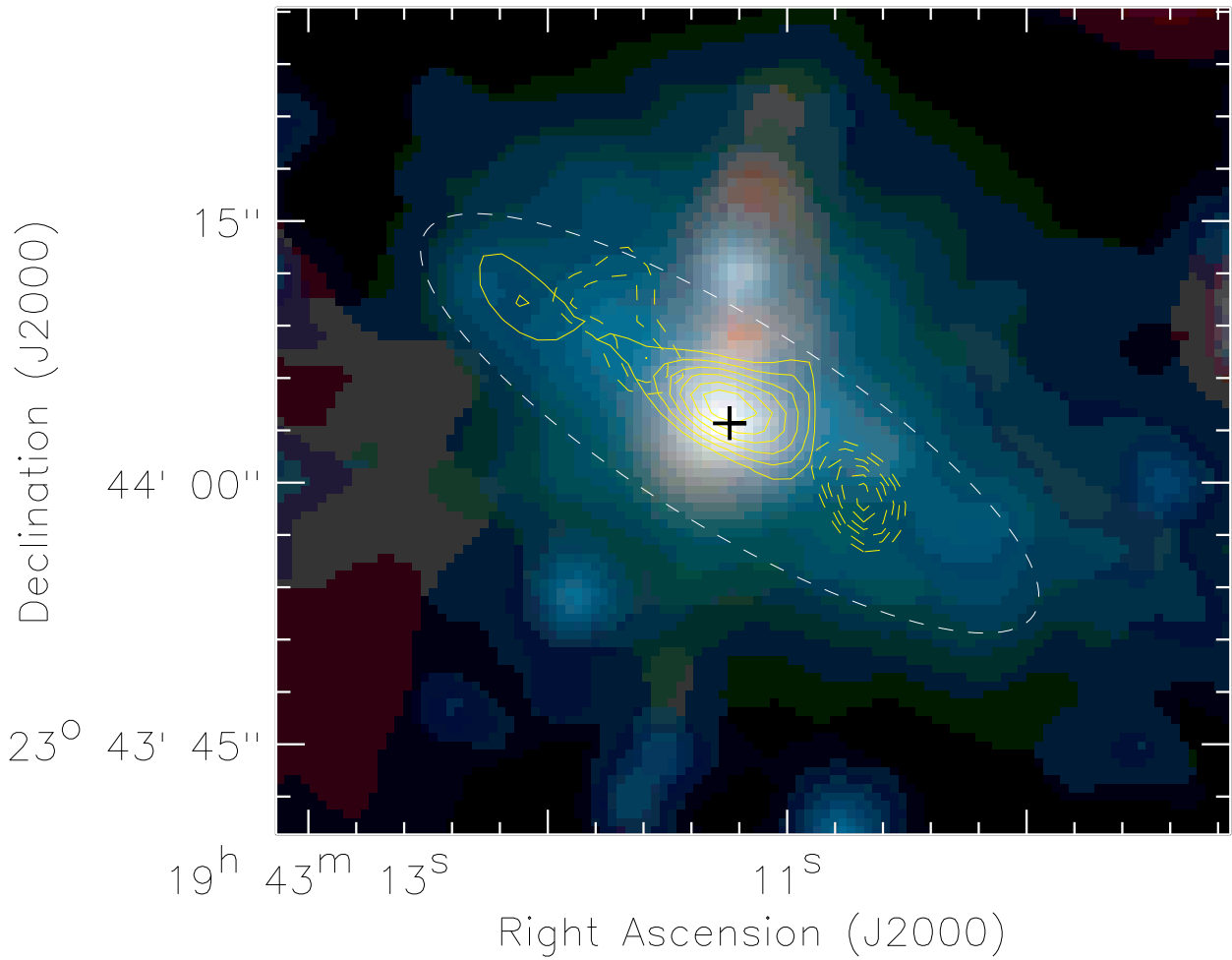


Fig. 12.— IRAS 19410: the 3.6/4.5/8.0  $\mu\text{m}$  three-color composite of the central part. The dashed ellipse outlines the IRAC elliptical structure. Solid and dashed contours show blue- and redshifted lobes from a CO outflow by Beuther et al. (2003), respectively, and the plus sign a millimeter continuum peak therein.

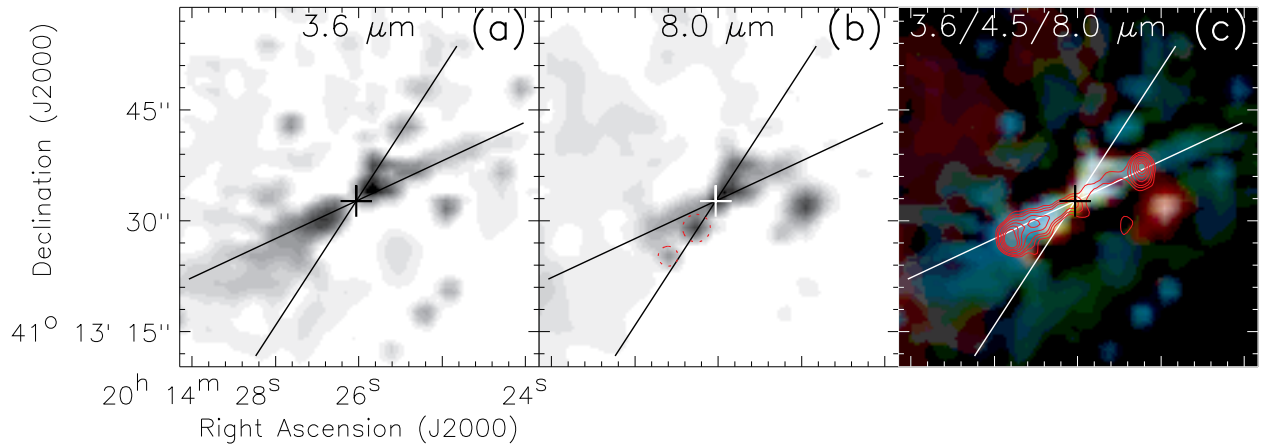


Fig. 13.— IRAS 20126: the IRAC bands emission from the central part. (a) The  $3.6 \mu\text{m}$  emission. To highlight the bipolar nebula a high-pass-filtering in IDL has been applied to the image. (b) Same as (a), but for the  $8.0 \mu\text{m}$  emission. Infrared emission from the central source is detected at this wavelength. The two dashed circles mark “bandwidth” artifacts induced by the central bright source. (c) The  $3.6/4.5/8.0 \mu\text{m}$  three-color composite, with an SiO (2-1) jet from Cesaroni et al. (1999) overlaid in red contours. In each panel the crossing lines outline the wall of the IRAC biconical structure. The plus sign marks the  $1.2 \mu\text{m}$  continuum peak from Cesaroni et al. (2005).

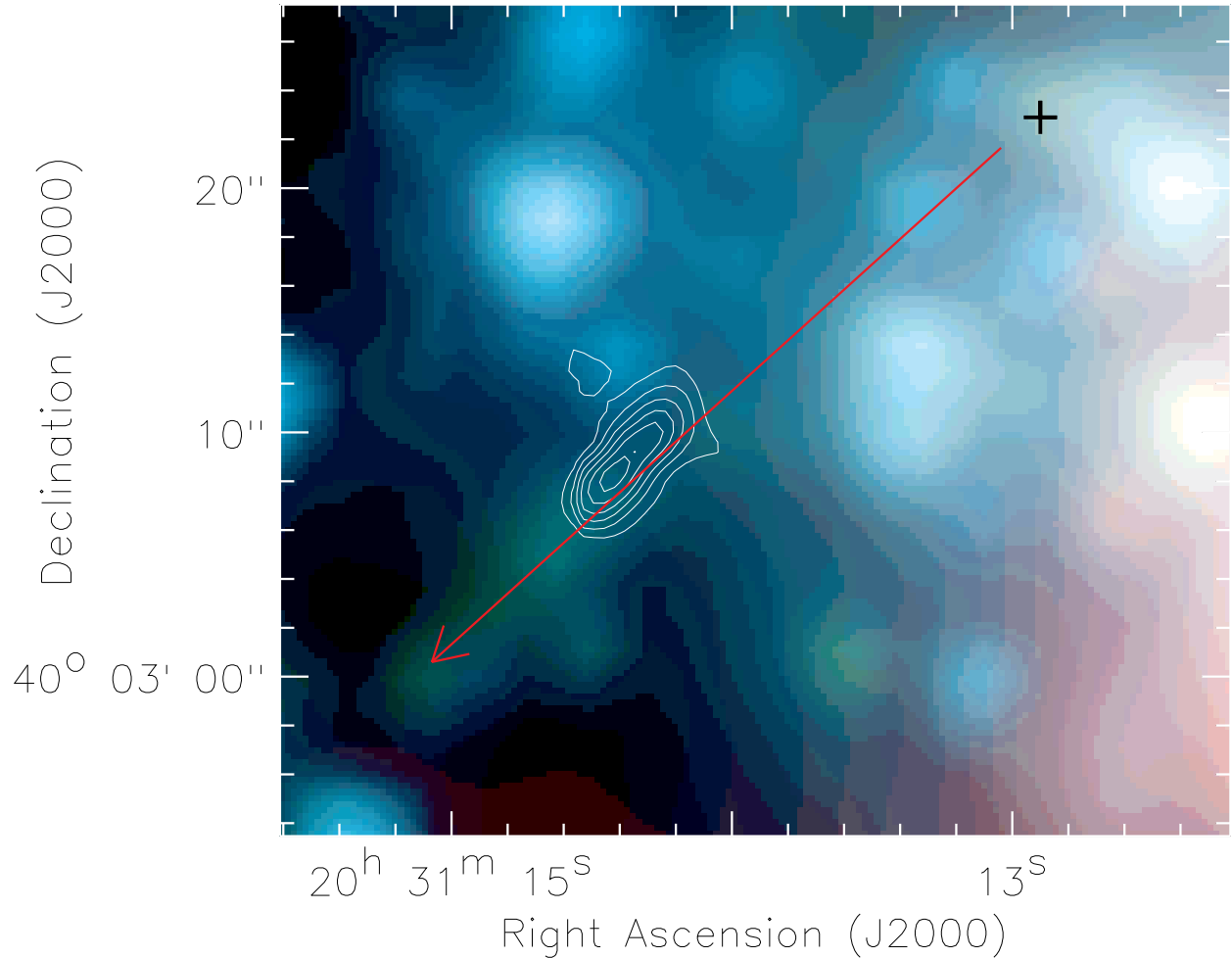


Fig. 14.— IRAS 20293: the 3.6/4.5/8.0  $\mu\text{m}$  three-color composite of the central part. The arrow marks the orientation of a jet prominent in the 4.5  $\mu\text{m}$  band. The contours show blueshifted high-velocity CO emission in a jet-like outflow and the plus sign the millimeter continuum peak from Beuther & Schilke (2004a).

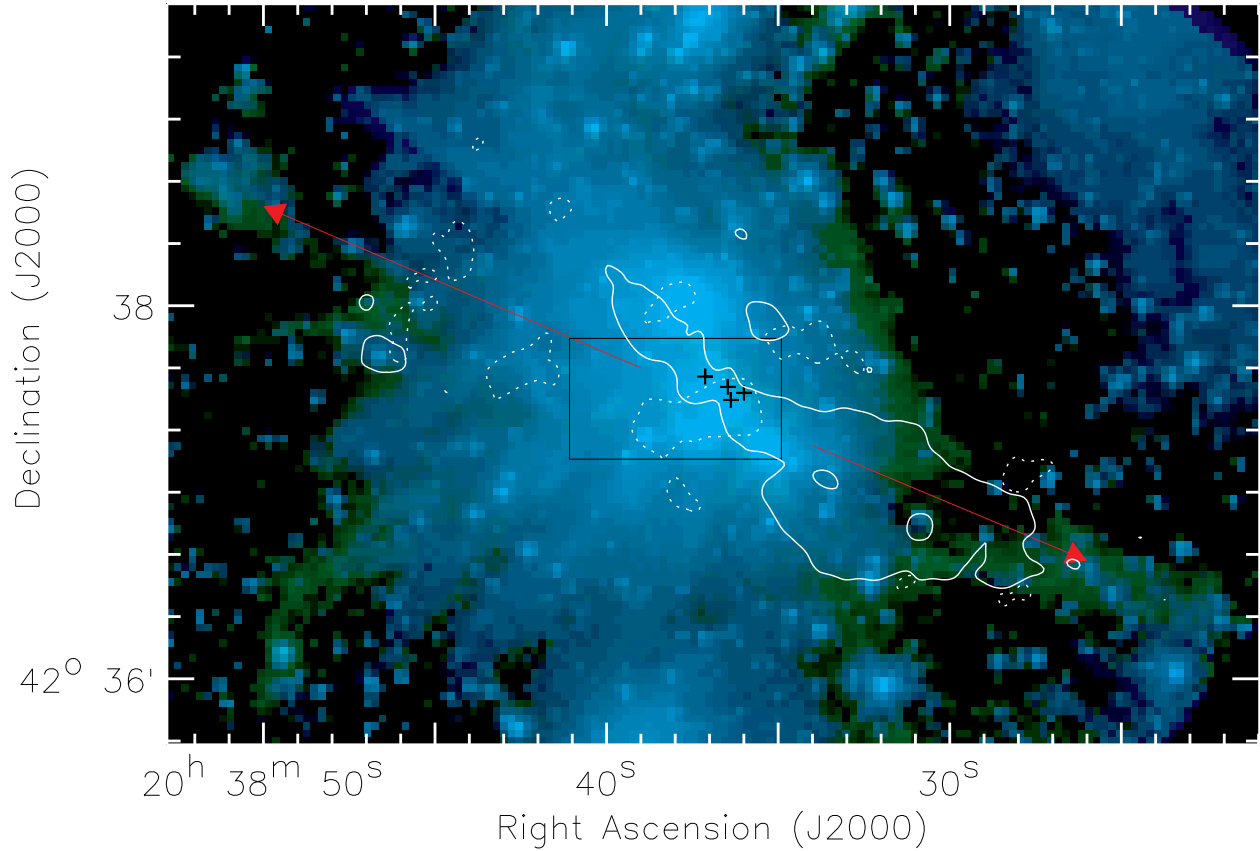


Fig. 15.— W75 N: the  $3.6/4.5 \mu\text{m}$  two-color composite of the central part. The double arrows mark the orientation of a large scale bow-shaped structure. Solid and dashed contours are the lowest contours of red- and blueshifted emission in a CO outflow, respectively (Shepherd et al. 2003). Plus signs mark the millimeter continuum peaks from Shepherd (2001).

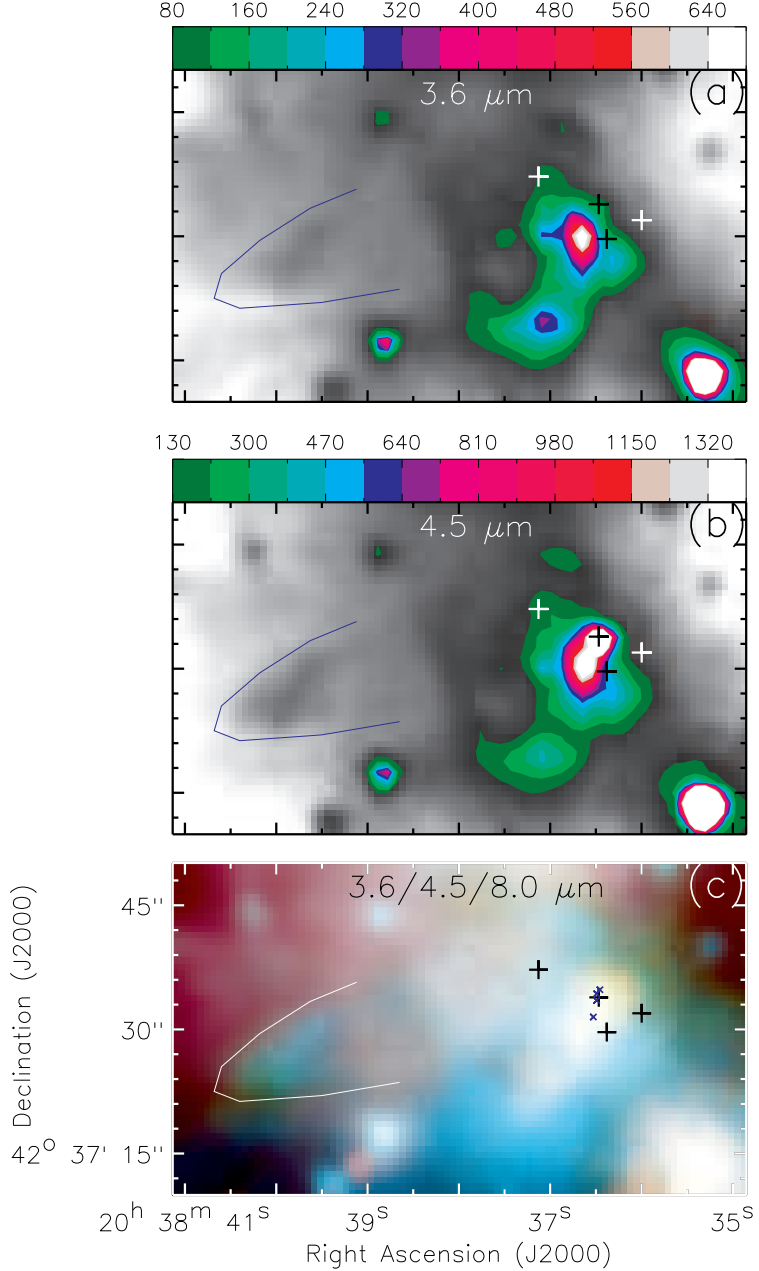


Fig. 16.— W75 N: the IRAC bands emission of the area labelled as a rectangle in Figure 15. (a) The  $3.6 \mu\text{m}$  emission, with emission levels between 8.2 and 80 MJy/sr shown in grayscale and that beyond 80 MJy/sr in colored contours. The contour levels in MJy/sr are labelled at the top of the image. (b) Same as (a), but for the  $4.5 \mu\text{m}$  emission. The emission between 10.7 and 130 MJy/sr is shown in grayscale and that beyond 130 MJy/sr in colored contours. (c) The  $3.6/4.5/8.0 \mu\text{m}$  three-color composite. In each panel a solid curve outlines the edge of a small bow-shaped structure and the plus signs mark the millimeter continuum peaks (MM1 to MM4) from Shepherd (2001). The crosses in (c) mark the centimeter continuum peaks revealed by Hunter et al. (1995) and Torrelles et al. (1997).

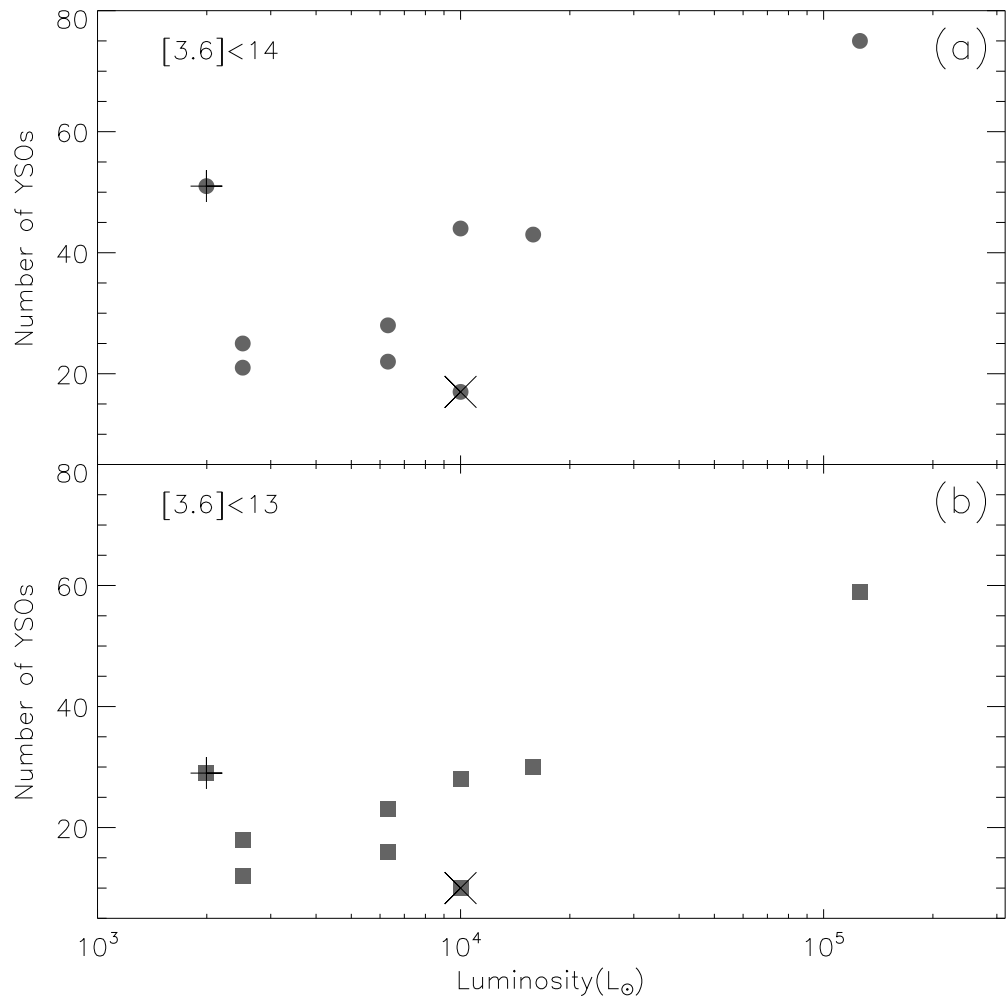


Fig. 17.— The number of detected YSOs vs. the IRAS luminosity. (a) The YSOs number counted from those with  $[3.6] < 14$ . The data points for IRAS 22172 and IRAS 20126 are overlaid with a plus sign and a cross, respectively. (b) Same as (a), but for YSOs with  $[3.6] < 13$ .